



Title	Effective Separation of Diluted Pollutants Using Monolithic Microhoneycombs
Author(s)	吉田, 誠一郎
Citation	北海道大学. 博士(工学) 甲第12801号
Issue Date	2017-03-23
DOI	10.14943/doctoral.k12801
Doc URL	<a href="http://hdl.handle.net/2115/74523">http://hdl.handle.net/2115/74523</a>
Type	theses (doctoral)
File Information	Seiichiro_Yoshida.pdf



[Instructions for use](#)

# **Effective Separation of Diluted Pollutants Using Monolithic Microhoneycombs**

**Graduate School of  
Chemical Sciences and Engineering  
Hokkaido University**

**Seiichiro Yoshida**

**March, 2017**



## Index

<b>Chapter 1. Introduction</b>	...	1
1.1 General Introduction	...	1
1.2 Typical Sorption	...	1
1.2.1 Classification of Sorption	...	1
1.2.2 Adsorption	...	1
1.2.3 Ion Exchange	...	2
1.2.4 Absorption	...	2
1.3 Sorption Process in Industrial Fields	...	3
1.3.1 Classification of Sorption Process	...	3
1.3.2 Slurry	...	3
1.3.3 Fixed Bed	...	5
1.3.4 Fluidized Bed	...	7
1.4 Morphologies of Sorbents	...	8
1.4.1 Classification of Sorbent Morphology	...	8
1.4.2 Particles	...	8
1.4.3 Fibers	...	9
1.4.4 Monoliths	...	9
1.5 Microhoneycombs	...	10
1.5.1 Ice-Templating Method	...	10
1.5.2 Features of Microhoneycombs	...	12
1.5.3 Application of Microhoneycombs	...	13
1.6 Objectives and Contents	...	14
1.7 Reference	...	16
<b>Part 1 Separation of Organic Compounds in Flow Systems Using Carbon Cryogel with a Microhoneycomb Structure</b>	...	21
<b>Chapter 2 Phenol and Methylene Blue Adsorption in Flow Systems Using Carbon Cryogels with a Microhoneycomb Structure</b>	...	23
2.1 Introduction	...	23
2.2 Materials and Methods	...	25
2.2.1 Materials	...	25

2.2.2 Preparation of CMHs	...	25
2.2.3 Characterization of the CMHs	...	26
2.2.4 Adsorption of Phenol and MB on the CMHs	...	27
2.3 Results and Discussion	...	29
2.3.1 Characterization of the CMHs	...	29
2.3.2 Phenol and MB Adsorption Using CMHs in Batch Systems	...	32
2.3.3 Phenol and MB Adsorption Using CMHs in Flow Systems	...	35
2.4 Conclusion	...	40
2.5 Reference	...	41

**Part 2 Separation of Cesium Ion in Flow Systems Using Monolithic Ion-Exchangers with a Microhoneycomb Structure** ... 43

**Chapter 3 Separation of Cesium Ion in Flow Systems Using Persian Blue Analogues Nanoparticles Supported in a Silica-Alumina Microhoneycomb** ... 45

3.1 Introduction	...	45
3.2 Materials and Methods	...	45
3.2.1 Materials	...	46
3.2.2 Preparation of the PBAs-SAMH	...	46
3.2.3 Characterization of the PBAs-SAMHs	...	47
3.2.4 Cs <sup>+</sup> Separation Experiments Using the PBAs-SAMHs in Batch Systems	...	47
3.2.5 Cs <sup>+</sup> Separation Experiments Using the PBAs-SAMHs in Flow Systems	...	48
3.3 Results and Discussion	...	48
3.3.1 Characterization of the PBAs-SAMHs	...	48
3.3.2 Cs <sup>+</sup> Separation Experiments Using the PBAs-SAMHs in Batch Systems	...	53
3.3.3 Cs <sup>+</sup> Separation Experiments Using the PBAs-SAMHs in Flow Systems	...	54
3.4 Conclusion	...	56
3.5 Reference	...	56

**Chapter 4 Separation of Cesium Ion in Flow Systems Using Ammonium Molybdophosphate Supported in a Silica Microhoneycomb** ... 59

4.1 Introduction	...	59
4.2 Materials and Methods	...	60

4.2.1 Materials	...	60
4.2.2 Preparation of the AMP-SMHs	...	60
4.2.3 Characterization of the AMP-SMHs	...	61
4.2.4 Cs <sup>+</sup> Separation Experiments Using the AMP-SMHs in Batch Systems	...	63
4.2.5 Cs <sup>+</sup> Separation Experiments Using the AMP-SMHs in Flow Systems	...	63
4.3 Results and Discussion	...	69
4.3.1 Characterization of Synthesized AMP-SMHs	...	69
4.3.2 Cs <sup>+</sup> Separation Experiments Using the AMP-SMHs in Batch Systems	...	73
4.3.3 Cs <sup>+</sup> Separation Experiments Using the AMP-SMHs in Flow Systems	...	74
4.4 Conclusion	...	78
4.5 Reference	...	79
<b>Chapter 5 Separation of Cesium Ion in Flow Systems Using Resorcinol-Formaldehyde Cryogels with a Microhoneycomb Structure</b>	...	81
5.1 Introduction	...	81
5.2 Materials and Methods	...	82
5.2.1 Materials	...	82
5.2.2 Preparation of the RFMHs	...	82
5.2.3 Characterization of the RFMHs	...	82
5.2.4 Cs <sup>+</sup> Separation Experiments Using the RFMHs in Batch Systems	...	83
5.2.5 Cs <sup>+</sup> Separation Experiments Using the RFMHs in Flow Systems	...	83
5.3 Results and Discussion	...	84
5.3.1 Characterization of the RFMHs	...	84
5.3.2 Cs <sup>+</sup> Separation Experiments Using the RFMHs in Batch Systems	...	85
5.3.3 Cs <sup>+</sup> Separation Experiments Using the RFMHs in Flow Systems	...	89
5.4 Conclusion	...	89
5.5 Reference	...	90
<b>Part 3 Application of Microhoneycombs for Carbon Dioxide Absorption by Supported Ionic Liquid Phases</b>	...	93
<b>Chapter 6 Absorption of Carbon Dioxide in Flow Systems Using Silica Microhoneycombs Loaded with an Ionic Liquid</b>	...	95

<i>6.1 Introduction</i>	...	95
<i>6.2 Materials and Methods</i>	...	97
<i>6.2.1 Materials</i>	...	97
<i>6.2.2 Preparation of SMHs</i>	...	97
<i>6.2.3 Preparation of Ionic Liquid ([P<sub>66614</sub>][Ala])</i>	...	98
<i>6.2.4 Preparation of Silica Microhoneycombs Loaded with [P<sub>66614</sub>][Ala] (IL-SMHs)</i>	...	98
<i>6.2.5 Preparation of Silica Gel Particles Loaded with [P<sub>66614</sub>][Ala] (IL-SPs)</i>	...	98
<i>6.2.6 Characterization</i>	...	99
<i>6.2.7 Evaluation of the Hydraulic Resistance of IL-SMHs and a Column Packed with IL-SPs</i>	...	99
<i>6.2.8 CO<sub>2</sub> Separation Experiments in a Batch System</i>	...	100
<i>6.2.9 CO<sub>2</sub> Separation Experiments in a Flow System</i>	...	101
<i>6.3 Results and Discussion</i>	...	101
<i>6.3.1 Synthesis and Characterization of IL-SMHs and IL-SPs</i>	...	101
<i>6.3.2 Pressure Drop Measurements</i>	...	102
<i>6.3.3 CO<sub>2</sub> Sorption Isotherms on SMH and IL-SMH</i>	...	106
<i>6.3.4 CO<sub>2</sub> Separation Performance</i>	...	106
<i>6.4 Conclusion</i>	...	108
<i>6.5 Reference</i>	...	109
<b><i>Chapter 7 Conclusion</i></b>	...	111
<b><i>Acknowledgements</i></b>	...	115
<b><i>Research Achievements</i></b>	...	117

# ***Chapter 1***

## ***Introduction***

### **1.1 General Introduction**

Separation techniques, including adsorption, ion exchange, and absorption, have been widely used in industrial fields and in our daily life. To improve their separation performance, the materials, their processing, and morphology have been investigated worldwide. In this work, we suggest the use of a “microhoneycomb” structure as a morphology for materials to achieve effective separation. In this chapter, separation techniques, processing, and morphology are introduced, and the significance of this work is explained.

### **1.2 Typical Sorption**

#### **1.2.1 Classification of Sorption**

Sorption, suggested by McBain in 1909, is a phenomenon in which chemicals selectively transfer and are concentrated to the bulk phase of a solid or liquid.<sup>1</sup> This phenomenon mainly occurs by physical interaction and chemical interaction between one phase and another. Adsorption, ion exchange, and chromatography are categorized as sorption; however, according to the McBain’s definition, absorption and membrane separation are also classed as sorption.<sup>1</sup> Among these types of sorption, adsorption, ion exchange, and absorption are widely used in both industrial fields and our daily life to separate pollutants, e.g., toxic compounds, radionuclides, and other undesirable species in fluids. In this section, the separation techniques used in this work, adsorption, ion exchange, and absorption, are introduced.

#### **1.2.2 Adsorption**

Adsorption is the selective transfer and concentration of chemical species, e.g., atoms, ions, and molecules, to a “solid surface,” which is a special case of sorption, mentioned above. The solid phase is called an “adsorbent.” The adsorption is divided into two types according to interaction forces:

physical adsorption (physisorption), which occurs by van der Waals forces, and chemical adsorption (chemisorption), which occurs by a chemical reaction. Because the activation energy of physisorption is low, adsorption rates are fast. In addition, adsorbed species can be easily desorbed by heating, or under a vacuum, because of the low activation energy. On the other hand, because of chemical bond formation resulting from chemisorption, the activation energy of chemisorption is normally higher than that of physisorption. Moreover, due to difficulties in cleaving chemical bonds, the activation energy of desorption is also high. These features make it difficult to recover the chemisorbed species from adsorbents. A huge number of physical/chemical adsorbents have been reported, e.g., carbonaceous materials,<sup>2-4</sup> silica gel,<sup>5</sup> metal oxides,<sup>6, 7</sup> synthetic/natural zeolites,<sup>8-10</sup> and metal-organic frameworks.<sup>11-14</sup> These adsorbents have been applied to purification,<sup>2, 4</sup> dehydration,<sup>10</sup> gas storage<sup>3, 5, 7-9, 11-14</sup> and etc.<sup>6</sup>

### 1.2.3 Ion Exchange

Ion exchange is defined as the exchange of ions between a liquid phase and a solid phase.<sup>15</sup> Ion exchanges of cations and anions are called cation exchange and anion exchange, respectively. The solid phase, in which the ion-exchange reaction occurs, is called an “ion exchanger.” Ion exchangers are roughly divided into two categories: organic ion exchangers and inorganic ion exchangers.<sup>16</sup> Synthesized ion-exchange resins are included in organic ion exchangers. Synthetic and natural zeolites, clays, metal phosphates, and heteropolyacids are included in inorganic ion exchangers. Recently, inorganic and organic supports modified with ion-exchangeable surface groups have also been reported. These ion exchangers have been used in various fields, e.g., desalination of sea water, and the removal and concentration of radionuclides.

### 1.2.4 Absorption

Absorption is the selective transfer and concentration of chemical species to a “liquid.” Absorption can also be classified into two types according to interactions between chemical species and liquids: physical absorption and chemical absorption. Liquids that can show a good absorption performance

are called absorbents. Absorption is widely used to remove gas species, e.g., VOC and acidic/basic gases. Recently, absorbent-supported composites, e.g., supported ionic liquid phases, have been developed. Because these composites can be used as solid sorbents, fixed bed systems can be applied, as for adsorption and ion exchange.

## 1.3 Sorption Process in Industrial Fields

### 1.3.1 Classification of Sorption Process

Various sorption processes have been developed in industrial fields for separation and purification. An example of the classification of adsorption and ion exchange is shown in Table 1.1. Among these classifications, fixed bed systems are widely used in industrial fields because they are easily scaled up, and operations are normally continuous. Various derivatives of fixed bed systems, e.g., fluidized bed, moving bed, and simulated moving bed, are also studied. However, these processes are not widely used compared with the simple fixed bed system because of some difficulties associated with these derivative processes. In this chapter, the features and applications of these processes are explained.

### 1.3.2 Slurry

In slurry sorption in an agitation vessel, adsorbents in powder or particle form (<1 mm in diameter) are added to liquid in a tank or vessel, and the obtained slurries are mixed.<sup>1,17</sup> After reaching concentrations of target compounds to specified values, sorbents are separated by filtration or sedimentation processes. Normally, spent sorbents are not recovered. Because of the simplicity of the system, the scaling-up and design of these systems are easy. The most important application of batch systems is the removal of dyes, pollutants, and odors from water. For the removal of high-molecular-weight species, the contact time is long because of their slow sorption rate. To reduce the contact time, small particles are used in slurry systems.

**Table 1.1** Classification of sorption processes [summarized from<sup>1, 17-19</sup>]

	Features	Application
Slurry	<ul style="list-style-type: none"><li>• Mainly liquid phase</li><li>• Batch operation</li><li>• Used adsorbents are discarded</li><li>• Single/multiple systems</li></ul>	<ul style="list-style-type: none"><li>• Decolorization of water</li><li>• Deodorization of water</li><li>• Purification of water</li></ul>
Fixed bed	<ul style="list-style-type: none"><li>• Gas/liquid phase</li><li>• Continuous operation</li><li>• Recycles used adsorbents by PSA and TSA operations</li><li>• Ease of scaling-up</li><li>• Trade-off relation between pressure drop and diffusion rate</li></ul>	<ul style="list-style-type: none"><li>• Dehydration of air/solvents</li><li>• Deodorization of water/air</li><li>• Removal of solvent vapors</li><li>• Purification of water</li><li>• Separation of gas species</li></ul>
Fluidized bed	<ul style="list-style-type: none"><li>• Gas/liquid phase</li><li>• Continuous operation</li><li>• Continuous recycling operation</li><li>• Fast flow rate</li><li>• Fast mass/heat transfer</li><li>• Frictional wear of particles and column</li><li>• Difficulty of resident time control</li></ul>	<ul style="list-style-type: none"><li>• Separation of petroleum distillates</li><li>• Separation of hydrocarbons</li><li>• Purification of water</li><li>• Deodorization of water</li></ul>
Moving bed	<ul style="list-style-type: none"><li>• Gas/liquid phase</li><li>• Continuous operation</li><li>• Continuous recycling operation</li><li>• Fast mass/heat transfer</li><li>• Short column height</li></ul>	<ul style="list-style-type: none"><li>• Decolorization of water</li><li>• Purification of water</li></ul>

### 1.3.3 Fixed Bed

In a fixed bed process, solutions containing target components are fed through columns packed with adsorbent particles (or pellets). The adsorbents typically consist of spherical or granular particles with diameters of 0.05 cm to 1.2 cm to minimize the pressure drop caused by fluid flowing.<sup>1</sup> A schematic illustration of typical adsorbate distribution in a column packed with adsorbents is shown in Fig. 1.1. When fluids containing adsorbate are passed through a column packed with particles, firstly, adsorbate is not detected downstream of the flow. The adsorption proceeds in a column, and the region where adsorption is taking place is transferred downstream. This region is called the “mass-transfer zone (MTZ)” or “adsorption zone.” In adsorption fields, about half the length of the MTZ, the length of unused bed (LUB), is also used. When the MTZ reaches the exit point of a column, the adsorbate is detected and its concentration increases until the concentration equals the feed concentration. The concentration profile of a column endpoint, ideally a sigmoidal curve, is called the “breakthrough curve.” In fixed bed operation, a column is recovered when the adsorbate is detected. The standard of the recovery is normally 5 to 10% of the initial concentration.<sup>20</sup>

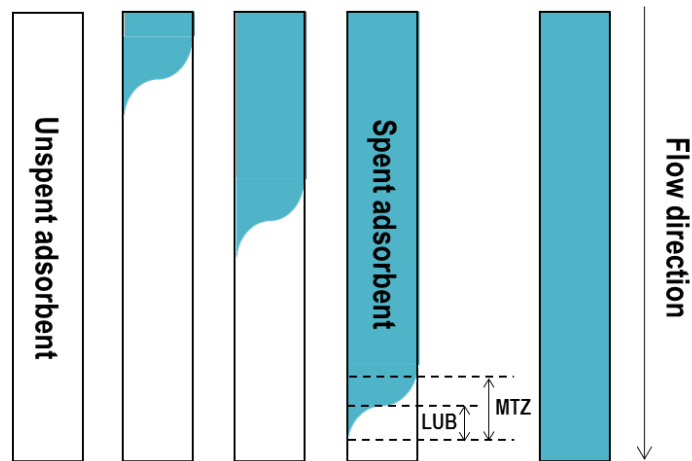


**Fig. 1.1** Schematic illustration of mass-transfer zone in a column

As mentioned above, particles are commonly used in fixed bed systems. When fluids are passed through a column packed with particles, resistance by particles, which is called the hydraulic resistance, occurs. Hydraulic resistance is detected as a pressure drop between the inside of a column

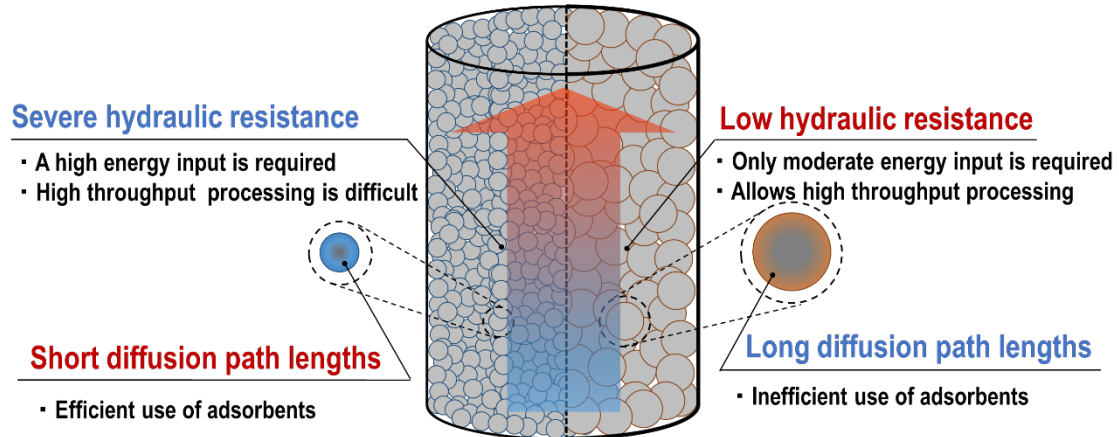
and the outside. In fixed bed systems used in industrial fields, a severe pressure drop should be avoided, because high-performance pumps are needed to continuously and stably pump fluids through a column packed with particles. Degradation of the adsorbents, column, and pipes also presents a problem. Such operation problems are more serious in the case of liquid phase systems, because of a severe hydraulic resistance occurring due to the high viscosity of fluids compared with that of gases. Therefore, comparatively large particles are used in the fixed bed system to reduce the pressure drop. On the other hand, the large particles have long diffusion path lengths compared with smaller particles. Because large particles have long diffusion path lengths, the MTZ in a column packed with particles will be broad. Such a broad MTZ is not desirable in achieving an effective fixed bed adsorption system, because the adsorbents should be recovered when the MTZ reaches the end-point of a column. Small particles make the MTZ short; however, the pressure drop for a column packed with such particles causes severe hydraulic resistance when fluid flows, because the column pressure drop ( $\Delta P$ ) and the square of the particle diameter ( $d_p^2$ ) are inversely proportional (Kozeny-Carman equation,<sup>21</sup> Eq. (1.1)).

$$\Delta P = 36\kappa \frac{(1 - \varepsilon_p)^2 \mu u_s L_p}{\varepsilon_p^3 d_p^2} \quad (1.1)$$

In this equation,  $\kappa$  represents the Kozeny-Carman constant (set to 5),  $\varepsilon_p$  the bed porosity,  $\mu$  the viscosity of the fluids,  $u_s$  the superficial velocity, and  $L_p$  the length of the bed particles.

Considering the relationship between the particle diameter and the hydraulic resistance, a low hydraulic resistance and short diffusion path lengths (= short MTZ length) are not compatible in columns packed with spherical particles (Fig. 1.2). To overcome such a trade-off between the pressure drop and diffusion paths molding of the adsorbents into a special morphology,<sup>22-24</sup> has been developed.

## Adsorption by a column packed with “Particles”



**“Low hydraulic resistance” and “short diffusion path lengths” are not compatible**

**Fig. 1.2** Trade-off relation between hydraulic resistance and diffusion path lengths

### 1.3.4 Fluidized Bed

When the fluid flow rate exceeds a specified value in a column packed with particles, the particles adopt a fluid-like movement, thus are known as a fluidized bed (Fig. 1.3). The specified flow rate is called the minimum fluidization velocity. Because of the fluid-like motion of the particles, fluids can efficiently make contact with particles and adsorption heat can be easily removed. Moreover, the processing speed is fast because of the high flow rate. The ease of heat transfer prevents an increase in the bed temperature; however, such a problem does not occur for adsorption because the reaction heat of adsorption is lower than that of catalytic reactions. A disadvantage of a fluidized bed is that the flow rate must remain faster than the minimized fluidization velocity to maintain the fluidized state. Therefore, control of the residence time is difficult and the separation performance may be lower than that of a typical fixed bed system. Besides, the frictional wear of the particles and the column wall caused by the fluidized particles is also a problem. Now, fluidized bed systems are used for liquid-phase adsorption processes when clogging by suspended matter is a problem.<sup>18, 25</sup>

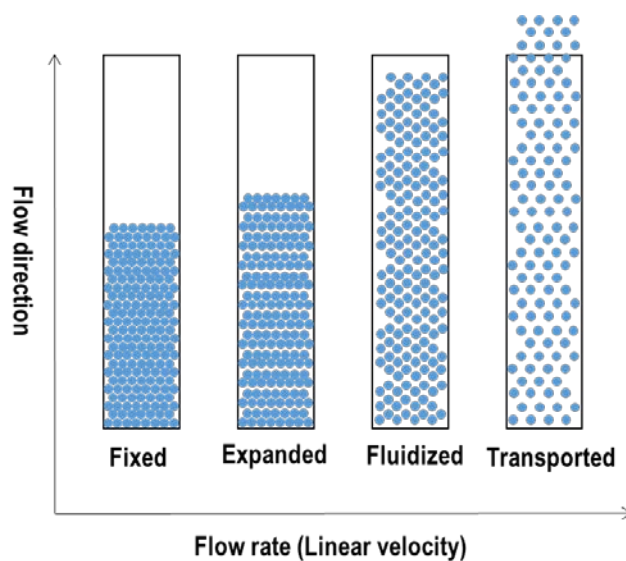


**Fig. 1.3** Illustration of particles in fluidized bed<sup>17,19</sup>

## 1.4 Morphologies of Sorbents

### 1.4.1 Classification of Sorbent Morphology

As mentioned in the previous section, various sorption systems have been developed, and fixed bed systems are widely used in various fields. To effectively utilize sorbents for fixed bed systems, optimization of the sorbent morphologies is important. In this section, the classification of adsorbents, focusing on their morphologies and application, is explained.

### 1.4.2 Particles

Particles are widely used in sorption systems, and they have been optimized for each process. The particles are roughly classified into granular, spherical, and pelletized particles. Granular particles are simply prepared by crushing large particles. The granular particles are affordable; however, it is difficult to uniformly pack them in a column because of the irregularity of their structure. Such an irregularly packed bed causes higher pressure drops and unpredictable fluid flow through a column packed with particles. In fluidized bed systems, micronization of the particles by frictional wear is also a problem. To avoid this, “spherical” particles are widely used in both fixed bed and fluidized-bed

systems.

### 1.4.3 Fibers

Fibrous adsorbents, such as activated carbon fibers (ACFs),<sup>22, 23</sup> have short diffusion path lengths due to their fibrous morphology, and suitable handling properties due to their ease of molding to paper, sheets, and felt-like structures. Because of these beneficial properties for adsorption systems in flow systems, columns packed with fibers are applied to vapor separation and water purification. Fiber-form carbons have been widely reported and applied in industrial fields and our daily-life; however, a fiber is not a suitable morphology for adsorbents because molding of adsorbents into fibers is not easy. ACFs are widely used because precursor polymers, e.g., polyacrylonitrile (PAN), have good flexibility for molding into fiber-form.

### 1.4.4 Monoliths

Monoliths, commonly used as a morphology for three-way catalysts in vehicles, are one option for an adsorbent's morphology (Fig. 1.4).<sup>24, 26-28</sup> A monolith is typically composed of aligned polygonal straight channels (a few mm to a few hundred  $\mu\text{m}$ ) surrounded by thin channel walls (normally thinner than a channel size). The cell density and wall thickness of typical monoliths are  $31\text{--}186\text{ cells}\cdot\text{cm}^{-2}$  and  $0.051\text{--}0.27\text{ mm}$ , respectively.<sup>24</sup> Important features of monoliths are their low pressure drops, fast mass transfer, and high geometric surface area. The straight channels minimize the pressure drop occurring when fluids pass through, and the thin channel walls allow a fast mass-transfer rate and improve the contact efficiency of fluids and solids. These features are preferable for not only catalytic but also adsorption systems.

Various methods have been developed to obtain adsorbents with a monolithic structure, e.g., extrusion, hard/soft-templating method, and self-assemblies. In industrial applications, the extrusion method is commonly used to obtain ceramic-based monoliths. For example, cordierite with a monolithic structure, prepared by using an extrusion method, is widely used for substrates of three-way catalysts. This method is widely applied not only to ceramics but also zeolites, metal oxides, and

polymers. On the other hand, carbon-based monoliths, which have a high potential for use as catalyst supports and adsorbents, are difficult to obtain by simple extrusion. Therefore, thermosetting resins, e.g., phenolic resins, are used as precursors of carbon-based monoliths. Resin is directly extruded, or extruded with binders, to obtain precursor monoliths, or is coated on ceramic monoliths, as mentioned above. After heating precursor monoliths in an inert atmosphere, carbon-based monoliths can be obtained. Monoliths have a high geometric surface area, and this can be increased by reducing the channel size and wall thickness. The adsorption performance can be improved by increasing the geometric surface area; however, it is difficult to obtain monoliths with smaller channel sizes by the extrusion method because of limitations associated with the form block size.

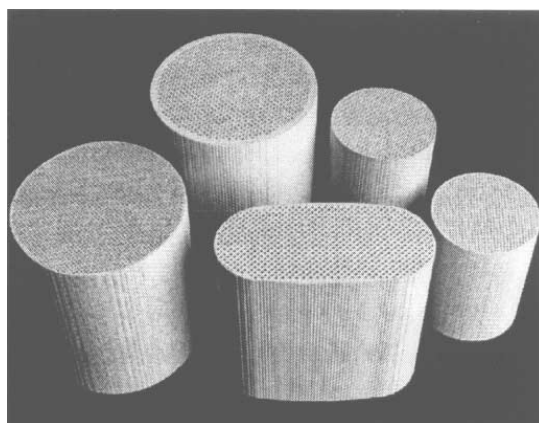


**Fig. 1.4** A photograph of cellular ceramic monoliths.<sup>24</sup> “Catalysis Today, 69 (1-4), Jimmie L. Williams, Reprinted from Monolith structures, materials, properties and uses, 3-9, Copyright (2001), with permission from Elsevier.”

## 1.5 Microhoneycombs

### 1.5.1 Ice-Templating Method

In 1980, Mahler and Bechtold reported silica fibers prepared by unidirectional freezing of silica hydrogel.<sup>29</sup> The polygonal silica fibers were obtained by unidirectional-freezing, thawing, and freeze-drying of silica hydrogels. Not only silica fibers with hexagonal cross-sections, but also ribbed flakes or mixtures of honeycombs and flakes were obtained by changing the hardness of precursor gels, by changing the aging time. They explained that the phase separation of ice crystals and silica occurred.

Zirconia, titania, and alumina fibers were also prepared by these unidirectional freezing techniques.

After that, from 2004 to 2005, Mukai<sup>30</sup> and Nishihara<sup>31</sup> reported monolithic silica with a honeycomb-like structure, prepared by using a unidirectional freezing method, and the monolith was named as “microhoneycomb” (Fig. 1.5). The most important difference compared to Mahler’s method was the hardness of the precursor gels. They froze soft silica hydrogels, which were aged for a short time, as precursors of the monolith. In Mahler’s method, hard silica gels, which were aged for a long time, were frozen. By changing the hardness (aging time) of the precursor hydrogel, silica with lamellar structures, flat fibers, and polygonal fibers were obtained (Fig. 1.6).<sup>32</sup> Mukai and Nishihara’s group named this molding technique as the ice-templating method, because ice crystals substantially act as templates for these morphologies. Template ice crystals can be easily removed by merely thawing, compared with other hard-templating methods using metals, ceramics, and polymers. Therefore, it can be said that the ice templating method is eco-friendly. These groups also reported materials with the microhoneycomb structure (and other morphologies), composed of resorcinol formaldehyde resin,<sup>33</sup> silica,<sup>30, 31</sup> titania,<sup>34</sup> silica-alumina,<sup>35</sup> silica-titania,<sup>36</sup> zeolite-silica,<sup>37</sup> and ion-exchange resin.<sup>38</sup>

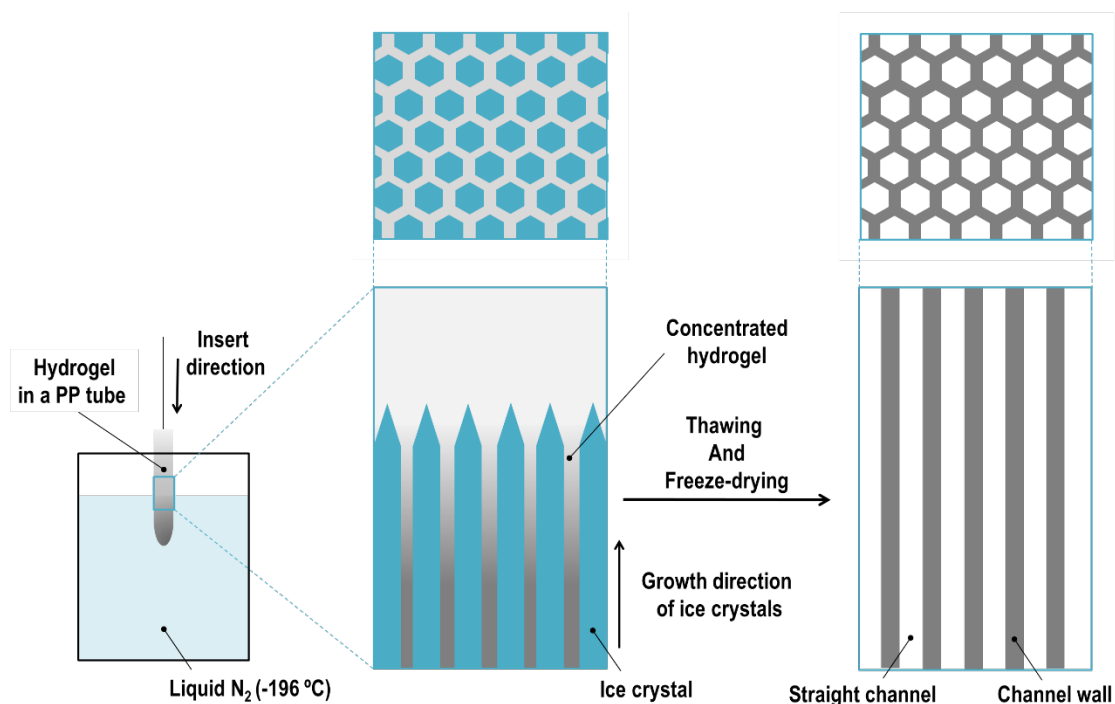


**Fig. 1.5** Formation of a microhoneycomb structure by the ice-templating method

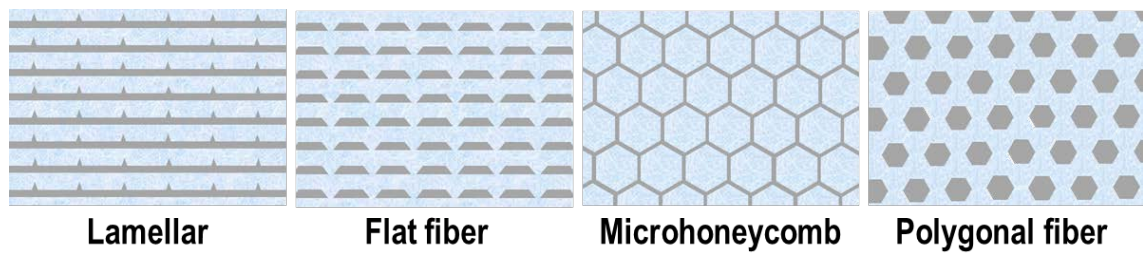
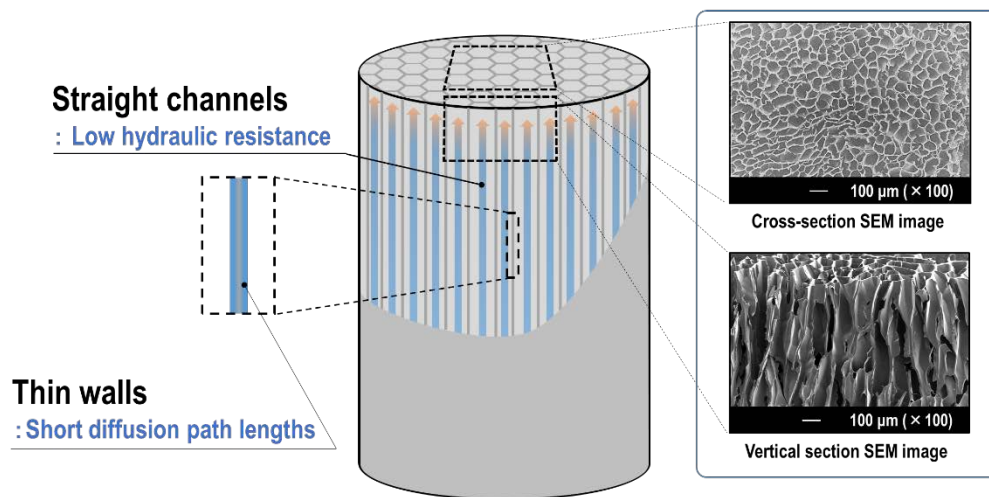


**Fig. 1.6** Morphologies that can be obtained by using the Ice-templating method<sup>39</sup>

### 1.5.2 Features of Microhoneycombs

Among the morphologies that can be synthesized using the ice templating method explained above, the microhoneycomb (MH) structure can be expected to be favorable for processing in flow systems (Fig. 1.7). The MH structure is composed of aligned straight macrochannels, a few tens of  $\mu\text{m}$  in diameter, and thin channel walls, a few  $\mu\text{m}$  in thickness. This MH structure can be regarded as a miniature version of the monoliths mentioned in the previous section. A critical difference when compared with the monolith is that the size of the MH structure is much smaller than that of the monolith. Because of smaller channels and thin channel walls, the geometric surface area (or cell density) is much higher than that of the typical monolith. Although the pressure drop occurring when fluids flow through the MH structure is much higher than that for the monolith, a column packed with particles that have same diffusion path lengths has an extremely severe hydraulic resistance. Therefore, the MH structure has a high potential for use in separation processes in flow systems.

## Adsorption by an adsorbent with a “Microhoneycomb” structure



- “Low hydraulic resistance” and “short diffusion path lengths” are compatible
- Easily synthesized by using “ice crystals” as templates

Fig. 1.7 Features of monolith with a microhoneycomb structure

### 1.5.3 Application of Microhoneycomb

As mentioned above, materials with microhoneycomb structures have a high potential for use in processing in flow systems. Among these systems, adsorption and catalysts are the most important applications. As regards adsorption, Ogino reported the adsorption of 1-butanol by carbon cryogels with a microhoneycomb structure (CMH).<sup>40</sup> With respect to catalysis, Mukai reported an ion-exchange resin with a microhoneycomb structure, and its catalytic performance was also discussed.<sup>38</sup> Murakami reported sulfonated carbon microhoneycombs,<sup>41</sup> and Ogino reported that their porosities and surface properties affected their catalytic activities.<sup>42</sup> Satoh reported sulfonated silica with a microhoneycomb structure.<sup>43, 44</sup> Currently, we have focused on the application of the microhoneycombs for catalysis; however, their application for adsorption is not well studied. Because the microhoneycomb structure has the compatibility of a low hydraulic resistance and short diffusion path lengths, it can be expected that the microhoneycomb has a high potential to be used for adsorption in flow systems.

## 1.6 Objectives and Contents

As mentioned in section 1.2, various sorption techniques, e.g., adsorption, ion exchange, and absorption, are widely used in various fields. To improve their separation performance, various processes have been developed and are widely used in industrial fields (section 1.3). Among these, fixed bed systems in flow systems using a column packed with spherical (or granular, or pelletized) particles are commonly and widely used due to their usability and applicability. However, a low hydraulic resistance and short diffusion path lengths are not compatible for a column packed with typical particles. To overcome such a trade-off relation between hydraulic resistance and diffusion path lengths, monolithic adsorbents were studied (section 1.4).

Recently, we developed monolithic materials with a “microhoneycomb (MH)” structure, which can be regarded as a miniature version of the monolith mentioned in section 1.4. Monoliths with a MH structure have short diffusion path lengths, which can be expected to result in fast mass transfer, and have fairly straight macro channels, which can be expected to show a low hydraulic resistance. Because of this unique morphology, monolithic sorbents with a MH structure have a high potential to be used for the effective separation of diluted pollutants, especially when processing large amounts of fluids. In this dissertation, to demonstrate the potential and applicability of sorbents with a MH structure for effective separation in flow systems, the adsorbents are prepared and applied to the separation of diluted pollutants in liquid and gas systems. The establishment of a preparation procedure for adsorbents with a MH structure is also investigated to widen the application fields of microhoneycombs.

In section 1 (chapter 2), carbon cryogels with a MH structure (CMHs) are applied to the adsorption of organic compounds in batch and flow systems to evaluate their potential to be used for this purpose. Carbonaceous adsorbents have been widely used in various adsorption systems to remove organic compounds from water. In this section, we focused on using carbon gels (CGs) as adsorbents of organic compounds. CGs have high controllability of mesopores, which can improve the diffusion rates of large molecules, such as dyes. In addition, CGs can be easily molded into a MH structure (known as carbon gel microhoneycombs (CMHs)) by applying the ice-templating method to the CG precursor,

resorcinol formaldehyde gels (RF gels).

In chapter 2, phenol and dye adsorption are studied to evaluate the potential of CMHs to be used for continuous separation of diluted organic compounds. The effects of surface properties on the phenol and methylene blue adsorption performance are investigated. The potential of a MH structure to be used for adsorption in flow systems is also investigated.

In section 2 (chapters 3, 4, and 5), the cesium cation ( $\text{Cs}^+$ ) separation performance of various ion exchangers having a MH structure, which can remove  $\text{Cs}^+$  under various conditions, is investigated. The CMHs, studied in the previous section, had a high potential to separate organic compounds because of strong interactions between the organic compounds and carbon. To consider the widening applicability of adsorbents with a MH structure to other targets, e.g., ions and carbonaceous adsorbents, is not appropriate because of poor interaction between ions and carbon surfaces. In addition, it is not always possible to mold inorganic adsorbents, which can selectively adsorb specified ions, into a MH structure. To obtain monolithic materials with a MH structure, gels with appropriate properties, e.g., gel strength, density, and hydrophilicity, are needed. Therefore, the establishment of an appropriate preparation procedure for inorganic adsorbents with a MH structure is also important.

Firstly, in chapter 3, Prussian blue analogues (PBAs), which are thought to be typical  $\text{Cs}^+$  exchangers, supported on microhoneycombs were studied. PBAs are directly synthesized in a silica-alumina hydrogel, which is a precursor of monoliths having a MH structure, and the effect of the PBA content on the formation of a MH structure in precursor gels is studied. The effect of the cation used to prepare PBAs for  $\text{Cs}^+$  adsorption is also studied.

Next, in chapter 4, AMP, one of the heteropoly salts that can selectively adsorb  $\text{Cs}^+$ , supported on silica microhoneycombs (SMHs) (AMP-SMHs), is studied. AMP can selectively remove  $\text{Cs}^+$  from solutions at low pH, and is stable at high temperature. Fine AMP particles are directly supported on and into the channel wall of the MH by a simple mixing method. The effect of various parameters, e.g., monolith length, superficial velocities, AMP contents, and feed concentration, on the  $\text{Cs}^+$  adsorption performance are also studied. Simulational comparisons with a typical column packed with particles are also conducted.

Finally, in chapter 5, Cs<sup>+</sup> separation by RF gels with a MH structure (RFMHs), which can adsorb Cs<sup>+</sup> under high pH conditions, are studied. PBAs, AMP, silica-alumina, and silica, which are used in chapters 5 and 6, are unstable at high pH. Cs<sup>+</sup>-contaminated water at high pH can be produced by incineration of Cs-containing wastes. Therefore, Cs<sup>+</sup> adsorbents that can act and be stable at high pH are needed. The effects of the preparation conditions and solution pH on the Cs<sup>+</sup> separation performance of RFMHs were studied.

In section 3 (chapter 6), ionic liquids (ILs) loaded on silica microhoneycombs (IL-SMHs) are studied to remove diluted CO<sub>2</sub> in the gas phase. Currently, CO<sub>2</sub> absorption by various ILs is reported because of their good CO<sub>2</sub> adsorption performance and their tunability with respect to physical and chemical properties. To improve the performance of ILs, supported ILs (SILPs), ILs thinly coated on porous supports, are suggested. In this section, ILs supported on silica microhoneycombs (IL-SMHs) are prepared and their CO<sub>2</sub> adsorption performances are evaluated in batch and flow systems.

In the conclusion section (chapter 7), the results and conclusions obtained from each chapter are summarized, and the potential of adsorbents with a microhoneycomb structure to be used for flow adsorption systems is discussed.

## 1.7 Reference

1. Henley, E. J.; Seader, J. D.; Roper, D. K., *Separation Process Principles 3rd ed. International Student Version*. Wiley: 2011.
2. Dąbrowski, A.; Podkościelny, P.; Hubicki, Z.; Barczak, M., Adsorption of Phenolic Compounds by Activated Carbon-A Critical Review. *Chemosphere* **2005**, *58* (8), 1049-1070.
3. Dillon, A. C.; Jones, K. M.; Bekkedahl, T. A.; Kiang, C. H.; Bethune, D. S.; Heben, M. J., Storage of Hydrogen in Single-Walled Carbon Nanotubes. *Nature* **1997**, *386* (6623), 377-379.
4. Hameed, B. H.; Din, A. T. M.; Ahmad, A. L., Adsorption of Methylene Blue onto Bamboo-Based Activated Carbon: Kinetics and Equilibrium Studies. *J. Hazard. Mater.* **2007**, *141* (3), 819-825.
5. Leal, O.; Bolívar, C.; Ovalles, C.; García, J. J.; Espidel, Y., Reversible Adsorption of Carbon Dioxide on Amine Surface-Bonded Silica Gel. *Inorg. Chim. Acta* **1995**, *240* (1), 183-189.
6. Kenausis, G. L.; Vörös, J.; Elbert, D. L.; Huang, N.; Hofer, R.; Ruiz-Taylor, L.; Textor, M.; Hubbell, J. A.; Spencer, N. D., Poly(l-lysine)-g-Poly(ethylene glycol) Layers on Metal Oxide Surfaces: Attachment Mechanism and Effects of Polymer Architecture on Resistance to Protein Adsorption. *J. Phys. Chem. B* **2000**, *104* (14), 3298-3309.

7. Busca, G.; Lorenzelli, V., Infrared spectroscopic identification of species arising from reactive adsorption of carbon oxides on metal oxide surfaces. *Mater. Chem.* **1982**, 7 (1), 89-126.
8. Cavenati, S.; Grande, C. A.; Rodrigues, A. E., Adsorption Equilibrium of Methane, Carbon Dioxide, and Nitrogen on Zeolite 13X at High Pressures. *J. Chem. Eng. Data* **2004**, 49 (4), 1095-1101.
9. Siriwardane, R. V.; Shen, M.-S.; Fisher, E. P.; Losch, J., Adsorption of CO<sub>2</sub> on Zeolites at Moderate Temperatures. *Energy Fuels* **2005**, 19 (3), 1153-1159.
10. Pelmenschikov, A. G.; van Santen, R. A., Water Adsorption on Zeolites: ab-initio Interpretation of IR Data. *J. Phys. Chem.* **1993**, 97 (41), 10678-10680.
11. Millward, A. R.; Yaghi, O. M., Metal–Organic Frameworks with Exceptionally High Capacity for Storage of Carbon Dioxide at Room Temperature. *J. Am. Chem. Soc.* **2005**, 127 (51), 17998-17999.
12. Noro, S. i.; Kitagawa, S.; Kondo, M.; Seki, K., A New, Methane Adsorbent, Porous Coordination Polymer [ $\{CuSiF_6(4,4\text{-bipyridine})_2\}_n$ ]. *Angew. Chem., Int. Ed.* **2000**, 39 (12), 2081-2084.
13. Matsuda, R.; Kitaura, R.; Kitagawa, S.; Kubota, Y.; Belosludov, R. V.; Kobayashi, T. C.; Sakamoto, H.; Chiba, T.; Takata, M.; Kawazoe, Y.; Mita, Y., Highly Controlled Acetylene Accommodation in a Metal-Organic Microporous Material. *Nature* **2005**, 436 (7048), 238-241.
14. Kaye, S. S.; Dailly, A.; Yaghi, O. M.; Long, J. R., Impact of Preparation and Handling on the Hydrogen Storage Properties of Zn<sub>4</sub>O(1,4-benzenedicarboxylate)<sub>3</sub> (MOF-5). *J. Am. Chem. Soc.* **2007**, 129 (46), 14176-14177.
15. Perry, R. H.; Green, D. W.; Maloney, J. O., *Chemical Engineers' Handbook Eighth Edition*. McGraw-Hill: 2007.
16. Helfferich, F. G., *Ion Exchange*. McGraw-Hill: 1962.
17. Takeuchi, Y., *KYUCHAKUBUNRI*. BAIFUKAN CO., LTD: Tokyo, 2000.
18. Hashimoto, K.; Ogino, F., *GENDAIKAGAKUKOGAKU*. SANGYOTOSHO: 2001.
19. Ono, Y.; Suzuki, I., *KYUCHAKU NO KAGAKU TO OUYOU*. KODANSHA Ltd.: Tokyo, 2003.
20. Kagakukogakukyokai, *KAGAKUKOGAKUBINRAN*. 4th ed.; MARUZEN-YUSHODO Company, Limited: 1978.
21. Kozeny, J., Ueber kapillare leitung des wassers im boden. *Sitzungsber. Akad. Wiss. Wien* **1927**, 136, 271-306.
22. Le Cloirec, P., Adsorption onto Activated Carbon Fiber Cloth and Electrothermal Desorption of Volatile Organic Compound (VOCs): A Specific Review. *Chin. J. Chem. Eng.* **2012**, 20 (3), 461-468.
23. Suzuki, M., Activated Carbon Fiber: Fundamentals and Applications. *Carbon* **1994**, 32 (4), 577-586.
24. Williams, J. L., Monolith Structures, Materials, Properties and Uses. *Catal. Today* **2001**, 69 (1-4), 3-9.
25. Fernández, N.; Montalvo, S.; Borja, R.; Guerrero, L.; Sánchez, E.; Cortés, I.; Colmenarejo, M. F.; Travieso, L.; Raposo, F., Performance Evaluation of an Anaerobic Fluidized Bed Reactor with Natural

Zeolite as Support Material When Treating High-strength Distillery Wastewater. *Renewable Energy* **2008**, *33* (11), 2458-2466.

26. Crittenden, B.; Patton, A.; Jouin, C.; Perera, S.; Tennison, S.; Echevarria, J. A. B., Carbon Monoliths: A Comparison with Granular Materials. *Adsorption* **2005**, *11* (S1), 537-541.

27. Crittenden, B.; Perera, S.; Mays, T.; Camus, O.; Tennison, S., Monolithic Adsorbents in Sustainable Development. *World Congress of Chemical Engineering, 7th*, **2005**.

28. Patton, A.; Crittenden, B. D.; Perera, S. P., Use of the Linear Driving Force Approximation to Guide the Design of Monolithic Adsorbents. *Chem. Eng. Res. Des.* **2004**, *82* (8), 999-1009.

29. Mahler, W.; Bechtold, M. F., Freeze-formed Silica Fibres. *Nature* **1980**, *285* (5759), 27-28.

30. Mukai, S. R.; Nishihara, H.; Tamon, H., Formation of Monolithic Silica Gel Microhoneycombs (SMHs) Using Pseudosteady State Growth of Microstructural Ice Crystals. *Chem. Commun.* **2004**, (7), 874-875.

31. Nishihara, H.; Mukai, S. R.; Yamashita, D.; Tamon, H., Ordered Macroporous Silica by Ice Templating. *Chem. Mater.* **2005**, *17* (3), 683-689.

32. Mukai, S. R.; Nishihara, H.; Tamon, H., Porous Properties of Silica Gels with Controlled Morphology Synthesized by Unidirectional Freeze-Gelation. *Microporous Mesoporous Mater.* **2003**, *63* (1-3), 43-51.

33. Mukai, S. R.; Nishihara, H.; Yoshida, T.; Taniguchi, K.-i.; Tamon, H., Morphology of Resorcinol-formaldehyde gels obtained through ice-templating. *Carbon* **2005**, *43* (7), 1563-1565.

34. Mukai, S. R.; Nishihara, H.; Shichi, S.; Tamon, H., Preparation of Porous TiO<sub>2</sub> Cryogel Fibers through Unidirectional Freezing of Hydrogel Followed by Freeze-Drying. *Chem. Mater.* **2004**, *16* (24), 4987-4991.

35. Nishihara, H.; Mukai, S. R.; Fujii, Y.; Tago, T.; Masuda, T.; Tamon, H., Preparation of Monolithic SiO<sub>2</sub>-Al<sub>2</sub>O<sub>3</sub> Cryogels with Inter-Connected Macropores through Ice Templating. *J. Mater. Chem.* **2006**, *16* (31), 3231-3236.

36. Nishihara, H.; Mukai, S. R.; Shichi, S.; Tamon, H., Preparation of Titania-Silica Cryogels with Controlled Shapes and Photocatalysis through Unidirectional Freezing. *Mater. Lett.* **2010**, *64* (8), 959-961.

37. Mukai, S. R.; Mitani, K.; Murata, S.; Nishihara, H.; Tamon, H., Assembling of Nanoparticles Using Ice Crystals. *Mater. Chem. Phys.* **2010**, *123* (2-3), 347-350.

38. Mukai, S. R.; Satoh, Y., Development of a Strong Acid Ion Exchange Resin with a Monolithic Microhoneycomb Structure Using the Ice Templating Method. *Ind. Eng. Chem. Res.* **2010**, *49* (21), 10438-10441.

39. Nishihara, H., Ph.D., Ph.D. Dissertation. Kyoto University: Japan, 2005.

40. Ogino, I.; Kazuki, S.; Mukai, S. R., Marked Increase in Hydrophobicity of Monolithic Carbon Cryogels via HCl aging of precursor resorcinol-formaldehyde hydrogels: Application to 1-butanol

Recovery from Dilute Aqueous Solutions. *J. Phys. Chem. C* **2014**, *118* (13), 6866-6872.

41. Murakami, K.; Satoh, Y.; Ogino, I.; Mukai, S. R., Synthesis of a Monolithic Carbon-Based Acid Catalyst with a Honeycomb Structure for Flow Reaction Systems. *Ind. Eng. Chem. Res.* **2013**, *52* (44), 15372-15376.

42. Ogino, I.; Suzuki, Y.; Mukai, S. R., Tuning the Pore Structure and Surface Properties of Carbon-Based Acid Catalysts for Liquid-Phase Reactions. *ACS Catal.* **2015**, 4951-4958.

43. Satoh, Y.; Yokoyama, Y.; Ogino, I.; Mukai, S. R., Synthesis of Sulfonic Acid Functionalized Silica Honeycombs. *Ind. Eng. Chem. Res.* **2013**, *52* (44), 15293-15297.

44. Satoh, Y., Ph.D. Dissertation. Hokkaido University: Japan, 2014.



## *Part 1*

# *Separation of Organic Compounds in Flow Systems Using Carbon Cryogel with a Microhoneycomb Structure*



# ***Chapter 2***

## ***Phenol and Methylene Blue Adsorption in Flow Systems Using Carbon Cryogels with a Microhoneycomb Structure***

### **2.1 Introduction**

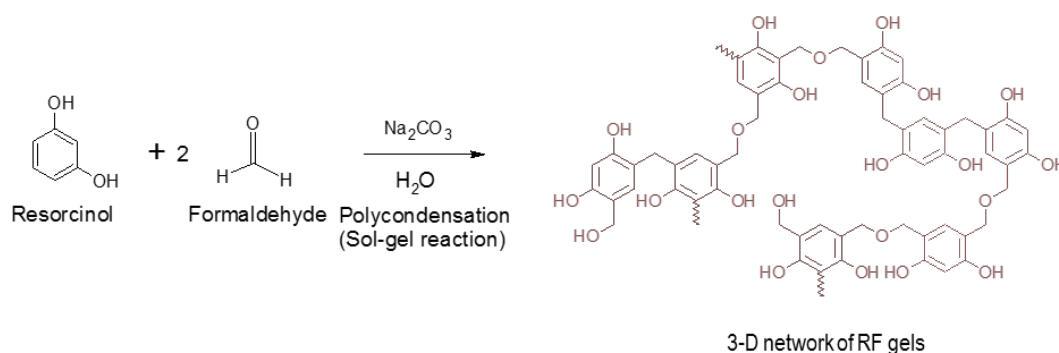
Water soluble aromatic compounds, e.g. phenol derivatives and various dyes emitted from petroleum and coal refining plants and chemical plants are harmful to human health and environment, therefore, emission of these compounds is strictly controlled (e.g. phenol < 5 ppm in Japan<sup>1</sup>). Various removal techniques of have been studied, for example, adsorption,<sup>2-4</sup> membrane separation,<sup>5</sup> biodegradation<sup>6</sup> and oxidative degradation.<sup>7</sup> Among these techniques, adsorption using carbonaceous materials such as activated carbons derived from biomass, coals and synthetic resins are widely used to remove organic contaminants including phenolic and dyes existing in aqueous solutions.<sup>2-4</sup>

In this work, we applied carbon gels (CGs), which are categorized as porous carbons such as ACs, to adsorbents for organic contaminants. Most important difference when compared with ACs is that mesopores of CGs can be easily controlled by changing precursor composition. CGs were obtained by carbonization of resorcinol-formaldehyde (RF) gels, precursors of CGs, by Pekala and co-workers in 1980s.<sup>8-10</sup> RF gels are synthesized by a polycondensation reaction between resorcinol (*p*-benzenediol, HO(C<sub>6</sub>H<sub>4</sub>)OH) and formaldehyde (HCHO) catalyzed by sodium carbonate (Na<sub>2</sub>CO<sub>3</sub>) (Scheme 2.1). CGs can be obtained by carbonization of the RF gels in inert atmosphere. CGs are composed of small carbon nanoparticles (1<sup>st</sup> particles) and their aggregates (2<sup>nd</sup> particles). Micropores and mesopores are voids of the 1<sup>st</sup> particles and 2<sup>nd</sup> particles, respectively (Fig. 2.1). CGs have hierarchical pore structures in which short micropores directly connected to the mesopores. Most important features of the CGs are their mesopores are monodisperse and the pore size can be simply controlled by changing monomer/catalyst ratio of the precursor RF gels. Commonly, this ratio is called *R/C* whose *R* and *C* represents mole of resorcinol (monomer) and Na<sub>2</sub>CO<sub>3</sub> (catalyst). The mechanism of the pore

construability is explained as size of the 2<sup>nd</sup> particles. At low *R/C*, whole monomers can react with each other, therefore, the size of the 2<sup>nd</sup> particles are comparatively small. On the other hand, at high *R/C*, the size of the 2<sup>nd</sup> particles comparatively large because the catalyst amount is low. Void volume of large 2<sup>nd</sup> particles is large and opposite for small particles. Therefore, the mesopore size is large at high *R/C* and small at small *R/C*. Because of the pore controllability of the CGs, they have been applied to various fields, e.g. energy storage devices,<sup>11</sup> catalyst supports<sup>12</sup> and adsorbents.<sup>13</sup>

Previously, we reported that synthesis of CGs having microhoneycomb structure (CMHs) by applying the ice-templating method to RF gels.<sup>14</sup> In this work, to verify the applicability of CMHs to adsorption in continuous flow systems, firstly, the pressure drop which occurs when fluids are passed through them was measured. Next, the adsorption of phenol and methylene blue (one of typical dye) from an aqueous media in batch and continuous flow systems using a CMH was demonstrated. CMHs carbonized at various temperatures were used to clarify how their surface properties affect adsorption abilities. By these experiments, we intend to show that CMHs can be used for continuous separation of organic contaminants without causing a severe hydraulic resistance.

**Scheme 2.1** Synthesis of RF gels by polycondensation reaction of resorcinol and formaldehyde



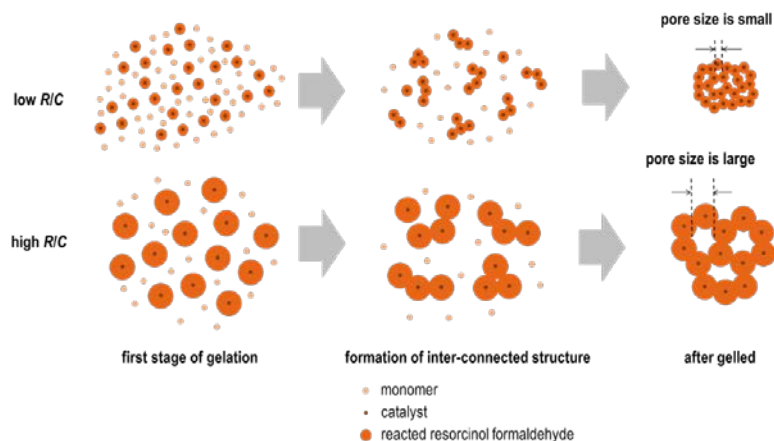


Fig. 2.1 Relationship between porous structure and  $R/C$  value<sup>15</sup>

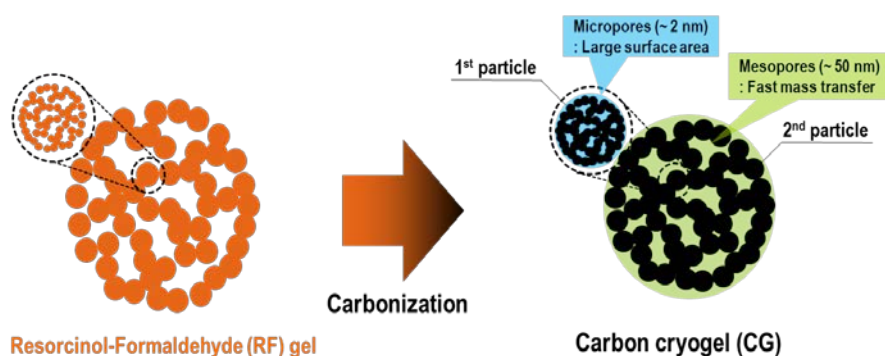


Fig. 2.2 Hierarchal porous structures of carbon gels

## 2.2 Materials and Methods

### 2.2.1. Materials

Resorcinol, formaldehyde solution, sodium carbonate, 2-methyl-2-propanol (*tert*-butyl alcohol, TBA) and phenol were purchased from Wako Pure Chemical Industries, Ltd., Japan. Methylene blue was purchased from KANTO CHEMICAL Co., Ltd., Japan. All reagents were used as received.

### 2.2.2. Preparation of CMHs

CMHs were prepared according to our previous report.<sup>16</sup> Firstly, a resorcinol-formaldehyde (RF) cryogel was prepared through the polycondensation of resorcinol with formaldehyde using sodium

carbonate as a catalyst. Resorcinol (R) was dissolved in deionized-water (W), and sodium carbonate (C) was added to the mixture. After a transparent mixture was obtained, formaldehyde (F) was added to the mixture. The molar ratios between these 4 components (R:F:C:W) were set to 1:2:0.005:61. The obtained mixture was poured into a glass tube (40 mm × 8 mm i.d.) sealed with a rubber cap, and kept at 303 K for 39 h. The obtained RF hydrogel was released from the glass tube and was washed with deionized water for 1 h to remove excess reactants and catalyst. Then, the RF hydrogel was put into a polypropylene tube (125 mm × 13 mm i.d.), and unidirectionally dipped into a liquid nitrogen bath (77 K) at a constant rate (60 mm·h<sup>-1</sup>). After the tube was completely frozen, the frozen hydrogel was released from the tube, thawed at room temperature and cut into portions of several centimeters. The obtained RF hydrogel was immersed in 1 mol·L<sup>-1</sup> hydrochloric acid for 4 days for aging, and then washed with an excess amount of deionized water to completely remove the hydrochloric acid. After washing, the RF hydrogel was immersed in TBA for 2 days to replace the water in it with this alcohol. The TBA was exchanged three times during this treatment. Then, the obtained gel was freeze-dried at 263 K for 2 days. After drying, the obtained monolithic RF gel was carbonized at 673-1273 K for 4 h under a nitrogen flow (100 mL·min<sup>-1</sup>).

### 2.2.3. Characterization of the CMHs

The morphology of the synthesized CMHs was characterized using a scanning electron microscope (SEM, JSM-5410, JEOL Ltd.).

Porous properties of the CMHs were evaluated through nitrogen adsorption-desorption experiments conducted at 77 K using an automatic nitrogen adsorption apparatus (BELSORP-mini, BEL Japan Inc.). Crushed CMH samples were loaded in Pyrex tubes and were heated at 523 K for 4 h under a nitrogen flow of 20 mL·min<sup>-1</sup> to remove adsorbed species from the samples before measurements.

Water vapor adsorption experiments were conducted at 298 K using an automatic adsorption apparatus (BELSORP-max, BEL Japan Inc.) to evaluate surface properties of the CMHs. Samples were loaded in Pyrex tubes and were pretreated by heating at 523 K for 4 h under vacuum before

measurements.

The hydraulic resistance of the CMHs was evaluated by the pressure drop which occurs when water was passed through them. A CMH monolith was fixed in a heat shrinkable tube and water was fed to the monolith at a superficial velocity set in the range of 0 to 12.0 cm·min<sup>-1</sup> using a HPLC pump (PU-2080, JASCO Corporation, Japan). The pressure drop was measured using a pressure sensor (PA-853, Copal Electronics, Japan). The pressure drop that CMHs cause was compared with that a capillary and a column packed with particles respectively cause.

The pressure drop a capillary causes was estimated by the pressure drop a laminar flow in a straight tube causes which can be calculated using the Hagen-Poiseuille equation (2.1).

$$\Delta P = \frac{32\mu u_s L}{\varepsilon D^2} \quad (2.1)$$

Here,  $\Delta P$ ,  $L$ ,  $\mu$ ,  $u_s$ ,  $\varepsilon$  and  $D$ , respectively denotes the pressure drop, the tube length, the viscosity of water, the superficial velocity, the porosity and the tube diameter. In this calculation, the length of the CMH was used as  $L$  and the porosity calculated from cross-sectional SEM image was used as  $\varepsilon$  (= 0.85).

The pressure drop a column packed with particles causes was calculated using the Kozeny-Carman equation (2).

$$\Delta P = 36k \frac{(1 - \varepsilon)^2}{\varepsilon^3} \frac{\mu u_s L}{D_p^2} \quad (2.2)$$

Here,  $k$ ,  $\varepsilon$ ,  $L$  and  $D_p$  respectively denotes the Kozeny-Carman constant (set to 5), the bed porosity (set to a typical value of 0.4), the length of the fixed bed and the particle diameter. In this calculation,  $L$  was set to the length of a column packed with particles having the same total weight as the CMH.

#### 2.2.4. Adsorption of Phenol and MB on the CMHs

Adsorption experiments using CMHs were conducted in both batch and continuous flow systems. In batch experiments, 15 mg of a crushed CMH was added to a 25 mL phenol or methylene blue (MB) aqueous solution having a specified concentration and the obtained slurry was placed in a thermostatic bath which was maintained at 303 K and was shaken at 100 rpm for 7 days (SHK-101B and CTR-320,

IWAKI CO., LTD.). After 7 days, the crushed CMH was separated from the solution by centrifugation at 300 rpm for 5 min. The phenol or MB concentrations of the obtained solutions were measured using a UV-vis spectrometer (UV-2400PC, Shimadzu Corp., wavelength: 270 nm for phenol, 665 nm for MB). The background of deionized water were measured before UV-vis measurements.

The obtained isotherms were analyzed using the Langmuir model (2.3).

$$q = \frac{q_0 K_L C_e}{1 + K_L C_e} \quad (2.3)$$

Here,  $q$ ,  $q_0$ ,  $K_L$  and  $C_e$ , respectively denotes the uptake of phenol and MB, the monolayer capacity, the Langmuir constant, and the phenol or MB concentrations at equilibrium.

In experiments using continuous flows, a monolithic CMH was fixed in a heat shrinkable tube in a similar manner as in pressure drop measurement experiments (Fig. 1). One side of the tube holding the CMH was connected to an HPLC pump, and the opposite side was connected to a UV-vis detector (SPD-10A VP, Shimadzu Corp., wavelength: 270 nm for phenol, 600 nm for MB). The tube holding the CMH was set vertically in an HPLC oven (CTO-10A VP, Shimadzu Corp.) and was kept at 303 K. An aqueous solution was fed to the CMH at a superficial velocity set in the range 1.0 to 3.0  $\text{cm} \cdot \text{min}^{-1}$ . From the breakthrough curves, the length of unused bed (LUB) values were calculated using the following equation (2.4).

$$LUB = \frac{L}{t_s} (t_s - t_b) \quad (2.4)$$

Here,  $L$ ,  $t_s$  and  $t_b$ , respectively denotes the monolith length, the stoichiometric time and the breakthrough time where  $C \cdot C_f^{-1} = 0.05$ .  $C$  and  $C_f$ , respectively denotes the phenol or MB concentrations and the feed concentration. The stoichiometric time is calculated using the following equation (2.5).

$$t_s = \int_0^{t_e} (1 - C/C_f) dt \quad (2.5)$$

Here,  $t_e$  denotes the breakthrough time which is the time when  $C \cdot C_f^{-1}$  reaches 0.95. The “stoichiometric time” represents the time when half of the adsorbent is consumed for adsorption. If the breakthrough curve is a point symmetric sigmoidal, the stoichiometric time will be equal to 50 %

of the breakthrough time.

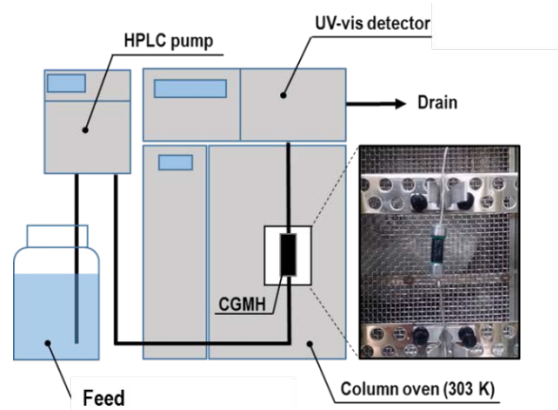


**Fig. 2.3** Experimental apparatus for phenol adsorption in flow systems. The photograph shows a CMH set in a column oven.

## 2.3 Results and Discussion

### 2.3.1. Characterization of the CMHs

The obtained CMHs were black monoliths with a cylindrical shape whose lengths were a few cm and diameters a few mm (Fig. 2, inset). The CMHs had aligned straight channels 25-45  $\mu\text{m}$  in diameter which are expected to show low hydraulic resistances (Fig.2). The thickness of the walls were 5-10  $\mu\text{m}$ , so the mass transfer resistance the walls cause are expected to be extremely low.

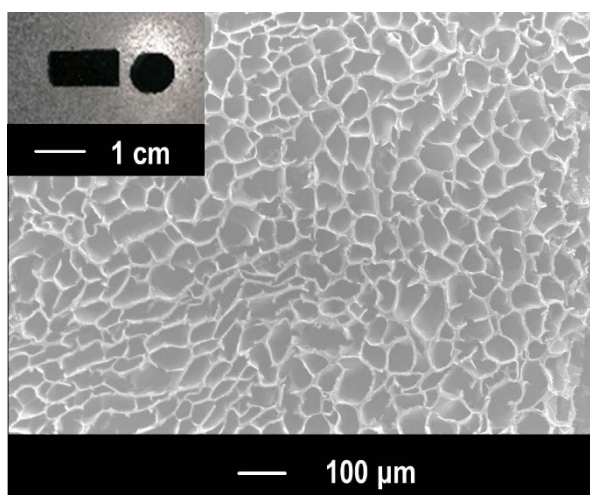


**Fig. 2.4** Cross-sectional SEM image of a CMH carbonized at 1273 K. The inset shows a photograph of the CMH

To evaluate the hydraulic resistance of a CMH, the pressure drop which occurs when water was passed through it was measured. The pressure drop linearly increases with the increase in the superficial velocity of water (Fig. 3). The Hagen-Poiseuille equation suggests that the hydraulic resistance a CMH causes is equivalent to that a capillary with a diameter of 37  $\mu\text{m}$  causes. This diameter is similar to the averaged channel diameter of the CMH estimated from SEM images. Next, to compare the pressure drop the CMH causes with that a typical column packed with particles causes, the latter was calculated using the Kozeny-Carman equation. In the calculation, the particle diameter was set to 5  $\mu\text{m}$  which is equivalent to the wall thickness of the CMH. The calculated pressure drop was 370 times higher than that of the CMH on the same mass basis. These results suggest that CMHs can continuously process a large amount of fluids without high energy inputs compared with a column packed with particles.

Figure 2.6 and Table 2.1 show  $\text{N}_2$  adsorption-desorption isotherms and porous properties of the obtained CMH, respectively. The isotherms are of type IV according to the IUPAC classification which indicates the existence of micropores and mesopores in the materials. Brunauer-Emmett-Teller (BET) surface area ( $S_{\text{BET}}$ ) of the samples increases with the increase in carbonization temperature because of the development of micropores by carbonization. On the other hand, mesopore volume ( $V_{\text{Meso}}$ ) decreases with the increase in carbonization temperature because of the shrinking of the samples caused by carbonization. The total pore volume does not drastically change because the shrinkage of mesopores are compensated by the development of the micropores.

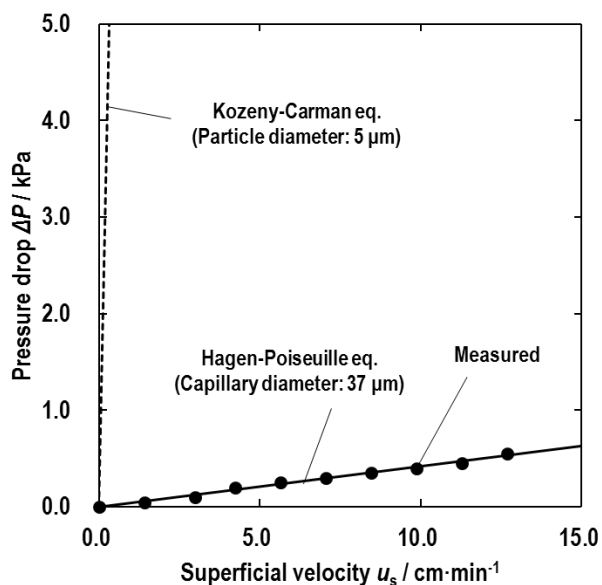


**Fig. 2.5** Pressure drop which a CMH causes when water is passed through it (black circle). The black line represents the pressure drop a tube 37  $\mu\text{m}$  in diameter causes which was calculated using the Hagen-Poiseuille equation. The dashed line represents the pressure drop a column packed with 5  $\mu\text{m}$  diameter particles causes, calculated using the Kozeny-Carman equation.

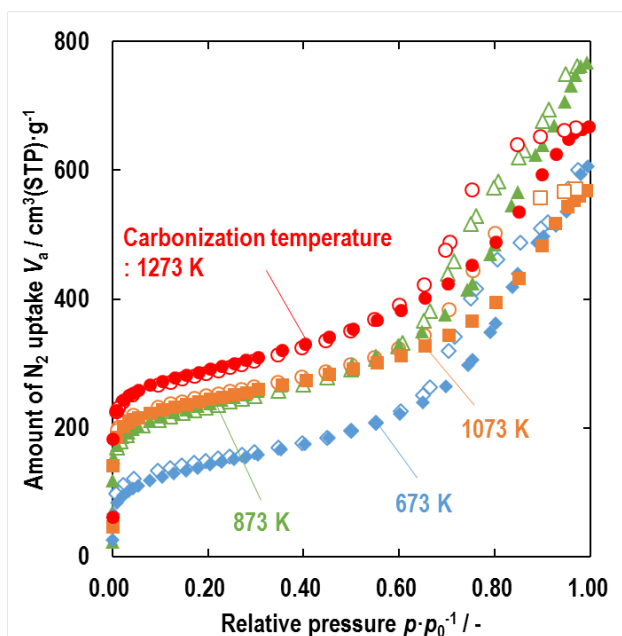


**Fig. 2.6** Nitrogen adsorption-desorption isotherms of CMHs carbonized at 673 K (blue diamond), 873 K (green triangle), 1073 K (orange square) and 1273 K (red circle). Solid and open symbols represent adsorption and desorption branches, respectively.

**Table 2.1** Porous properties of CMH carbonized at 673 to 1273 K

$T / \text{K}$	BET surface area $S_{\text{BET}} / \text{m}^2 \cdot \text{g}^{-1}$	Micropore volume $V_{\text{Micro}}^a / \text{cm}^3 \cdot \text{g}^{-1}$	Mesopore volume $V_{\text{Meso}}^b / \text{cm}^3 \cdot \text{g}^{-1}$	Total pore volume $V_{\text{Total}}^c / \text{cm}^3 \cdot \text{g}^{-1}$
673	513	0.20	0.73	0.93
873	866	0.35	0.84	1.2
1073	903	0.37	0.51	0.88
1273	1070	0.44	0.59	1.0

<sup>a</sup>Calculated from the adsorbed volume of N<sub>2</sub> at  $p/p_0 = 0.15$ , <sup>b</sup> $V_{\text{Total}} - V_{\text{Micro}}$ , <sup>c</sup>Calculated from the adsorbed volume of N<sub>2</sub> at  $p/p_0 = 0.98$ .

**Table 2.2** Ratio of water vapor and N<sub>2</sub> uptake at  $p/p_0 = 0.15$ 

$T / \text{K}$	Adsorption amount of water vapor $V_{\text{H}_2\text{O}}^a / \text{cm}^3(\text{STP}) \cdot \text{g}^{-1}$	Adsorption amount of nitrogen $V_{\text{N}_2}^b / \text{cm}^3(\text{STP}) \cdot \text{g}^{-1}$	$x_{0.15}(\text{H}_2\text{O})$ / %
673	46.3	134	34.6
873	19.6	229	8.56
1073	5.50	337	1.63
1273	2.71	282	0.96

<sup>a</sup> Measured from water vapor adsorption at 298 K, <sup>b</sup> Measured from N<sub>2</sub> adsorption at 77 K.

### 2.3.2. Phenol and MB Adsorption Using CMHs in Batch Systems

Figure 5 shows phenol uptake curves of CMHs carbonized at 673-1273 K. The uptake drastically increased within 15 min, and then gradually increased for a period of about 1 week especially in CMHs carbonized at temperatures higher than 873 K. Indeed, if extremely small micropores exist within the carbon, such a unique uptake behavior may be observed. However, if additional irreversible reactions involving phenol occur in/on the carbons, such a behavior is also thought to be observed. Grant and King reported that phenol oligomers are actually formed presumably through oxidative coupling reactions and the obtained oligomers are irreversibly adsorbed on activated carbon.<sup>17</sup> In addition, Magne and Walker reported that this reaction mainly occurs at graphene edges where oxygen-containing functional groups do not exist.<sup>18</sup> The fact that the unique uptake behavior was mostly observed in CMHs carbonized at higher temperatures, suggest that the gradual increase is likely to be

caused by irreversible reactions. In CMHs used in this work, the  $x_{0.15}(\text{H}_2\text{O})$  value ( $= V_{\text{H}_2\text{O}}/V_{\text{N}_2}$ ),<sup>19, 20</sup> which represents the surface hydrophilicity of the materials, decreases with the increase in carbonization temperature because of the decrease in the amount of surface groups.

Adsorption isotherms of the CMHs are shown in Fig. 6. In various reports, the phenol adsorption isotherms of various adsorbents, including carbons, can be generally fitted using either the Langmuir model or the Freundlich model<sup>21</sup>. From the comparison of  $R^2$  values of the fitted curves, it was found that phenol adsorption on CMHs can be well represented by the Langmuir model. The phenol maximum uptake ( $q_0$ ) calculated using the Langmuir model increases with the increase in carbonization temperature and reaches a saturated value at around 1073 K.

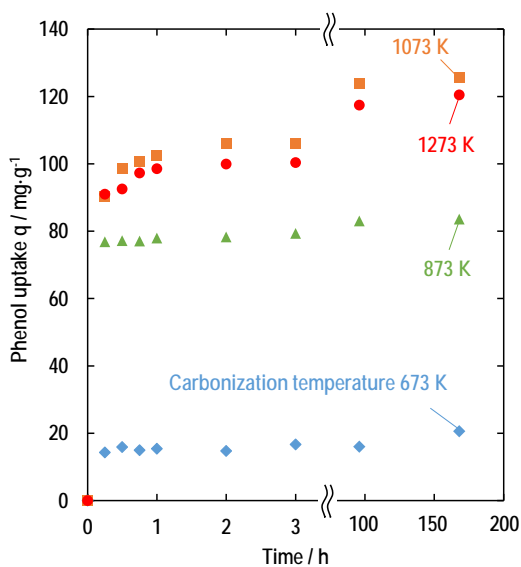


**Fig. 2.7** Phenol uptake curves of CMHs carbonized at 673 K (blue diamond), 873 K (green triangle), 1073 K (orange square) and 1273 K (red circle) at 303 K; initial concentration, 100 ppm; mass-solution ratio, 1.67 L·g<sup>-1</sup>.

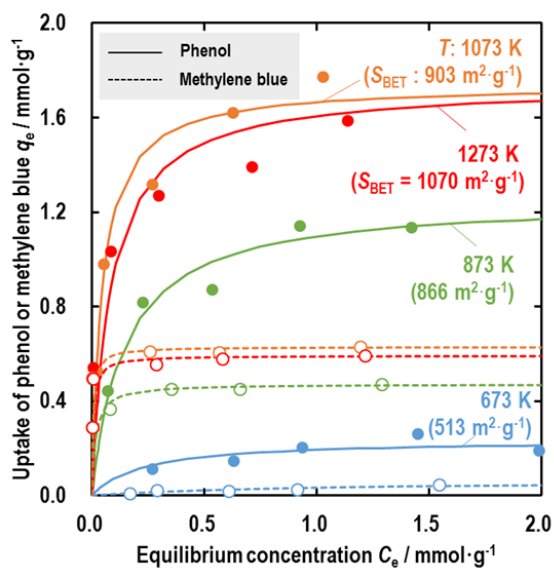


**Fig. 2.8** Equilibrium phenol and methylene blue adsorption isotherms (303 K) of the CMHs carbonized at 673 K (blue diamond), 873 K (green triangle), 1073 K (orange square) and 1273 K (red circle). The solid and dashed lines are phenol and methylene blue curves fitted using the Langmuir model, respectively.

**Table 2.3** Isotherm parameters of phenol and methylene blue  $T / K$

	Phenol			Methylene blue		
	$q_0 / \text{mmol} \cdot \text{g}^{-1}$	$K_L / \text{L} \cdot \text{mmol}^{-1}$	$R^2$	$q_0 / \text{mmol} \cdot \text{g}^{-1}$	$K_L / \text{L} \cdot \text{mmol}^{-1}$	$R^2$
673	0.24	4.49	0.940	0.07	0.91	0.824
873	1.25	7.01	0.995	0.47	61.8	1.000
1073	1.74	22.1	0.999	0.63	173	1.000
1273	1.74	12.1	0.997	0.59	150	1.000

### 2.3.3. Phenol and MB Adsorption Using CMHs in Flow Systems

Phenol breakthrough curves of CMH carbonized at various temperature are shown in Fig. 2.9. The obtained curves show an ideal shape and the LUB values of them were in the range of 0.4-0.7 cm. The ratio of the LUB over the monolith length ( $LUB \cdot L^{-1}$ ) decreases with increasing of the carbonization temperature. If this ratio is small, utilization of monolith for adsorption process is high, therefore, CMHs carbonized at higher temperatures are preferable in continuous flow systems. In CMHs carbonized at higher temperatures (873-1273 K), the ratio of the measured capacity over the theoretical capacity ( $q_B \cdot q_{theor}^{-1}$ ) is 0.8-0.9 which indicates that 10-20 % of the total capacity cannot be used in continuous flow systems. This difference indicates that physisorption mainly occurred in such CMHs because the residence time was very short ( $\sim 30$  s). On the other hand in the CMH carbonized at 673 K,  $q_B \cdot q_{theor}^{-1}$  was close to 1 indicating almost all of the adsorption sites were used. Methylene blue breakthrough curves of CMH carbonized at various temperature are shown in Fig. 2.10. The obtained curves are also ideal shape and the LUB values of them were in the range of 0.4-1.3 cm. The ratio of the LUB over the monolith length ( $LUB \cdot L^{-1}$ ) decreases with increasing of the carbonization temperature. In CMHs carbonized at higher temperatures (873-1273 K),  $q_B \cdot q_{theor}^{-1}$  was close to 1 indicating almost all of the adsorption sites were used.

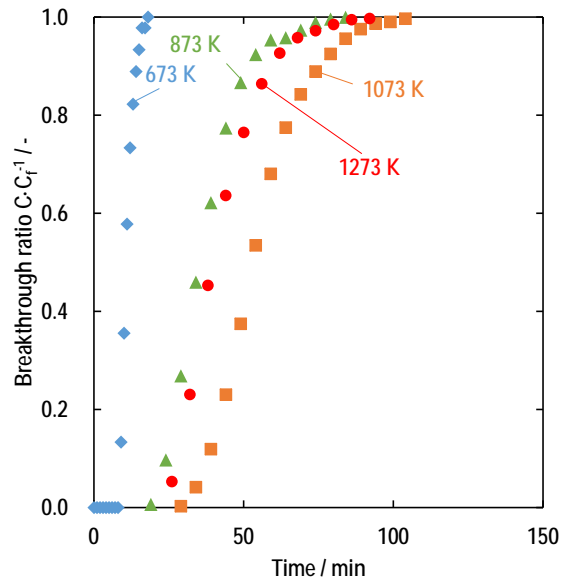


**Fig. 2.9** Phenol breakthrough curves (303 K) of CMHs carbonized at 673 K (blue diamond, run 1), 873 K (green triangle, run 2), 1073 K (orange square, run 3) and 1273 K (red circle, run 5); initial concentration (feed concentration), 100 ppm; monolith length, 1.5 cm; monolith diameter, 0.6-0.8 cm, superficial velocity,  $3.0 \text{ cm} \cdot \text{min}^{-1}$ .

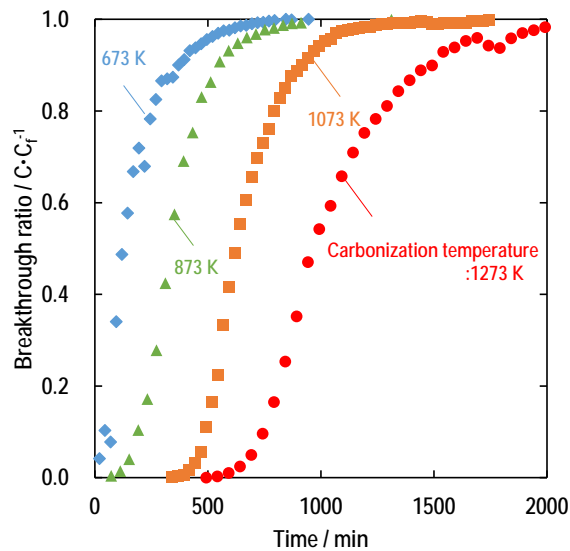


**Fig. 2.10** MB breakthrough curves (303 K) of CMHs carbonized at 673 K (blue diamond, run 1), 873 K (green triangle, run 2), 1073 K (orange square, run 3) and 1273 K (red circle, run 5); initial concentration (feed concentration), 100 ppm; monolith length, 1.5 cm; monolith diameter, 0.6-0.8 cm, superficial velocity,  $3.0 \text{ cm} \cdot \text{min}^{-1}$ .

To evaluate the scaling-up applicability of CMHs, breakthrough experiments using CMHs, with various monolith lengths were conducted (Fig.2.10, Table 2.4). Although the obtained curves shift to the right with the increase in monolith length, the shape of the curves hardly changes. In CMHs longer than 1.5 cm, the calculated LUB values were constant (0.6 cm) which indicates that the adsorption zone of the CMH has already reached an equilibrium state at a short length of 1.5 cm (constant-pattern behavior<sup>22</sup>). In addition,  $LUB \cdot L^{-1}$  decreases with the increase in monolith length. These results indicate that a high column utilization on a length basis can be achieved after scaling-up of the CMH.

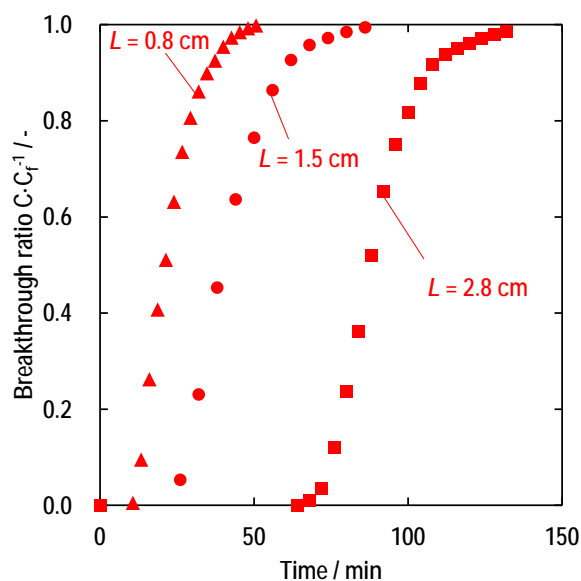


**Fig. 2.10** Phenol breakthrough curves (303 K) of CMHs carbonized at 1273 K with monolith lengths of 0.8 cm (red triangle, run 4), 1.5 cm (red circle, run 5) and 2.8 cm (red square, run 6); initial concentration (feed concentration), 100 ppm; monolith diameter, 0.7 cm, superficial velocity, 3.0  $\text{cm} \cdot \text{min}^{-1}$ .

**Table 2.4** Results from the breakthrough experiments of phenol on CMH<sup>a</sup>

Run	$T / K$	Mass / g	Length $L / cm$	Diameter / cm	$q_B^b /$ $mmol \cdot g^{-1}$	$q_{theor.}^c /$ $mmol \cdot g^{-1}$	$q_B \cdot q_{theor}^{-1}$ / -	LUB / cm	$LUB \cdot L^{-1}$ / -
1	673	0.05	1.5	0.8	0.21	0.20	1.1	0.44	0.29
2	873	0.05	1.5	0.7	1.00	1.11	0.91	0.66	0.44
3	1073	0.04	1.5	0.6	1.28	1.67	0.76	0.60	0.40
4	1273	0.02	0.8	0.7	1.40	1.62	0.87	0.34	0.43
5	1273	0.03	1.5	0.7	1.36	1.62	0.84	0.56	0.37
6	1273	0.07	2.8	0.7	1.29	1.62	0.80	0.61	0.22

<sup>a</sup>All experiments were conducted at 303 K at superficial velocity of  $3.0 \text{ cm} \cdot \text{min}^{-1}$ , <sup>b</sup> Phenol uptake calculated from breakthrough curve, <sup>c</sup> Theoretical phenol uptake calculated from the Langmuir model at equilibrium concentration of 100 ppm

**Table 2.5** Results from the breakthrough experiments of methylene blue on CMH<sup>a</sup>

Run	$T / K$	Mass / g	Length $L / cm$	Diameter / cm	$q_B^b /$ $mmol \cdot g^{-1}$	$q_{theor.}^c /$ $mmol \cdot g^{-1}$	$q_B \cdot q_{theor}^{-1}$ / -	LUB / cm	$LUB \cdot L^{-1}$ / -
7	673	0.05	1.5	0.8	0.15	0.002	75	1.31	0.87
8	873	0.03	1.5	0.7	0.43	0.31	1.4	0.82	0.53
9	1073	0.03	1.5	0.7	0.65	0.53	1.2	0.43	0.27
10	1273	0.05	1.9	0.6	0.57	0.49	1.2	0.63	0.32

<sup>a</sup>All experiments were conducted at 303 K at superficial velocity of  $3.0 \text{ cm} \cdot \text{min}^{-1}$ , <sup>b</sup> Methylene blue uptake calculated from breakthrough curve, <sup>c</sup> Theoretical methylene blue uptake calculated from the Langmuir model at equilibrium concentration of 10 ppm

To evaluate recyclability of the CMHs, regeneration was conducted by ethanol flows after phenol breakthrough experiments. The obtained curves for each cycle is shown in Figure 2.11. The curves were shifted toward left direction, indicating that the capacity decreases by ethanol regeneration. Finally, the capacity reaches about 60 % of the initial capacity ( $0.78 \text{ mmol} \cdot \text{g}^{-1}$ ). This decreases also indicates that the irreversible adsorption occurs. The capacity stabilized after the 7<sup>th</sup> cycle, indicating that irreversible adsorption sites were saturated (7.12).

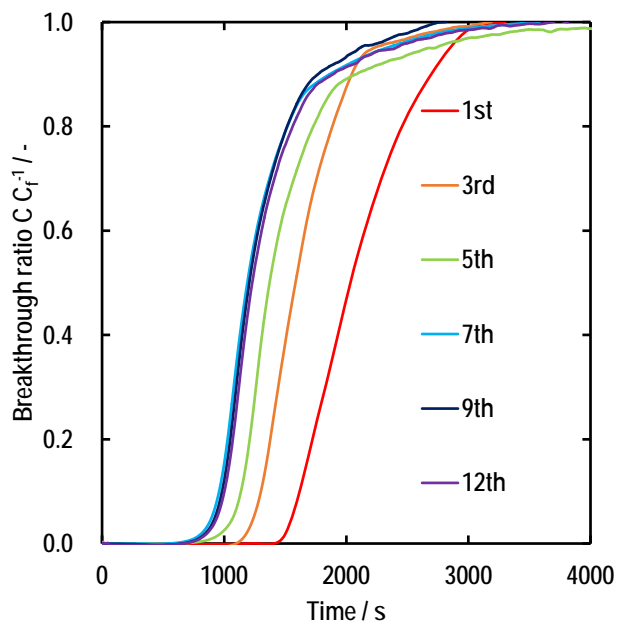


**Fig. 2.11** Phenol breakthrough curves of CMH carbonized at 1273 K after regeneration. For breakthrough experiments: monolith lengths, 1.5 cm; initial concentration (feed concentration), 100 ppm; monolith diameter, 0.7 cm, superficial velocity,  $3.0 \text{ cm}\cdot\text{min}^{-1}$ . Regeneration conditions: effluent, ethanol; superficial velocity,  $3.0 \text{ cm}\cdot\text{min}^{-1}$ .

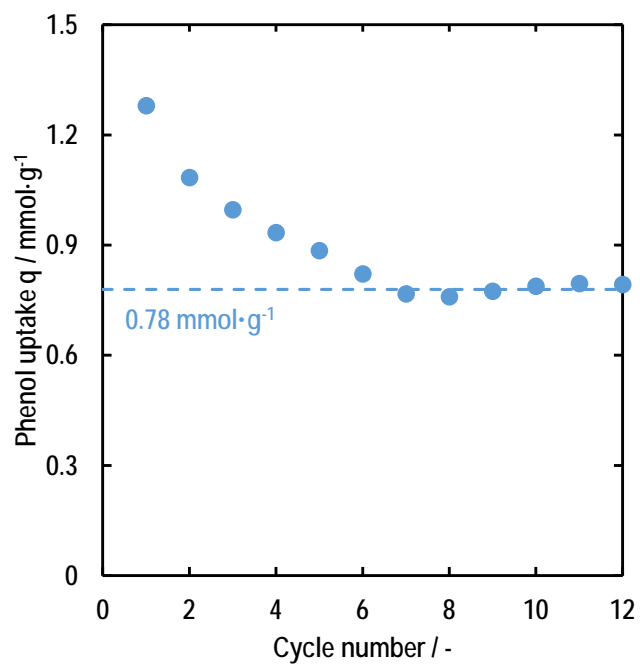


**Fig. 2.12** Phenol capacity of CMH carbonized at 1273 K calculated from each cycle

## 2.4 Conclusion

In this chapter we synthesized and characterized various CMHs and tested their phenol and methylene blue adsorption abilities not only in batch systems but also in continuous flow systems. The CMH showed a 370 times-lower hydraulic resistance when compared with a typical column packed with particles having the same diffusion length as in the microhoneycomb walls. The CMHs had developed meso-micro pores and their BET surface area and hydrophobicity increases with the increase in carbonization temperature. Phenol and methylene blue uptake also increases with the increase in carbonization temperature and irreversible adsorption also occurs in CMHs carbonized at higher temperatures. Phenol and methylene blue adsorption isotherms indicated that adsorption is not only affected by the surface area of the CMHs but also by their surface hydrophilicity/hydrophobicity which is governed by the concentration of surface oxygen groups in them. The adsorption experiments in flow systems showed that physisorption solely occurs because of the short residence time. For phenol, the LUB values were in the range of 0.3-0.6 cm and became constant at lengths as short as 1.5 cm. These results show that a constant-pattern behavior is quickly achieved so high column utilization can be expected in scaled-up CMHs. For methylene blue, the LUB values were in the range of 0.4-1.3 cm. The phenol capacity decreased by ethanol regeneration and the capacity stabilized at the 7<sup>th</sup> cycle. These results clearly indicate that CMHs have a high potential to be used for phenol and methylene blue adsorption in continuous flow systems.

## 2.5 Reference

1. Government of Japan, Ministry of the Environment, National Effluent Standards. <http://www.env.go.jp/en/water/wq/nes.html>.
2. Dąbrowski, A.; Podkościelny, P.; Hubicki, Z.; Barczak, M., Adsorption of Phenolic Compounds by Activated Carbon-A Critical Review. *Chemosphere* **2005**, *58* (8), 1049-1070.
3. Srivastava, V. C.; Swamy, M. M.; Mall, I. D.; Prasad, B.; Mishra, I. M., Adsorptive Removal of Phenol by Bagasse Fly Ash and Activated Carbon: Equilibrium, Kinetics and Thermodynamics. *Colloid. Surface. A* **2006**, *272* (1-2), 89-104.
4. Juang, R.-s.; Tseng, R.-L.; Wu, F.-C., Role of Microporosity of Activated Carbons on Their Adsorption Abilities for Phenols and Dyes. *Adsorption* **2001**, *7* (1), 65-72.
5. Kujawski, W.; Warszawski, A.; Ratajczak, W.; Porębski, T.; Capała, W.; Ostrowska, I., Removal of Phenol from Wastewater by Different Separation Techniques. *Desalination* **2004**, *163* (1-3), 287-296.
6. Jiang, H. L.; Tay, J. H.; Tay, S. T. L., Aggregation of Immobilized Activated Sludge Cells into Aerobically Grown Microbial Granules for the Aerobic Biodegradation of Phenol. *Lett. Appl. Microbiol.* **2002**, *35* (5), 439-445.
7. Esplugas, S.; Giménez, J.; Contreras, S.; Pascual, E.; Rodríguez, M., Comparison of Different Advanced Oxidation Processes for Phenol Degradation. *Water Res.* **2002**, *36* (4), 1034-1042.
8. Pekala, R. W., Low density, Resorcinol-Formaldehyde Aerogels. US Patent 4873218: 1989.
9. Pekala, R. W., Organic Aerogels from the Polycondensation of Resorcinol with Formaldehyde. *J. Mater. Sci.* **1989**, *24* (9), 3221-3227.
10. Kaschmitter, J. L.; Mayer, S. T.; Pekala, R. W., Process for Producing Carbon foams for Energy Storage Devices. US Patent 5789338: 1998.
11. Mirzaeian, M.; Hall, P. J., Preparation of Controlled Porosity Carbon Aerogels for Energy Storage in Rechargeable Lithium Oxygen Batteries. *Electrochim. Acta* **2009**, *54* (28), 7444-7451.
12. Moreno-Castilla, C.; Maldonado-Hódar, F. J., Carbon Aerogels for Catalysis Applications: An Overview. *Carbon* **2005**, *43* (3), 455-465.
13. Kim, S. I.; Yamamoto, T.; Endo, A.; Ohmori, T.; Nakaiwa, M., Adsorption of Phenol and Reactive Dyes from Aqueous Solution on Carbon Cryogel Microspheres with Controlled Porous Structure. *Micropor. Mesopor. Mater.* **2006**, *96* (1-3), 191-196.
14. Nishihara, H.; Mukai, S. R.; Tamon, H., Preparation of Resorcinol-Formaldehyde Carbon Cryogel Microhoneycombs. *Carbon* **2004**, *42* (4), 899-901.
15. Yamamoto, T.; Nishimura, T.; Suzuki, T.; Tamon, H., Control of Mesoporosity of Carbon Gels Prepared by Sol-Gel Polycondensation and Freeze Drying. *J. Non-Cryst. Solids* **2001**, *288* (1-3), 46-55.
16. Ogino, I.; Sakai, K.; Mukai, S. R., Marked Increase in Hydrophobicity of Monolithic Carbon Cryogels via HCl Aging of Precursor Resorcinol-Formaldehyde Hydrogels: Application to 1-butanol

- Recovery from Dilute Aqueous Solutions. *J. Phys. Chem. C* **2014**, *118* (13), 6866-6872.
17. Grant, T.; King, C., Mechanism of Irreversible Adsorption of Phenolic Compounds by Activated Carbons. *Ind. Eng. Chem. Res.* **1990**, *29*, 264-271.
18. Magne, P.; Walker, P. L., Phenol Adsorption on Activated Carbons: Application to the Regeneration of Activated Carbons Polluted with Phenol. *Carbon* **1986**, *24* (2), 101-107.
19. Thommes, M.; Mitchell, S.; Pérez-Ramírez, J., Surface and Pore Structure Assessment of Hierarchical MFI Zeolites by Advanced Water and Argon Sorption Studies. *J. Phys. Chem. C* **2012**, *116* (35), 18816-18823.
20. Ogino, I.; Kazuki, S.; Mukai, S. R., Marked Increase in Hydrophobicity of Monolithic Carbon Cryogels via HCl Aging of Precursor Resorcinol-formaldehyde Hydrogels: Application to 1-butanol Recovery from Dilute Aqueous Solutions. *J. Phys. Chem. C* **2014**, *118* (13), 6866-6872.
21. Lin, S. H.; Juang, R. S., Adsorption of Phenol and Its Derivatives from Water Using Synthetic Resins and Low-Cost Natural Adsorbents: A review. *J. Environ. Manage.* **2009**, *90* (3), 1336-1349.
22. Ruthven, D. M., *Principles of Adsorption and Adsorption Processes*. Wiley: New York, 1984.

## *Part 2*

# *Separation of Cesium Ion in Flow Systems Using Monolithic Ion- Exchangers with a Microhoneycomb structure*



# ***Chapter 3***

## ***Separation of Cesium Ion in Flow Systems Using Prussian Blue Analogues Nanoparticles Supported in a Silica-Alumina Microhoneycomb***

### **3.1. Introduction**

The nuclear disaster at the Fukushima Daiichi nuclear power plant in Japan has generated a huge amount of radionuclides, which have spread from the plant into the ocean and nearby grounds. Among these radionuclides, the quick and effective recovery of cesium-137 ( $^{137}\text{Cs}$ ) has been required especially because it has high radioactivity and a long half-life (30.1 years<sup>1</sup>), potentially causing harmful effects to human health and environment. Total amounts of  $^{137}\text{Cs}$  which spread into nearby grounds and released to the Pacific Ocean were estimated as 6.7 PBq and 1.3 PBq, respectively.<sup>2</sup> The  $^{137}\text{Cs}$  which spread into the ground is strongly adsorbed in the layer silicates in the soil of the ground, therefore, aqueous acidic solutions can be used to extract the  $^{137}\text{Cs}$  from the soil.<sup>3, 4</sup> However, this will lead to the generation of acidic solutions containing low concentrations of  $^{137}\text{Cs}$ .

To effectively separate  $^{137}\text{Cs}$ , the possibility of using various separation methods have been investigated. Examples include ion exchange<sup>5-22</sup> and extraction.<sup>23</sup> Ion exchange is one of the most effective methods because it can be readily applied to flow systems and can also be easily scaled up. Various ion exchangers have been tested, for example, transition metal ferrocyanides,<sup>15-18</sup> heteropoly compounds with Keggin structure,<sup>5-14</sup> various kinds of zeolites,<sup>19, 20</sup> silicotitanates<sup>21</sup> and polymers.<sup>22</sup>

Among these ion exchangers, Prussian blue analogues (PBAs) as the medium for recovery, as they are inexpensive and as they show a high selectivity towards cesium. PBAs which have abilities to recover cesium can be obtained by insolubilizing ferrocyanide using bivalent metal cations. However, the PBAs obtained through this method are usually in the form of fine particles,<sup>24</sup> so a severe pressure drop is likely to occur when fluids are passed through them.

Therefore, in this chapter, we dispersed such PBAs insolubilized by various bivalent cations ( $\text{Fe}^{2+}$ ,  $\text{Ni}^{2+}$ ,  $\text{Cu}^{2+}$  and  $\text{Zn}^{2+}$ ) within a matrix material and molded the composite to microhoneycomb structure have a morphology which only causes a minimal hydraulic resistance while still maintaining a high accessibility to the included PBAs. The obtained monolithic materials (PBAs-SAMHs) were characterized by a scanning electron microscope (SEM) and a transmission electron microscope (TEM) observation, elemental analysis,  $\text{N}_2$  adsorption/desorption experiments. The hydraulic resistance was evaluated by pressure drop measurements. The  $\text{Cs}^+$  separation performance were evaluated in batch and flow systems.

## 3.2. Materials and Methods

### 3.2.1. Materials

Sodium silicate solution ( $\text{Na}_2\text{SiO}_3$ , 55 wt%, molar ratio ( $\text{SiO}_2/\text{Na}_2\text{O}$ ) = 2.1), aluminum nitrate ( $\text{Al}(\text{NO}_3)_3$ ), iron (II) sulphate ( $\text{FeSO}_4$ ), nickel (II) nitrate ( $\text{Ni}(\text{NO}_3)_2$ ), copper (II) chloride ( $\text{CuCl}_2$ ), zinc (II) nitrate ( $\text{Zn}(\text{NO}_3)_2$ ), 2-methyl-2-propanol (*tert*-butyl alcohol, TBA), cesium chloride ( $\text{CsCl}$ ), nitric acid ( $\text{HNO}_3$ , 1 mol  $\text{L}^{-1}$  aqueous solution) and cesium standard solution ( $\text{CsCl}$ , 1000 ppm) were purchased from Wako Pure Chemical Industries. All reagents were used as received.

### 3.2.2. Preparation of the PBAs-SAMHs

In this work, silica alumina was used as the matrix of the PBA composites.<sup>25</sup> First, a silica sol, the silica source of the matrix, was prepared by diluting a sodium silicate solution with distilled and deionized water, and subsequently exchanging the sodium cations in it with protons using a strong acid ion-exchange resin. To this sol, aluminium nitrate, the alumina source of the matrix, was added so that the Si/Al molar ratio in the resulting mixture would be 5. Next, potassium ferrocyanide, the ferrocyanide source of the PBA, was added so that the  $\text{Fe}^*/\text{Si}$  molar ratio in the resulting mixture would be either 0.040, 0.050 or 0.067 ( $\text{Fe}^*$  denotes that the origin of it is ferrocyanide). Then, a compound which can release a bivalent cation was added to insolubilize the dispersed ferrocyanide. The bivalent cations used in this work were  $\text{Fe}^{2+}$ ,  $\text{Ni}^{2+}$ ,  $\text{Cu}^{2+}$  and  $\text{Zn}^{2+}$ , and the compounds used as

their sources were iron(II) sulphate, nickel(II) nitrate, copper(II) chloride and zinc(II) nitrate, respectively. Then the mixtures were transferred to polypropylene tubes and were aged at 333 K. After the mixtures transformed into gels, the tubes including them were dipped into a liquid nitrogen bath at a constant rate of 60 mm·h<sup>-1</sup>, and the gels were froze unidirectionally. After the gels were completely frozen, they were thawed and then thoroughly washed with distilled and deionized water. Next the water in the gels was exchanged with 2-methyl-2-propanol and then the gels were freeze-dried. Finally, cylindrical monoliths were obtained.

### 3.2.3. Characterization of the PBAs-SAMHs

The morphology of the samples was directly observed using a scanning electron microscope (SEM). Elemental analyses of the samples were conducted using an inductively coupled plasma spectrometer and a CHN coder. The samples were also analysed using an X-ray diffractometer (XRD) to confirm the existence of PBAs. The porous properties of the samples were evaluated through nitrogen adsorption experiments. First, nitrogen adsorption isotherms of the samples were measured at 77 K. Next, the Brunauer-Emmett-Teller surface areas ( $S_{\text{BET}}$ ) of the samples were calculated from the obtained isotherms.

### 3.2.4. Cs<sup>+</sup> Separation Experiments Using the PBAs-SAMHs in Batch Systems

The cesium capacity of the samples was evaluated by measuring their cesium ion exchange isotherms. Experiments were conducted at 298 K using 1 mmol·L<sup>-1</sup> nitric acid containing cesium carbonate. Solutions containing the samples were shaken for 7 days before determining the cesium uptake. Cesium uptake ( $q$ ) was calculated using the following equation (eq. 3.1)

$$q = (C_0 - C_e) \frac{V}{m} \quad (3.1)$$

where  $C_0$  and  $C_e$  are respectively the initial and equilibrium concentration,  $V$  the volume of the solution and  $m$  the weight of the sample.

### 3.2.5. Cs<sup>+</sup> Separation Experiments Using PBAs-SAMHs in Flow Systems

Next, the performance of the samples in flow systems was evaluated. The hydraulic resistance the samples cause was evaluated by measuring the pressure drop which occurs when water was passed through them. The diameter and length of the samples used in this experiment were 10 mm and 10 mm, respectively. Finally, the performance of the samples as cesium adsorbents was checked in a flow system. First, 1 mmol·L<sup>-1</sup> nitric acid containing cesium carbonate was prepared so that the Cs<sup>+</sup> concentration in it would be 100 ppm ( $C_f$ ). The prepared solution was passed through the samples at a flow rate of 1 mL·min<sup>-1</sup>, and the Cs<sup>+</sup> concentration at the outlet of the samples ( $C$ ) was monitored periodically using ion chromatography. The ratio of  $C$  to  $C_f$  ( $C \cdot C_f^{-1}$ ) was plotted against the effluent volume. The diameter and length of the samples used in this experiment were 10 mm and 20 mm, respectively. Figure 4.1 shows the experimental apparatus used for the measurement of pressure drop and evaluation of separation performance in flow systems.

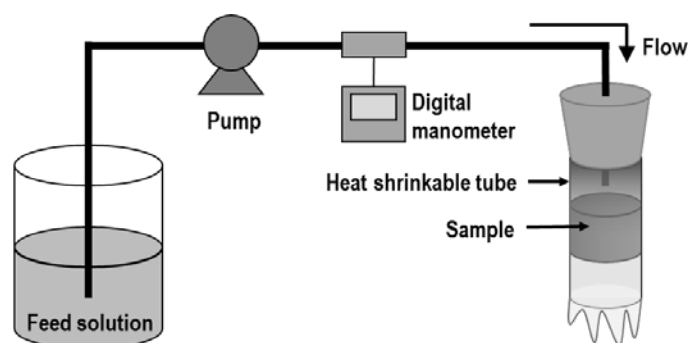


**Fig. 3.1** Experimental apparatus for flow systems

## 3.3. Results and Discussion

### 3.3.1. Characterization of the PBAs-SAMHs

Figure 3.2 shows photographs and cross sectional SEM images of typical samples obtained in this work. Basically, cylindrical samples show a characteristic color depending on the cation used for the insolubilization of ferrocyanide. Although the channels were slightly distorted, it was confirmed that the samples basically have a microhoneycomb structure, the average size of the channels being a few tens of micrometers. However, samples synthesized at high Fe\*/Si ratios tended to lack strength, and

some of them collapsed even during analysis. Therefore, following studies were conducted using samples synthesized at a Fe\*/Si ratio of 0.050.

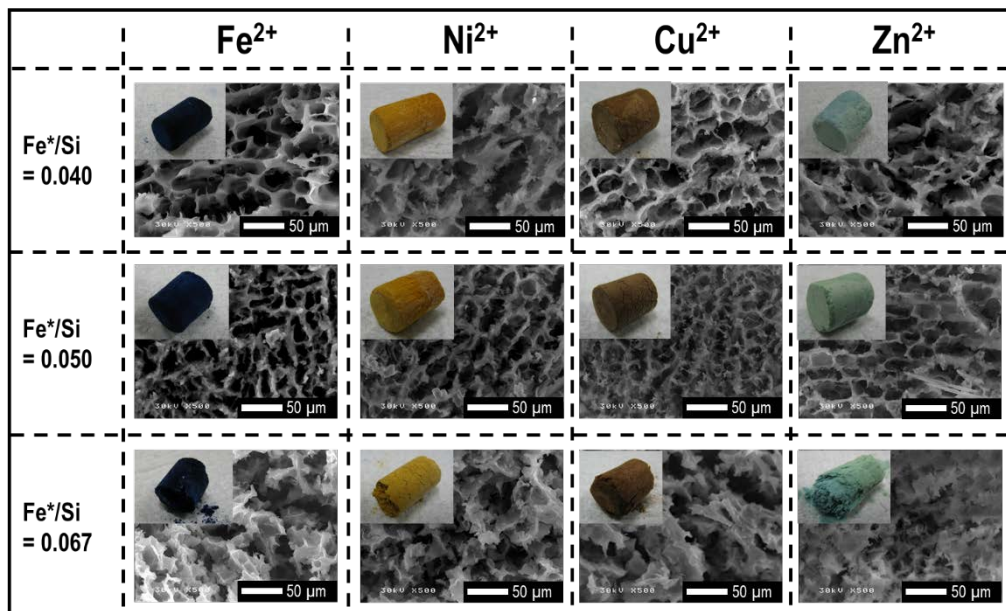


**Fig. 3.2** Photographs and cross sectional SEM images of typical samples obtained in this work

Next, the compositions of the PBAs included within the samples were verified through elemental analysis. Table 3.1 summarizes the results. If the desired PBAs were formed within the monolithic samples, the  $Fe^*/M$  and the  $\{(Fe^*+M)/2\}/(N/6)$  molar ratios should both be unity, where  $M$  ( $= Fe^{2+}$ ,  $Ni^{2+}$ ,  $Cu^{2+}$  and  $Zn^{2+}$ ) denotes the amount of the cation used for insolubilization and  $N$  is amount of nitrogen atom in the sample. It was confirmed that values close to unity were achieved in all samples, indicating the high possibility of the formation of ideal PBAs in all of the samples.

**Table 3.1** Elemental analysis results of the obtained samples

Atomic ratio	Ideal Ratio	$M = Fe^{2+}$	$Ni^{2+}$	$Cu^{2+}$	$Zn^{2+}$
$Fe^*/M$	1	1 <sup>a</sup>	0.93	0.97	1.02
$\{(Fe^*+M)/2\}/(N/6)$	1	0.89	0.90	0.97	0.93

$M$ : Amount of the cation used for insolubilization,  $Fe^*$ : Amount of Fe in the origin of it is ferrocyanide

<sup>a</sup> Assumed value as Fe from iron sulphate cannot be distinguished from that from ferrocyanide

The structure of the particles included in the samples was checked using an XRD. Figure 3.3 shows XRD patterns of typical samples in which the ferrocyanide included in them was insolubilized using different cations. In the samples synthesized using  $\text{Fe}^{2+}$ ,  $\text{Ni}^{2+}$  and  $\text{Cu}^{2+}$  for insolubilization, characteristic patterns of the corresponding PBAs were obtained, indicating the existence of the desired PBAs in them. However, this was not the case in samples synthesized using  $\text{Zn}^{2+}$  for insolubilization, which implies that either the desired PBA was not formed, or the formed PBA particles were too small to be detected. We will show later that the later seems to be the reason why  $\text{Zn}^{2+}$  based PBAs were not detected.

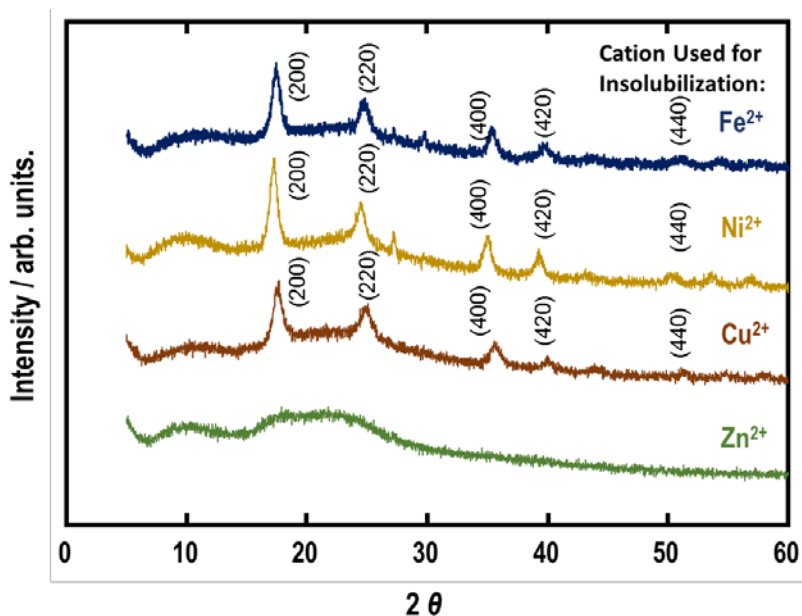


**Fig. 3.3** XRD patterns of typical samples obtained in this work

Next, the porous properties of the samples were evaluated through nitrogen adsorption experiments. A representative result is shown in Figure 3.4 where the nitrogen adsorption-desorption isotherm of a typical sample and  $S_{\text{BET}}$  derived from the isotherm is shown.  $\text{Fe}^{2+}$  was used to insolubilize the ferrocyanide in this sample. Those of a silica-alumina microhoneycomb synthesized without PBA inclusion, and of PBA particles alone is also shown for comparison. The PBA particles appeared to have a small amount of mesopores, which is thought to actually be the pores naturally formed between

the particles. On the other hand, monolithic silica-alumina microhoneycombs obtained through the Ice Templating method have developed micropores and mesopores. When PBAs were included into such microhoneycombs, a decrease in mesopore volume was observed, but the sample still showed high porosities, indicating that the accessibility to the surface of the PBA particles dispersed and immobilized in the microhoneycombs is high.

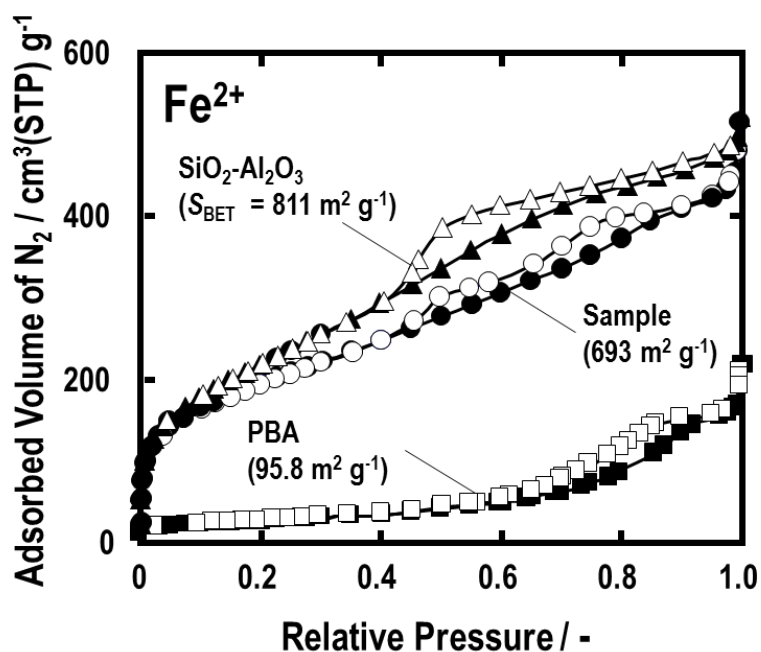


**Fig 3.4** Nitrogen adsorption-desorption isotherms (77 K) of a typical sample insolubilized by Fe<sup>2+</sup>

Figure 3.5 shows TEM images of samples. PBA particles 10-15 nm in diameter can be observed in the TEM images of samples synthesized using Fe<sup>2+</sup>, Ni<sup>2+</sup> and Cu<sup>2+</sup> for insolubilization. On the other hand, particles cannot be observed in the TEM image of sample synthesized using Zn<sup>2+</sup> for insolubilization.

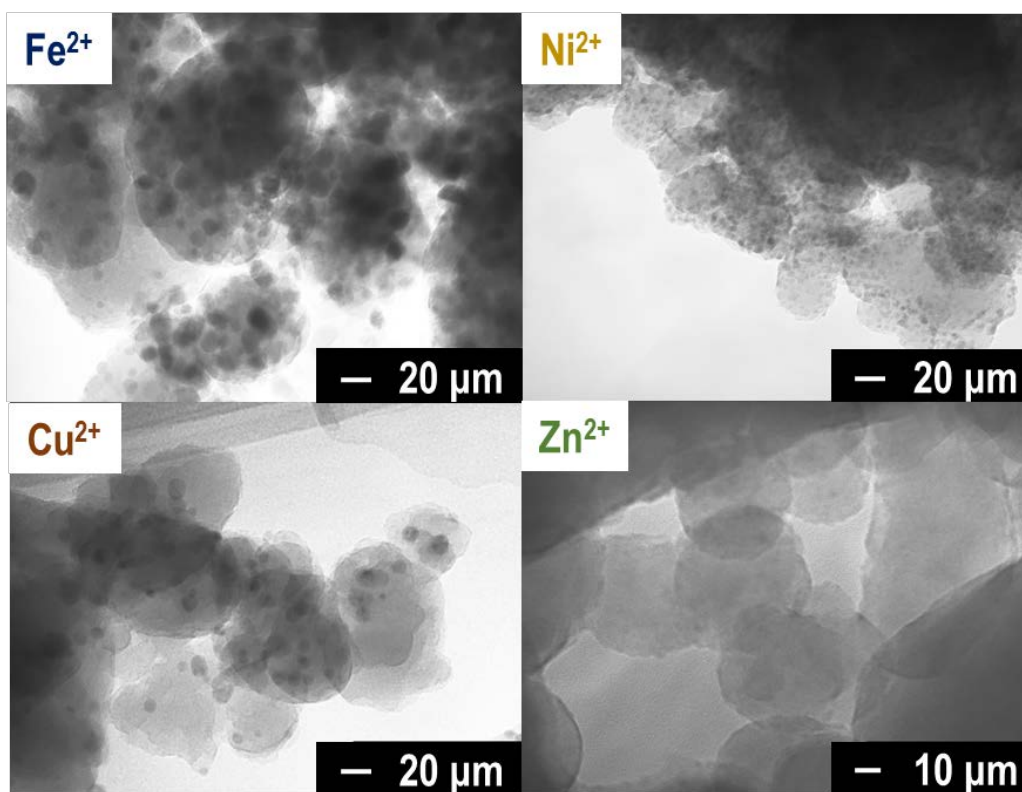


**Fig. 3.5** TEM image of PBA-SAMHs insolubilized by  $\text{Fe}^{2+}$  (upper left),  $\text{Ni}^{2+}$  (upper right),  $\text{Zn}^{2+}$  (bottom left) and  $\text{Cu}^{2+}$  (bottom right).

Next we checked how the samples perform when they are used to recover cesium in flow systems. First, the hydraulic resistance the samples cause when water was passed through them was measured. A typical result is shown in Figure 3.6, where the measured pressure drop is plotted as a function of superficial velocity. It was confirmed that, as expected, the hydraulic resistance of the samples is quite low. Analytical pressure drop occurs when water passes through tube  $11\ \mu\text{m}$  in diameter is also shown in the same Figure. This pressure drop value, which was calculated using the Hagen-Poiseuille equation, can well represent measured values. This result indicates that PBA-SAM can be regarded as a bundle of capillary tubes whose representative diameter is the same as the macro channel size of the samples. This result also indicates that synthesis of PBAs does not affect to formation of the honeycomb structure. The dotted line in the same figure shows the predicted values of the pressure drop which occurs in a column which has the same inner diameter as the samples, and which is packed

with the same amount of the same material as the samples in the form of particles. The values were predicted using the Kozeny-Carman equation<sup>26, 27</sup> assuming that the radius of the particles was 1.5  $\mu\text{m}$ , same as the average diffusion path length in the microhoneycomb sample, and the void fraction of the column was 0.45, a value typical for a column packed with particles. The resistance particles having the same diffusion path lengths as the samples caused was 50-fold higher than the samples. Therefore, it was confirmed that a low hydraulic resistance and short diffusion paths are compatible in the samples synthesized in this work.

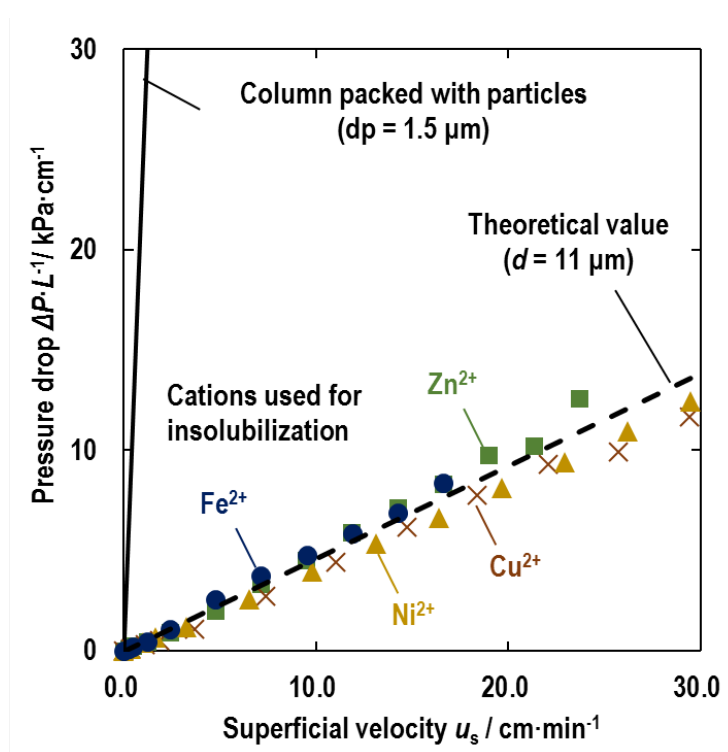


**Fig. 3.6** Pressure drop data of water flowing through PBA-SAMH insolubilized by  $\text{Fe}^{2+}$  (blue circle),  $\text{Ni}^{2+}$  (yellow triangle),  $\text{Zn}^{2+}$  (green square) and  $\text{Cu}^{2+}$  (brown cross). The dotted line represents the pressure drop calculated using the Hagen-Poiseuille equation. The solid line represents the pressure drop for a column packed with particles calculated using Kozeny-Carman equation.

### 3.3.2. $\text{Cs}^+$ Separation Using PBAs-SAMHs in Batch Systems

Figure 3.7 shows the cesium ion exchange isotherms of samples, in which different cations were used to insolubilize the ferrocyanide included in them. It was confirmed that all of the samples possess

a fairly high cesium capacity, even at low concentrations. Although the reason remains unclear at this moment, the samples synthesized using  $\text{Cu}^{2+}$  showed the highest capacity, followed by samples synthesized using  $\text{Zn}^{2+}$ ,  $\text{Ni}^{2+}$  and  $\text{Fe}^{2+}$  as the metal cation for insolubilization. The theoretical ion exchange capacities of these samples, which were calculated using  $\text{K}^+$  as the exchangeable ion, ranges from 0.843 to 0.846  $\text{mmol}\cdot\text{g}^{-1}$ . The measured maximum capacity of the sample using  $\text{Cu}^{2+}$  for insolubilization was half of the theoretical value. The measured capacity was higher than the reported capacity of a similar sample synthesized using  $\text{Cu}^{2+}$  for insolubilization and polyethylenimine/silica as the matrix ( $0.15 \text{ mmol}\cdot\text{g}^{-1}$ ),<sup>28</sup> but lower than that synthesized by using surface modification onto mesoporous silica ( $1.14 \text{ mmol}\cdot\text{g}^{-1}$ ).<sup>29</sup> As  $\text{Zn}^{2+}$ -based materials also showed a high capacity, it seems safe to conclude that PBAs were also formed when  $\text{Zn}^{2+}$  was used for insolubilization.

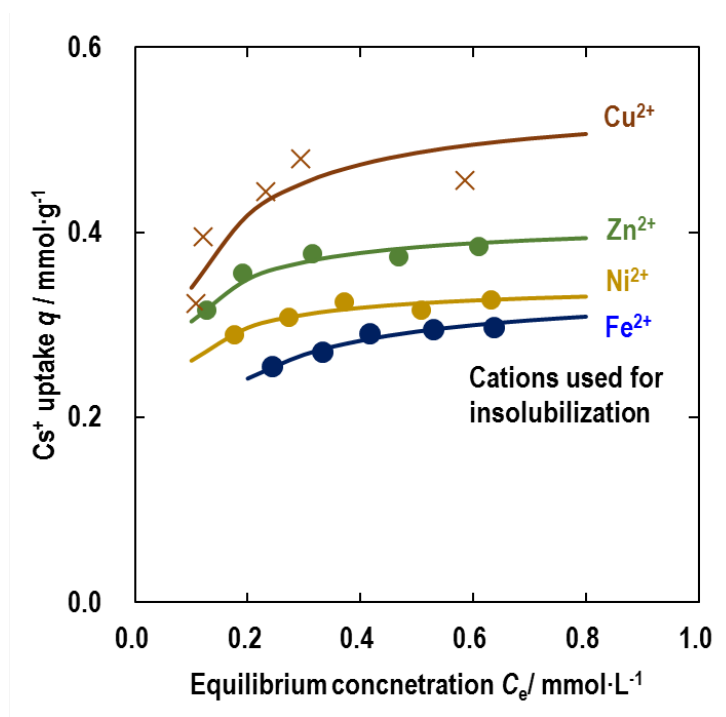


**Fig. 3.7**  $\text{Cs}^+$  ion exchange isotherms (298 K) of PBA-SAMHs insolubilized by  $\text{Fe}^{2+}$  (blue circle),  $\text{Ni}^{2+}$  (yellow triangle),  $\text{Zn}^{2+}$  (green square) and  $\text{Cu}^{2+}$  (brown cross). The solid lines represent fits to the Langmuir isotherm equation.  $\text{Cs}^+$  solution contains  $1 \text{ mmol}\cdot\text{L}^{-1} \text{ HNO}_3$ .

### 3.3.3. $\text{Cs}^+$ Separation Using PBAs-SAMHs in Flow Systems

Finally, the performance of the samples as cesium adsorbents for flow systems was verified. Figure

3.8 shows typical breakthrough curves of typical samples obtained in this work. Although the sample was short, 10 mm in length, a period of complete cesium removal was observed excluding Fe<sup>2+</sup> based sample. Then the outlet cesium concentration started to gradually increase following a typical sigmoidal curve. From the results of this experiments, the length of the mass transfer zone of the cylindrical sample could be estimated to be about 10 mm. Due to the unique microhoneycomb morphology of the samples, this length can be maintained even when the diameter of the cylindrical sample is significantly increased, as long as the size of the channels and the superficial velocity of the fluid is the same. Therefore, such microhoneycombs are expected to be used as adsorbents for efficient cesium recovery in flow systems which require a high throughput.

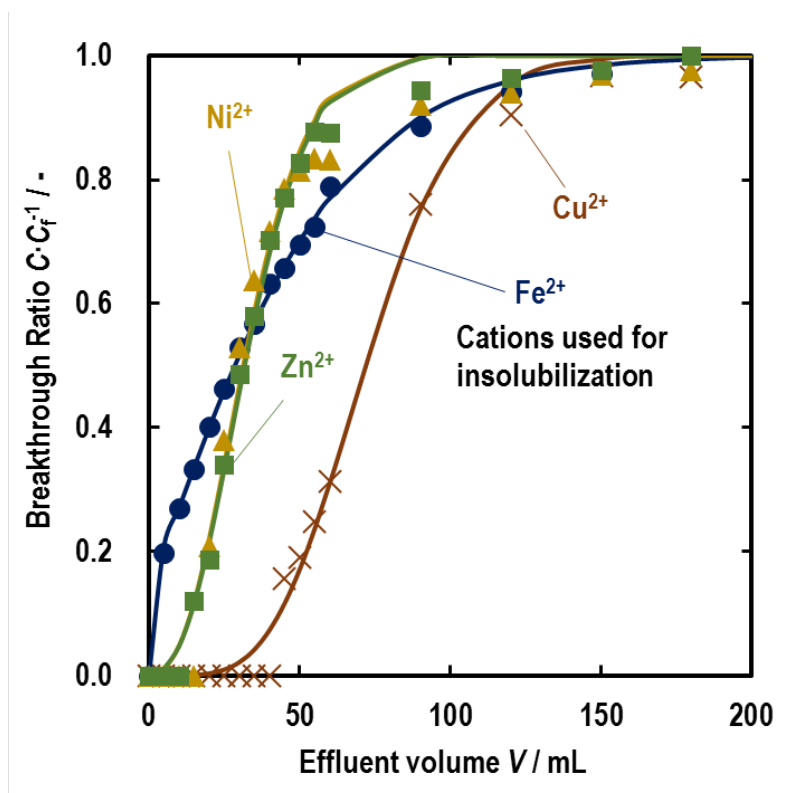


**Fig. 3.8** Breakthrough curves of PBA-SAMHs insolubilized by Fe<sup>2+</sup> (blue circle), Ni<sup>2+</sup> (yellow triangle), Zn<sup>2+</sup> (green square) and Cu<sup>2+</sup> (brown cross). Conditions: superficial velocity  $u_s = 20 \text{ mm} \cdot \text{min}^{-1}$ , feed Cs<sup>+</sup> concentration  $C_f = 100 \text{ ppm}$  (containing  $1 \text{ mmol} \cdot \text{L}^{-1} \text{ HNO}_3$ ), monolith length  $L = 10 \text{ mm}$ .

### 3.4. Conclusion

In this work, cesium adsorbents were synthesized by immobilizing various PBAs in silica-alumina microhoneycombs using the Ice Templating method. Due to their unique morphology, the microhoneycombs were found to efficiently recover cesium from aqueous solutions without causing a severe hydraulic resistance. It was found that the hydraulic resistance the adsorbent causes can be reduced over 90 % by adopting a microhoneycomb morphology instead of a particle morphology. Therefore, the usage of such materials also leads to a significant decrease in the energy and operation costs required to use them. Such microhoneycomb materials have high potentials to be used not only as novel adsorbents, but also as catalysts or catalyst supporting materials for flow systems, especially when a high throughput is required.

### 3.5. References

1. Audi, G.; Bersillon, O.; Blachot, J.; Wapstra, A. H., The NUBASE Evaluation of Nuclear and Decay Properties. *Nucl. Phys. A* **2003**, 729 (1), 3-128.
2. Yasunari, T. J.; Stohl, A.; Hayano, R. S.; Burkhart, J. F.; Eckhardt, S.; Yasunari, T., Cesium-137 Deposition and Contamination of Japanese Soils due to the Fukushima Nuclear Accident. *Proc. Natl. Acad. Sci. U. S. A.* **2011**, 108 (49), 19530-19534.
3. Parajuli, D.; Takahashi, A.; Tanaka, H.; Sato, M.; Fukuda, S.; Kamimura, R.; Kawamoto, T., Variation in Available Cesium Concentration with Parameters during Temperature Induced Extraction of Cesium from Soil. *J. Environ. Radioact.* **2015**, 140, 78-83.
4. Yasutaka, T.; Kawamoto, T.; Komai, T., Applicability of the Acid Extraction Method to Radioactive Caesium Contaminated Soil. *Radioisotopes* **2013**, 62 (4), 211-218.
5. Smit, J. V. R., Ammonium Salts of the Heteropolyacids as Cation Exchangers. *Nature* **1958**, 181 (4622), 1530-1531.
6. Endo, Y.; Wu, Y.; Mimura, H.; Niibori, Y.; Ozawa, M., Selective Uptake of Cesium Ions on AMP-loaded Silica Gels. *J. Ion Exch.* **2007**, 18.
7. Mimura, H.; Saito, M.; Akiba, K.; Onodera, Y., Selective Uptake of Cesium by Ammonium Molybdophosphate (AMP)-Calcium Alginate Composites. *J. Nucl. Sci. Technol.* **2001**, 38 (10), 872-878.
8. Tranter, T. J.; Herbst, R. S.; Todd, T. A.; Olson, A. L.; Eldredge, H. B., Evaluation of Ammonium Molybdophosphate-Polyacrylonitrile (AMP-PAN) as a Cesium Selective Sorbent for the Removal of

- <sup>137</sup>Cs from Acidic Nuclear Waste Solutions. *Adv. Environ. Res.* **2002**, *6* (2), 107-121.
9. Rao, K. L. N.; Shukla, J. P.; Venkataramani, B., Electron Irradiation Studies on Ammonium Molybdophosphate. *J. Radioanal. Nucl. Chem.* **1995**, *189* (1), 107-114.
10. Doležal, J.; Stejskal, J.; Tympl, M.; Kouřim, V., Improved Inorganic Ion-Exchangers. *J. Radioanal. Nucl. Chem.* **1974**, *21* (2), 381-387.
11. Satyanarayana, J.; Murthy, G. S.; Sasidhar, P., Adsorption Studies of Cesium on a New Inorganic Exchanger Ammonium Molybdophosphate-Alumina (AMP-Al<sub>2</sub>O<sub>3</sub>). *J. Radioanal. Nucl. Chem.* **1999**, *242* (1), 11-16.
12. Park, Y.; Lee, Y.-C.; Shin, W. S.; Choi, S.-J., Removal of Cobalt, Strontium and Cesium from Radioactive Laundry Wastewater by Ammonium Molybdophosphate-Polyacrylonitrile (AMP-PAN). *Chem. Eng. J.* **2010**, *162* (2), 685-695.
13. Todd, T. A.; Mann, N. R.; Tranter, T. J.; Šebesta, F.; John, J.; Motl, A., Cesium Sorption from Concentrated Acidic Tank Wastes Using Ammonium Molybdophosphate-Polyacrylonitrile Composite sorbents. *J. Radioanal. Nucl. Chem.* **2002**, *254* (1), 47-52.
14. Yoshida, S.; Kimura, Y.; Ogino, I.; Mukai, S. R., Synthesis of a Microhoneycomb-Type Silica-Supported Ammonium Molybdophosphate for Cesium Separation. *J. Che. Eng. Jpn* **2013**, *46* (9), 616-619.
15. Prout, W. E.; Russell, E. R.; Groh, H. J., Ion Exchange Absorption of Cesium by Potassium Hexacyanocobalt (II) ferrate (II). *J. Inorg. Nucl. Chem.* **1965**, *27* (2), 473-479.
16. Nilchi, A.; Saberi, R.; Moradi, M.; Azizpour, H.; Zarghami, R., Adsorption of Cesium on Copper Hexacyanoferrate-PAN Composite Ion Exchanger from Aqueous Solution. *Chem. Eng. J.* **2011**, *172* (1), 572-580.
17. Sangvanich, T.; Sukwarotwat, V.; Wiacek, R. J.; Grudzien, R. M.; Fryxell, G. E.; Addleman, R. S.; Timchalk, C.; Yantasee, W., Selective Capture of Cesium and Thallium from Natural Waters and Simulated Wastes with Copper Ferrocyanide Functionalized Mesoporous Silica. *J. Hazard. Mater.* **2010**, *182* (1-3), 225-231.
18. Lin, Y.; Fryxell, G. E.; Wu, H.; Engelhard, M., Selective Sorption of Cesium Using Self-Assembled Monolayers on Mesoporous Supports. *Environ. Sci. Technol.* **2001**, *35* (19), 3962-6.
19. Mimura, H.; Kanno, T., Distribution and Fixation of Cesium and Strontium in Zeolite A and Chabazite. *J. Nucl. Sci. Technol.* **1985**, *22* (4), 284-291.
20. Abusafa, A.; Yücel, H., Removal of <sup>137</sup>Cs from Aqueous Solutions Using Different Cationic Forms of a Natural Zeolite: Clinoptilolite. *Sep. Purif. Technol.* **2002**, *28* (2), 103-116.
21. Anthony, R. G.; Dosch, R. G.; Gu, D.; Philip, C. V., Use of Silicotitanates for Removing Cesium and Strontium from Defense Waste. *Ind. Eng. Chem. Res.* **1994**, *33* (11), 2702-2705.
22. Samanta, S. K.; Theyyanni, T. K.; Misra, B. M., Column Behaviour of Resorcinol-Formaldehyde Polycondensate Resin for Radiocesium Removal from Simulated Radwaste Solution. *J. Nucl. Sci.*

*Technol.* **1995**, 32 (5), 425-429.

23. Dozol, J. F.; Dozol, M.; Macias, R. M., ChemInform Abstract: Extraction of Strontium and Cesium by Dicarbolides, Crown Ethers and Functionalized Calixarenes. *J. Inclusion Phenom. Macrocyclic Chem.* **2001**, 32 (5).

24. Mimura, H.; Yamagishi, I., (3) Development of Composite Adsorbents for High Decontamination and Their Selective Adsorption Properties. *J. Ion Exch.* **2012**, 23 (2), 29-42.

25. Nishihara, H.; Mukai, S. R.; Fujii, Y.; Tago, T.; Masuda, T.; Tamon, H., Preparation of Monolithic SiO<sub>2</sub>-Al<sub>2</sub>O<sub>3</sub> Cryogels with Inter-Connected Macropores through Ice Templating. *J. Mater. Chem.* **2006**, 16 (31), 3231-3236.

26. Kozeny, J., Ueber Kapillare Leitung des Wassers im Boden. *Sitzungsber. Akad. Wiss. Wien* **1927**, 136, 271-306.

27. Carman, P. C., Fluid Flow through Granular Beds. *Trans. Inst. Chem. Eng.* **1937**, 15, 150-166.

28. Bispo, I.; Fedoroff, M.; Loos-neskovic, C.; Vidal-madjar, C., Sorption of Cesium on Copper Hexacyanoferrate/Polymer/Silica Composites in Batch and Dynamic Conditions. *J. Radioanal. Nucl. Chem.* **2002**, 252 (3), 497-501.

29. Park, Y.; Shin, W.; Choi, S.-J., Removal of Co, Sr and Cs from Aqueous Solution Using Self-Assembled Monolayers on Mesoporous Supports. *Korean J. Chem. Eng.* **2012**, 29 (11), 1556-1566.

# ***Chapter 4***

## ***Separation of Cesium Ion in Flow Systems Using Ammonium Molybdophosphate Supported in a Silica Microhoneycomb***

### **4.1 Introduction**

In previous chapter, Persian blue analogues (PBAs) supported monolithic microhoneycombs (PBAs-SAMH) were studied to remove  $\text{Cs}^+$  from its aqueous solution. PBAs are inexpensive and have a high  $\text{Cs}^+$  separation performance, however, toxic gas, e.g. hydrocyanic acid, occurs by thermal decomposition of PBAs.<sup>1</sup>  $\text{Cs}^+$  adsorbed materials should be stored carefully because radioactive cesium, such as  $^{137}\text{Cs}$ , emits heat decay for a long time. To avoid such problem, another ion exchangers have been suggested.

In this chapter, we applied ammonium molybdophosphate (AMP), which is a typical heteropoly compound, to  $\text{Cs}^+$  removal.<sup>2-10</sup> AMP is promising material because it shows a high selectivity towards cesium cations ( $\text{Cs}^+$ ) even in the presence of other alkali metal cations and protons (e.g. distribution coefficient  $K_d > 10^4 \text{ g}\cdot\text{mL}^{-1}$  in the presence of  $1 \text{ mol}\cdot\text{L}^{-1}\text{-H}^+$  or  $0.1 \text{ mol}\cdot\text{L}^{-1}\text{-Na}^+$  <sup>3</sup>), and is stable under acidic conditions.<sup>2</sup> This material is also relatively stable against irradiation.<sup>7</sup>

In this chapter, first, to optimize the amount of immobilized AMP in AMP-SMH, a series of AMP-SMH was synthesized and the morphology, porous properties and nanostructure of them were characterized by scanning electron microscope (SEM) observation,  $\text{N}_2$  adsorption-desorption experiments, Fourier transform infrared (FT-IR) spectroscopy and X-ray diffraction (XRD) measurements. The pressure drop the AMP-SMH causes when water was passed through them was also measured to clarify how the amount of immobilization affects hydraulic resistance. Then, to evaluate the  $\text{Cs}^+$  uptake capacity of AMP-SMH, adsorption experiments in batch systems were conducted. Finally, to clarify the effects of operation conditions on the  $\text{Cs}^+$  separation performance of AMP-SMH in flow systems, breakthrough experiments were conducted. The obtained results were

analyzed using a mathematical model, and the results were compared with a theoretical breakthrough curve of a column packed with particles to demonstrate the superiority of AMP-SMH.

## 4.2 Materials and Methods

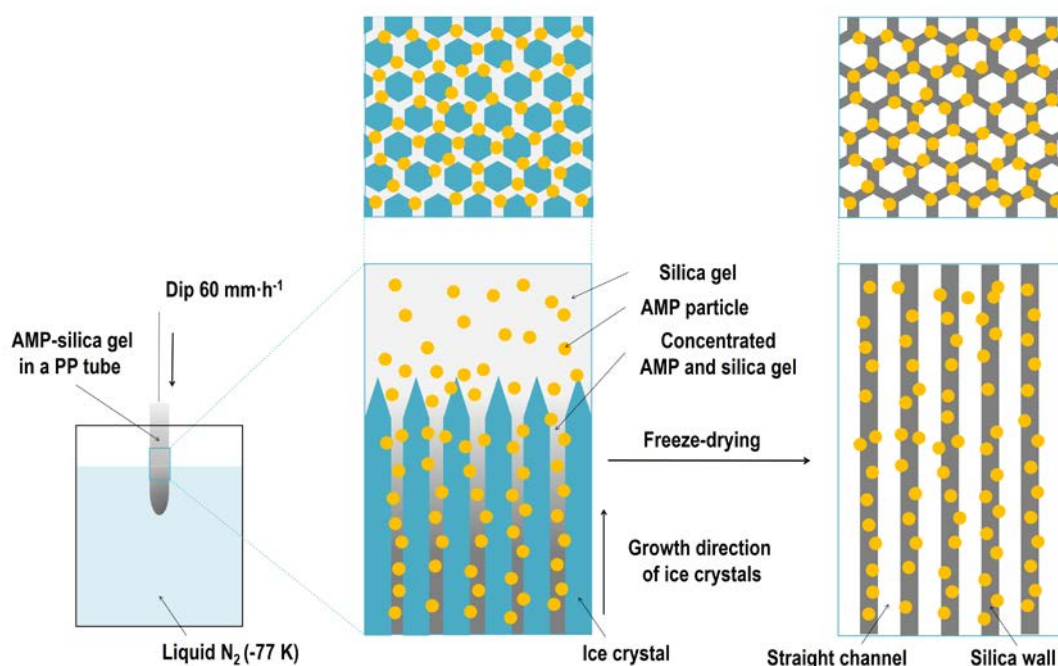
### 4.2.1 Materials

Sodium silicate solution ( $\text{Na}_2\text{SiO}_3$ , 55 wt%, molar ratio ( $\text{SiO}_2/\text{Na}_2\text{O}$ ) = 2.1), ammonium molybdophosphate ( $(\text{NH}_4)_3\text{PMo}_{12}\text{O}_{40}\cdot 3\text{H}_2\text{O}$ , AMP), 2-methyl-2-propanol (*tert*-butyl alcohol, TBA), cesium chloride (CsCl), nitric acid ( $\text{HNO}_3$ , 1 mol·L<sup>-1</sup> aqueous solution) and cesium standard solution (CsCl, 1000 ppm) were purchased from Wako Pure Chemical Industries, Ltd., Japan. All reagents were used as received.

### 4.2.2 Preparation of the AMP-SMHs

AMP-SMH were synthesized by applying the ice templating method to monolithic silica gels containing AMP particles (Scheme 4.1). Typically, a sodium silicate solution (15.4 g) was diluted with distilled water to 50 mL to adjust the concentration of the sodium silicate solution to 1.9 mol·L<sup>-1</sup>. The solution pH was adjusted to around 3.0 by adding 70 mL of an ion-exchange resin (Amberlite<sup>TM</sup> IR120B, Organo Corp.) to it. After removing the resin, AMP was added to the solution to obtain a sample with a specified content  $x$  ( $x = 0.1, 0.3, 0.5, 0.7$  g-AMP·(g-SiO<sub>2</sub>)<sup>-1</sup>). The slurry was mixed for 1 h to thoroughly disperse the AMP into the sol, and then, the slurry was poured into a polypropylene (PP) tube (i.d. 10 mm, length: 120 mm) and subsequently aged in an incubator (ICI-300, AS ONE Corporation) maintained at 303 K. During aging, the tube was shaken every 5 minutes. Next, the tube was dipped into a liquid nitrogen bath (77 K) at a rate of 60 mm h<sup>-1</sup> (the ice templating method, Scheme 4.1). After the tube was completely frozen, the tube was taken out from the bath and partially thawed at room temperature. The frozen gel was released from the tube, and soaked into TBA kept at 323 K for 2 days to exchange the water in the sample with TBA. During this exchange process, the TBA was renewed 3 times. Finally, the monolith was freeze-dried at 263 K under 40 Pa for 2 days by a freeze dryer (FDU-2200, Tokyo Rikakikai, Co., Ltd.). The obtained monolithic samples will be denoted as

AMP-SMH- $x$ , where  $x$  represents the content of AMP in the sample ( $\text{g-AMP} (\text{g-SiO}_2)^{-1}$ ).



**Scheme. 4.1** Synthesis of an AMP-SMH using the ice templating method

### 4.2.3 Characterization of AMP-SMH

Morphology of AMP-SMH was characterized using a scanning electron microscope (SEM, JSM-5410, JEOL Ltd.) and a field emission scanning electron microscope (FE-SEM, JSM-6500F, JEOL Ltd.).

Nitrogen adsorption and desorption experiments of the AMP-SMH were conducted using a nitrogen adsorption apparatus (77 K, BELSORP-mini, BEL Japan Inc.). Before measurements gas and water adsorbed in the samples were removed by heating the samples in Pyrex tubes at 523 K under a nitrogen flow for 4 hours. During measurements, the equilibrium time was set to 200 s.

Infrared spectra of the AMP-SMH were recorded on a Fourier transition infrared (FTIR) spectrometer (FT/IR-6100, JASCO Corporation, Japan) operated in the transmission mode under

vacuum condition with a spectral resolution of 4 cm<sup>-1</sup>. The samples were treated at 373 K under reduced pressure for 3 hours to remove adsorbed gas and water from the sample before measurements.

Powder X-ray diffraction (XRD) patterns of the AMP-SMH were recorded on a powder X-ray diffractometer with a step size of 0.02° using Cu K $\alpha$  monochromatic X-rays (JDX-8020, JEOL Ltd.).

Hydraulic resistance was evaluated by measurements of the pressure drop occurred when water passed through AMP-SMHs. Water at 291 K was fed to a AMP-SMH fixed in a heat shrinkable tube (Perfluoroalkoxy (PFA) polymer, i.d. 10.6 mm) at a flow rate of 0 to 10 mL·min<sup>-1</sup> by an HPLC pump (880-PU, JASCO Corporation, Japan). The pressure drop which occurred was measured using a pressure sensor (PA-853, Copal Electronics, Japan).

AMP-SMH can be modeled as a bundle of capillary tubes, so and the pressure drop which occurs when water flows through it can be estimated using the Hagen-Poiseuille equation (Eq. (4.1)), which assumes a laminar flow in a straight tube.<sup>11</sup>

$$\Delta P = \frac{32\mu u_i L}{d^2} \quad (4.1)$$

Here,  $\Delta P$  represents the pressure drop,  $\mu$  the viscosity of water,  $u_i$  the interstitial velocity ( $u_i = u_s \varepsilon^{-1}$ , where  $u_s$  represents the superficial velocity, and  $\varepsilon$  the porosity calculated from cross-sectional SEM images ( $\sim 0.85$ )),  $L$  the tube length and  $d$  represents the tube diameter. In this calculation, the length of AMP-SMH was used as  $L$ , and the average channel diameter of AMP-SMH was used as  $d$ . The pressure drop which occurs in a column packed with spherical particles was estimated using the Kozeny-Carman equation (Eq. (4.2)).<sup>12</sup>

$$\Delta P = 36\kappa \frac{(1-\varepsilon_p)^2}{\varepsilon_p^3} \frac{\mu u_s L_p}{d_p^2} \quad (4.2)$$

Here,  $\Delta P$  represents the pressure drop,  $\kappa$  the Kozeny-Carman constant (set to 5),  $\varepsilon_p$  the bed porosity (set to a typical value of 0.4),  $L_p$  the length of the bedded particles and  $d_p$  represents the particle diameter.  $L_p$  can be calculated using Eq. (4.3) which shows that its total adsorbent volume, excluding voids, is as same as the monolith.

$$L_p = \left( \frac{1-\varepsilon}{1-\varepsilon_p} \right) L \quad (4.3)$$

Here,  $\varepsilon$ ,  $\varepsilon_p$  and  $L_p$  represent the void fraction of the monolith (= 0.85), the void fraction of a column packed with spherical particles (set to a typical value of 0.4) and the length of the monolith, respectively.

#### 4.2.4 Cs<sup>+</sup> Adsorption Experiments Using AMP-SMH in a Batch System

Cs<sup>+</sup> adsorption experiments using AMP-SMH were conducted in a batch system. In experiments, one hundred milligram of a crushed AMP-SMH was introduced into a glass vial containing a 25-mL Cs<sup>+</sup> aqueous solution (concentration: 150 to 500 ppm) and equipped with a stir bar. The vial was placed in a bath maintained at 298 K, and the slurry in it was stirred vigorously using the stir bar. After 24 h, an aliquot of the slurry was sampled and filtered using a disposable PP syringe, and syringe filter (pore size 0.22  $\mu\text{m}$ , polyethersulfone, Membrane Solutions Co., Ltd.). The filtrate was analyzed using an ion chromatography system (JASCO Corporation, Japan) equipped with a conductivity detector (CD-200, Showa Denko K.K., Japan) with 4 mmol L<sup>-1</sup> nitric acid as the eluent. Uptake of Cs<sup>+</sup> at equilibrium was calculated from the difference in the initial and final concentrations by Eq. (4.4) assuming that the solution volume was constant.

$$q = (C_0 - C_e) \frac{v}{m} \quad (4.4)$$

Here,  $q$  represents the amount of Cs<sup>+</sup> adsorbed on AMP-SMH,  $C_0$  and  $C_e$  respectively represent the initial and the equilibrium Cs<sup>+</sup> concentration of the solution,  $v$  represents the solution volume, and  $m$  represents the mass of the AMP-SMH.

The obtained adsorption isotherms were analyzed by the Langmuir equation (Eq. (4.5))

$$q = \frac{q_m K_L C_e}{1 + K_L C_e} \quad (4.5)$$

Here,  $q_m$  represents the maximum Cs<sup>+</sup> loading of the AMP-SMH and  $K_L$  represents the adsorption-equilibrium constant.

#### 4.2.5 Cs<sup>+</sup> Adsorption Experiments Using AMP-SMH in Flow Systems

Cs<sup>+</sup> adsorption experiments were conducted in a flow system using AMP-SMH (diameter:  $\sim 10 \mu\text{m}$ , length: 9-27 mm). An AMP-SMH was fixed in a heat shrinkable tube and the tube was set

vertically in an incubator maintained at 298 K (Fig. 4.1). An aqueous solution containing a specified concentration of  $Cs^+$  was fed from the bottom of the tube using an HPLC pump (880-PU, JASCO Corporation, Japan). An aliquot of the effluent was sampled and filtered through a syringe filter by a disposable PP syringe. The  $Cs^+$  concentration was analyzed by the same procedure as that used in the batch system.

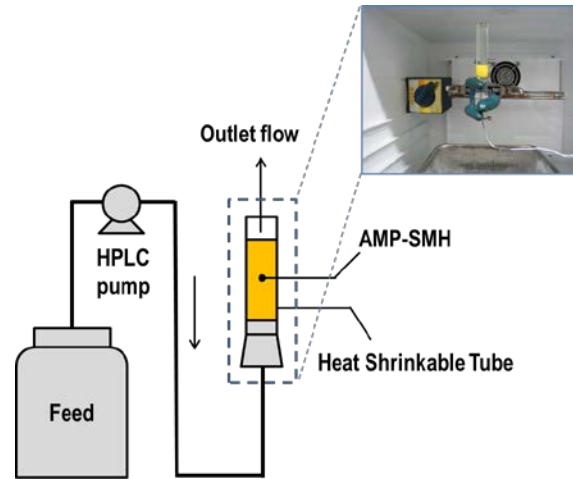


**Fig. 4.1** The apparatus for a flow adsorption system

The length of unused bed (LUB), which represents the length of the region where adsorption actually takes place in a packed bed, is calculated using Eq. (4.6).<sup>13</sup>

$$LUB = (V_s - V_b) \frac{L}{V_s} \quad (4.6)$$

Here,  $V_b$  represents the 5 % breakthrough volume and  $V_s$  represents the stoichiometric volume calculated using graphical integration shown in Eq. (4.7).

$$V_s = \int_0^{V_e} \left( 1 - \frac{C}{C_f} \right) dV \quad (4.7)$$

Here,  $V$  is the effluent volume,  $V_e$  is the 95 % breakthrough volume,  $C$  and  $C_f$  represent effluent concentration and feed concentration of  $Cs^+$ , respectively.

The  $Cs^+$  capacity of AMP-SMH in a flow system,  $q_f$ , is calculated using Eq. (4.8).

$$q_f = \frac{V_s C_f}{m} \quad (4.8)$$

To compare the breakthrough curves with theoretical curve a series of equations are used. Firstly,

the overall mass transfer coefficient  $k$  and dimensionless Henry's law adsorption equilibrium constant  $K$  were calculated by curve fitting using Eq. 4.11. And then, the effective diffusivity  $D_e$  was calculated using Eq. (4.14)-(4.19). The experimental values are shown in Table 4.3.

Mass balance of a packed bed can be written as Eq. (4.9).<sup>13</sup>

$$-D_L \frac{\partial^2 C}{\partial z^2} + \frac{\partial(u_i C)}{\partial z} + \frac{\partial C}{\partial t} + \left( \frac{1-\varepsilon}{\varepsilon} \right) \frac{\partial \bar{q}}{\partial t} = 0 \quad (4.9)$$

Here,  $D_L$ ,  $C$ ,  $z$ ,  $t$ , and  $\bar{q}$  represent axial diffusivity, concentration of  $Cs^+$ , distance from the entrance, time and average loading of  $Cs^+$ , respectively. Under the linear driving force (LDF) approximation and assuming a linear equilibrium isotherm, the adsorption rate can be written as Eq. (4.10).<sup>14</sup>

$$\frac{\partial \bar{q}}{\partial t} = k(q^* - \bar{q}) = kK(C - C^*) \quad (4.10)$$

Here,  $q^*$  ( $\text{mmol} \cdot \text{m}^{-3}$ ) represents the uptake of  $Cs^+$  equilibrated to  $C$ , and  $C^*$  represents the concentration equilibrated to  $\bar{q}$ . The analytical solution of Eq. (4.9) and (4.10) when axial dispersion is neglected ( $D_L = 0$ ) is shown in Eq. 4.11.

$$\frac{C}{C_f} = \frac{1}{2} \left[ 1 + \text{erf} \left( \sqrt{\tau} - \sqrt{\xi} + \frac{1}{8\sqrt{\tau}} + \frac{1}{8\sqrt{\xi}} \right) \right] \quad (4.11)$$

Here,  $\tau$ ,  $\xi$  and erf represent the dimension less time, the dimension less distance and the error function defined as Eq. (4.12), (4.13) and (4.14), respectively.

$$\tau = k \left( t - \frac{L}{u_i} \right) \quad (4.12)$$

$$\xi = \frac{kKL}{u_i} \left( \frac{1-\varepsilon}{\varepsilon} \right) \quad (4.13)$$

$$\text{erf}(x) = \frac{2}{\sqrt{\pi}} \int_0^x \exp(-s^2) ds \quad (4.14)$$

We assume that the total mass transfer coefficient ( $kK$ ) is governed by external mass transfer, intraparticle mass transfer and axial dispersion as shown in Eq. (4.15).<sup>14</sup>

$$\frac{1}{kK} = \frac{1}{a_v k_f} + \frac{1}{k_p D_e} \quad (4.15)$$

In this equation,  $a_v$ ,  $k_f$ ,  $k_p$  and  $D_e$  represent the external surface area of adsorbent per unit volume

of adsorbent (not containing voids in the bed), external mass transfer coefficient, intraparticle mass transfer coefficient and effective diffusivity, respectively. As it is difficult to model AMP embedded channel walls, we assume that AMP particles are uniformly dispersed in the cylindrical channel walls and neglect the overhanging part of the particles. Therefore, the calculated  $D_e$  value is the averaged diffusivity of the whole of channel walls.

The external mass transfer coefficient ( $k_f$ ) within monolith channels can be estimated from the Sherwood number ( $Sh$ ) which can be calculated using Eq. (4.16).<sup>15, 16</sup>

$$Sh = \frac{k_f d}{D_m} = Sh_\infty \left[ 1 + c \left( \frac{d}{L} \right) Re Sc \right]^{0.45} \quad (4.16)$$

In this equation,  $D_m$ ,  $Sh_\infty$ ,  $c$ ,  $Re$  and  $Sc$  represent molecular diffusivity of solute ( $\text{m}^2 \cdot \text{s}^{-1}$ ), asymptotic Sherwood number for fully developed flow specific to the channel geometry (= 3.66 for circular channel<sup>15</sup>), tube roughness constant, Reynolds number defined as Eq. (4.17) and Schmidt number defined as Eq. (4.18), respectively. The  $D_m$  value used was  $2.1 \times 10^{-9} \text{m}^2 \cdot \text{s}^{-1}$ .<sup>17</sup>

$$Re = \frac{du_i \rho}{\mu} \quad (4.17)$$

$$Sc = \frac{\mu}{\rho D_m} \quad (4.18)$$

Here,  $\rho$  represents the density of fluid. If  $c(D/L)ReSc$  in Eq. (4.16) is negligible,  $Sh$  reaches a constant value “ $Sh_\infty$ ”. Therefore, in this calculation,  $Sh$  was set to 3.66. The  $k_p$  of a hollow cylinder insulated external surface can be calculated using Eq. (4.19).<sup>16</sup>

$$k_p = \frac{4}{\left\{ \left[ \left( \frac{r_0}{r_i} \right) - 1 \right] (r_0^2 - r_i^2) - \left( \frac{1}{r_i (r_0 - r_i)} \right) \left[ \frac{1}{2} (r_0^4 - r_i^4) - \frac{4r_0}{3} (r_0^3 - r_i^3) + r_0^2 (r_0^2 - r_i^2) \right] \right\}} \quad (4.19)$$

In this equation,  $r_0$  and  $r_i$  respectively represent the outer radius and the inner radius of the channel when it is assumed that the microhoneycomb structure can be regarded as a bundle of capillaries. From measurements of the pressure drop, the calculated  $d$  values of AMP-SMH- $x$  are almost the same (20-22 $\mu\text{m}$ ), therefore, we set  $r_i$  as 10.5  $\mu\text{m}$  ( $d = 21.0 \mu\text{m}$ ).  $r_0$  was calculated from cross-sectional porosity ( $\varepsilon = r_i^2 / r_0^2 = 0.85$ ) because it is difficult to estimate the thickness of the channel wall ( $= 2 \times (r_0 - r_i) = 1.8 \mu\text{m}$ ). In this calculation, the hanging out part of AMP particles are

not considered in the channel structure, therefore, the calculated  $D_e$  value is an apparent values.

To compare the  $\text{Cs}^+$  separation performance of the AMP-SMH-0.5 in a continuous system with a typical column packed with particles causing the same pressure drop, the theoretical breakthrough curve of the particles were simulated. The simulational breakthrough curve can be calculated using Eq. (4.11) in a similar manner as the monolith. In case of a typical column packed with spherical particles, Eq. (4.15) can be rewritten as Eq. (4.20).<sup>14</sup>

$$\frac{1}{kK} = \frac{d_p}{6k_f} + \frac{d_p^2}{60D_e} \quad (4.20)$$

$k_f$ , values of a column packed with particles can be calculated by using Eq. (4.21).<sup>18</sup>

$$\frac{k_f}{u_s} Sc^{0.58} = 2.40 \left( \frac{Re_p}{\varepsilon} \right)^{-0.66} \quad (4.21)$$

Reynolds number ( $Re_p$ ) can be calculated using the following Eq. (4.22).

$$Re_p = \frac{d_p u_s \rho}{\mu} \quad (4.22)$$

$d_p$  was set to the equivalent diameter of a typical column packed with particles which shows the same total pressure drop as AMP-SMH-0.5 (~ pressure drop of a tube which diameter is 21  $\mu\text{m}$ ).

**Table 4.1** Physical properties of AMP-SMHs and results from batch adsorption experiments of  $\text{Cs}^+$

$x$ /g-AMP·(g-SiO <sub>2</sub> ) <sup>-1</sup>	$\rho_B$ <sup>a</sup> /g·mL <sup>-1</sup>	$d_{SEM}$ <sup>b</sup> / $\mu\text{m}$	$d$ <sup>c</sup> / $\mu\text{m}$	$q_m$ /mmol·g <sup>-1</sup>	$K_L$ /L·mmol <sup>-1</sup>	$q_{\text{theor.}}$ <sup>d</sup> /mmol·g <sup>-1</sup>	$q_m \cdot q_{\text{theor.}}$ <sup>-1</sup> /-
0.0	0.16	25 ± 3	n.d. <sup>e</sup>	0.01	4.4	-	-
0.1	0.15	29 ± 1	21	0.06	5.3	0.10	0.60
0.3	0.16	28 ± 2	20	0.20	21.7	0.24	0.83
0.5	0.22	21 ± 3	22	0.33	22.5	0.34	0.97
0.7	0.27	21 ± 2	n.d. <sup>e</sup>	0.32	46.6	0.43	0.74

<sup>a</sup> Bulk density of AMP-SMH- $x$ . <sup>b</sup> Average microchannel size calculated by averaging sizes of 50 channels observed in SEM images. <sup>c</sup> Microchannel size derived from applying pressure drop data to the Eq. (1). <sup>d</sup> Maximum uptake of  $\text{Cs}^+$  calculated by assuming that two  $\text{NH}_4^+$  per AMP cluster can be exchanged with  $\text{Cs}^+$ . <sup>e</sup> Not determined.

**Table 4.2** Results from flow adsorption experiments of Cs<sup>+</sup> <sup>a</sup>

Run	$x$ /g-AMP·(g-SiO <sub>2</sub> ) <sup>-1</sup>	$u_s$ / mm·min <sup>-1</sup>	$L$ / mm	LUB / mm	LUB·L <sup>-1</sup> /-	$q_f$ /mmol·g <sup>-1</sup> 1	$q_f·q_m^{-1}$ /-
1	0.1	93	23	6	0.27	0.07	1.2
2	0.3	93	23	6	0.26	0.20	1.0
3	0.5	93	23	5	0.22	0.38	1.1
4	0.5	31	9	4	0.44	0.34	1.0
5	0.5	64	9	3	0.33	0.31	0.9
6	0.5	112	9	3	0.33	0.33	1.0
7	0.5	100	10	4	0.40	0.34	1.0
8	0.5	100	15	3	0.21	0.32	0.9
9	0.5	100	27	5	0.19	0.35	1.0

<sup>a</sup>These adsorption experiments were conducted at 298 K, the diameter of the AMP-SMH was 10 mm and feed Cs<sup>+</sup> concentration was 10 ppm.

**Table 4.3** The experimental values calculated from the breakthrough curves

Run	$k$ / s <sup>-1</sup>	$K$ / -	$\zeta$ / -	$Re$ / -	$D_e$ / m <sup>2</sup> ·s <sup>-1</sup> × 10 <sup>11</sup>
1	0.03	1000	64	0.043	1.7
2	0.01	3000	66	0.043	1.9
3	0.01	6800	151	0.043	2.3
4	0.002	6500	38	0.014	0.4
5	0.003	6500	26	0.029	0.6
6	0.01	6500	47	0.052	2.2
7	0.01	6500	56	0.046	2.2
8	0.01	7000	91	0.046	2.4
9	0.01	6000	146	0.046	2.0

**Table 4.4** Parameters for simulation of breakthrough curves.

		AMP-SMH-0.5	Particles
Porosity	$\varepsilon$ / -	0.85	0.40
Monolith length/Bed height	$L$ or $L_p$ / cm	12.0	3.0
Channel diameter/Particle diameter	$d$ or $d_p$ / $\mu\text{m}$	21.0	54.5
Superficial velocity	$u_s$ / $\text{mm}\cdot\text{min}^{-1}$	100	
Interstitial velocity	$u_i$ / $\text{mm}\cdot\text{min}^{-1}$	118	250
Total pressure drop	$\Delta P$ / kPa	15.2	
Overall effective mass transfer coefficient	$k$ / $\text{s}^{-1}$	0.01	$6.7\times 10^{-5}$
Dimensionless Henry's law adsorption equilibrium constant	$K$ / -	6000	
Reynolds number	$Re$ or $Re_p$	0.046	0.10
Sherwood number	$Sh$	3.7	9.6
Schmidt number	$Sc$	425	
Film mass transfer coefficient	$k_f$ / $\text{m}\cdot\text{s}^{-1}$	$3.5\times 10^{-4}$	$3.0\times 10^{-4}$
External surface area	$a_v$ / $\text{m}^{-1}$	$1.1\times 10^6$	$1.1\times 10^5$
Effective diffusivity	$D_e$ / $\text{m}^2\cdot\text{s}^{-1}$	$2.0\times 10^{-11}$	
Intraparticle mass transfer coefficient	$k_p$ / $\text{m}^2$	$3.6\times 10^{12}$	$2.0\times 10^{10}$
Length of unused bed	LUB / mm	11	27

## 4.3 Results and Discussion

### 4.3.1 Characterization of Synthesized AMP-SMHs

Synthesized materials show a typical microhoneycomb structure when AMP content is relatively low ( $x \leq 0.5$ ) as shown by SEM images in Fig. 4.2 (a)-(c). For example, AMP-SMH-0.5 has a cylindrical shape 10 mm in diameter and a few tens of mm in length with microchannel openings approximately 21  $\mu\text{m}$  in diameter. Small particles ( $\sim 10 \mu\text{m}$ ), which are likely to be AMP, are immobilized in the microhoneycomb walls without clogging the microchannels. On the other hand, when the amount of AMP was high ( $x = 0.7$ ), AMP particles aggregated and partially blocked the microchannels as shown in Fig. 4.2 (d).

Nitrogen adsorption isotherms of all materials (Fig. 4.3) show type I isotherms,<sup>19</sup> indicating that the materials are microporous (SMH and AMP-SMH are macro-microporous). AMP-SMH-0.5 shows

a lower BET surface area ( $S_{\text{BET}}$ ) than SMH, which can be accounted for by the lower contribution to surface area from AMP. The sample contains 33 wt% AMP particles. Thus, addition of the surface area from AMP particles ( $220 \times 0.33 \text{ m}^2 \cdot \text{g}^{-1}$ ) and that from SMH ( $830 \times 0.67 \text{ m}^2 \cdot \text{g}^{-1}$ ) gives estimation of the surface area ( $629 \text{ m}^2 \cdot \text{g}^{-1}$ ), which is close to the  $S_{\text{BET}}$  of AMP-SMH-0.5. Thus, the data indicate that the immobilization of AMP particles did not alter the porous properties of the SMH matrix.

FT-IR spectra of AMP-SMHs (Fig. 4.4) show the peaks associated with the  $\alpha$ -Keggin anion ( $\text{PMo}_{12}\text{O}_{40}^{3-}$ ): 595 (bending mode of O-P-O), 790 (asymmetric stretching mode of Mo-O<sub>2c1</sub>-Mo), 865 (asymmetric stretching mode of Mo-O<sub>2c2</sub>-Mo), 960 (asymmetric stretching mode of Mo-O<sub>t</sub>), 1,060  $\text{cm}^{-1}$  (asymmetric stretching mode of P-O).<sup>20-22</sup> The peak at 1,400  $\text{cm}^{-1}$  is attributable to the bending mode of N-H of  $\text{NH}_4^+$ .<sup>20</sup>

The XRD patterns for AMP-SMHs show that the crystal structure of AMP is maintained after immobilization (Fig. 4.5), showing that AMP clusters are intact after immobilization.

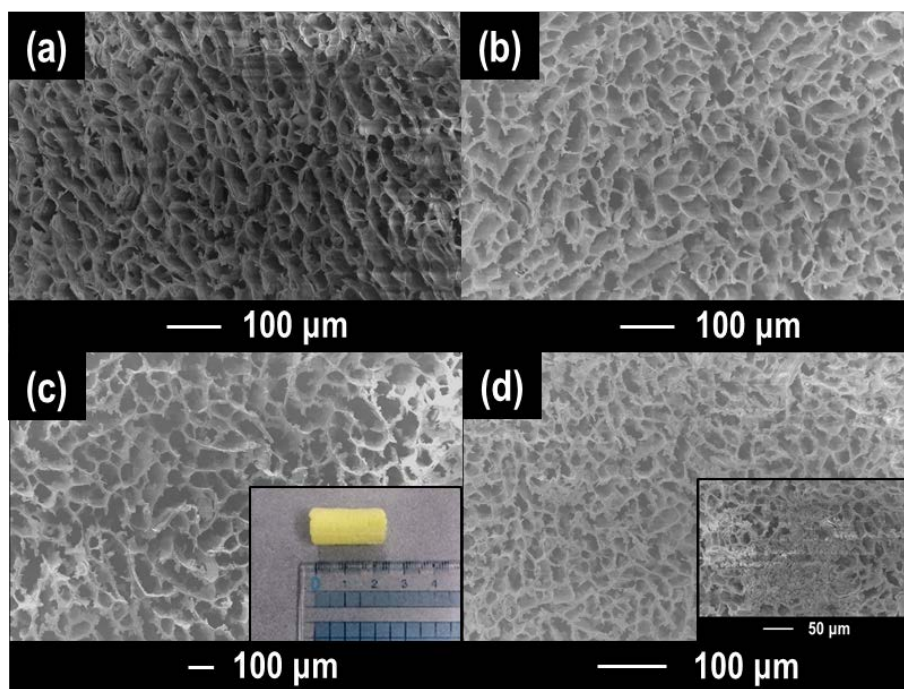


**Fig. 4.2** Cross-sectional SEM images of AMP-SMH- $x$ : (a)  $x = 0.1$ , (b)  $x = 0.3$ , (c)  $x = 0.5$  and (d)  $x = 0.7$

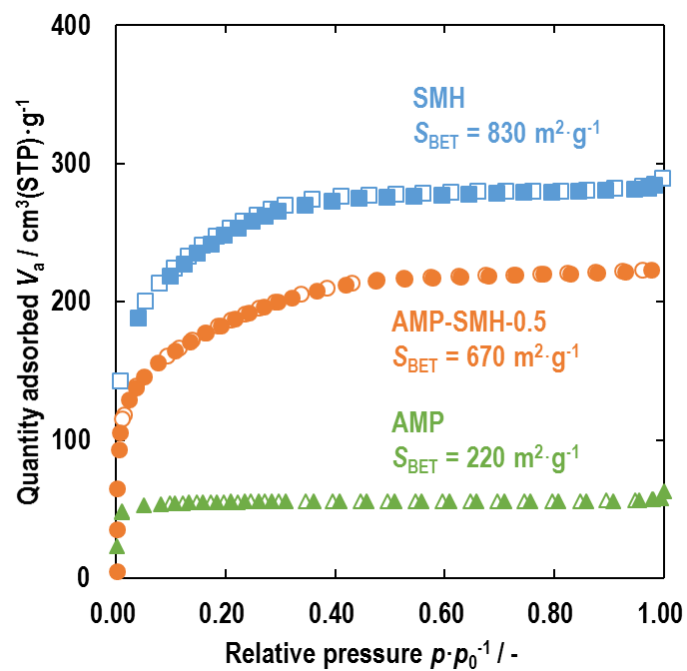


**Fig. 4.3** N<sub>2</sub> adsorption/desorption isotherms of AMP, SMH and AMPS-SMH-0.5

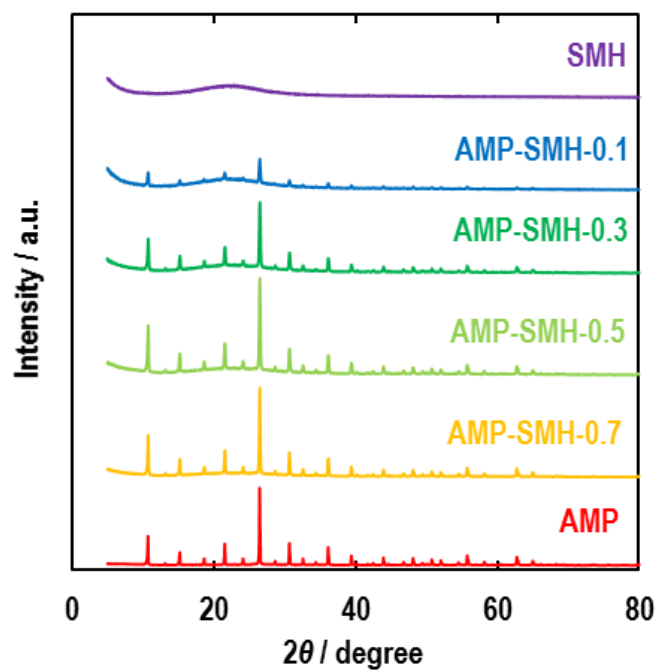


**Fig. 4.4** XRD patterns of AMP-SMH- $x$  and SMH.

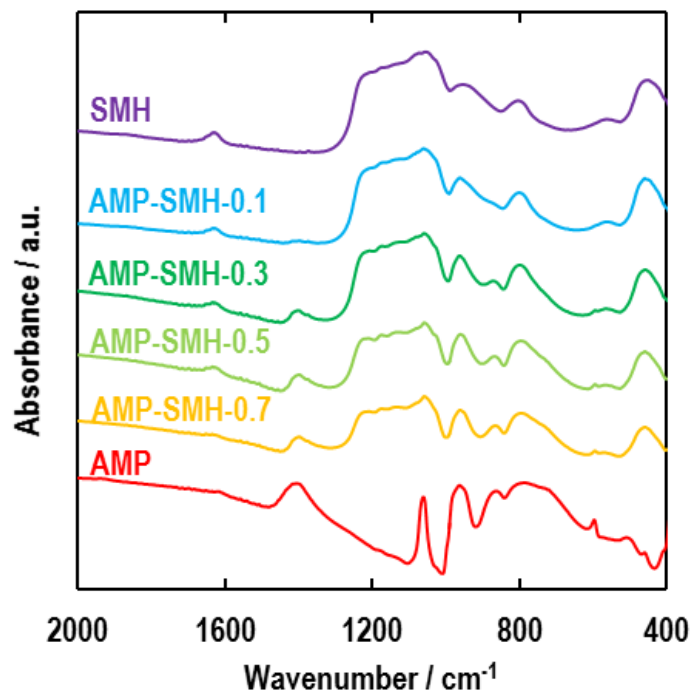


**Fig. 4.5** FTIR spectra of AMP-SMH- $x$  and SMH.

To evaluate the hydraulic resistance of AMP-SMH and to compare it with that a column packed with particles causes, the pressure drop which occurs when water is passed through AMP-SMH was measured. All of the pressure drop data for three AMP-SMHs ( $x = 0.1, 0.3,$  and  $0.5$ ) increased linearly with increasing superficial velocity (Fig. 4.6), and almost overlap each other, consistent with their similar microchannel sizes and the absence of pore blockage by AMP. Analysis of the pressure drop by the Hagen-Poiseuille equation gave an estimate of the microchannel diameter to be approximately  $21 \mu\text{m}$ , corresponding to the average microchannel size of AMP-SMHs. Thus, these results indicate that AMP-SMH can be regarded as a bundle of straight capillary tubes with AMP particles embedded in their walls. Because the immobilized AMP particles are about  $10 \mu\text{m}$  in diameter, the pressure drop which occurs in a column packed with  $10\text{-}\mu\text{m}$  particles was estimated using the Kozeny-Carman equation. The results show that AMP-SMHs cause a 35-fold lower pressure drop than the packed-column. This result suggests that AMP-SMH can show a higher performance for  $\text{Cs}^+$  separation in flow systems when compared with a column packed with particles having a similar diffusion path

length.

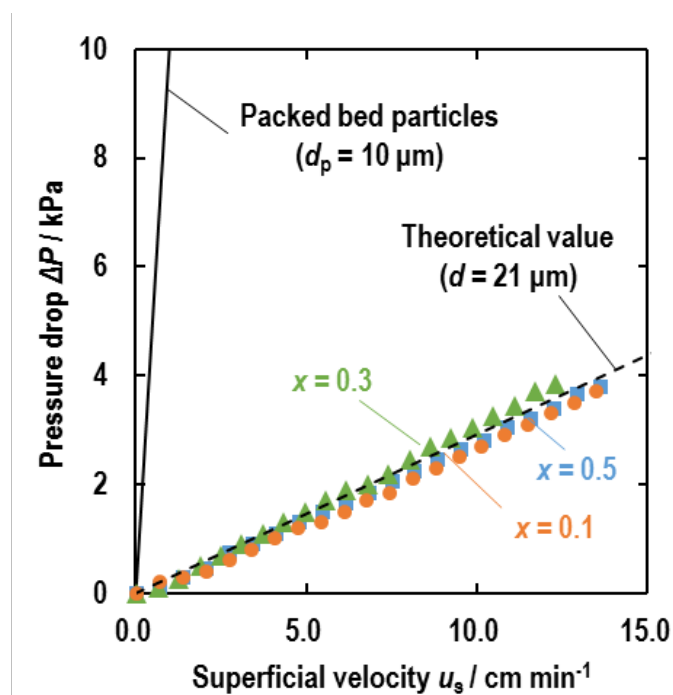


**Fig. 4.6** Pressure drop data of water flowing through the AMP-SMH- $x$ :  $x = 0.1$  (orange circle), 0.3 (green triangle), and 0.5 (blue square). Monolith length: 23 mm, monolith diameter: 11 mm. The dotted line represents the pressure drop calculated using the Hagen-Poiseuille equation. The solid line represents the pressure drop for a column packed with particles calculated using the Kozeny-Carman equation.

### 4.3.2 Cs<sup>+</sup> Separation Experiments Using the AMP-SMHs in Batch Systems

To evaluate the Cs<sup>+</sup> adsorption capacity of AMP-SMH, batch adsorption experiments were conducted at 298 K using aqueous solutions containing 150-500 ppm Cs<sup>+</sup> (Fig. 4.7). SMH shows a significantly lower uptake of Cs<sup>+</sup> than AMP-SMH. AMP-SMH with higher AMP contents tend to show higher uptakes of Cs<sup>+</sup>, all showing higher Cs<sup>+</sup> uptake than SiO<sub>2</sub>-impregnated AMP reported in the literature (0.06 mmol·g<sup>-1</sup>)<sup>3</sup>. It is reported that about two out of three ammonium ions of AMP can be readily exchanged with Cs<sup>+</sup> ions, which corresponds to approximately 1.0 mmol·Cs<sup>+</sup>·(g-AMP)<sup>-1.2</sup>. Thus, maximum uptake of Cs<sup>+</sup> for each AMP-SMH was calculated by assuming two Cs<sup>+</sup> per AMP and compared with the data obtained from adsorption experiments (Table 4.1). The results show that AMP-

SMH-0.3 and -0.5 show uptakes close to the calculated values whereas AMP-SMH-0.1 and -0.7 show a lower uptakes probably because AMP particles in AMP-SMH-0.1 were completely embedded in the silica matrix and those in AMP-SMH-0.7 were significantly aggregated (Fig. 4.2 (d), inset), limiting the access of  $\text{Cs}^+$  to AMP.

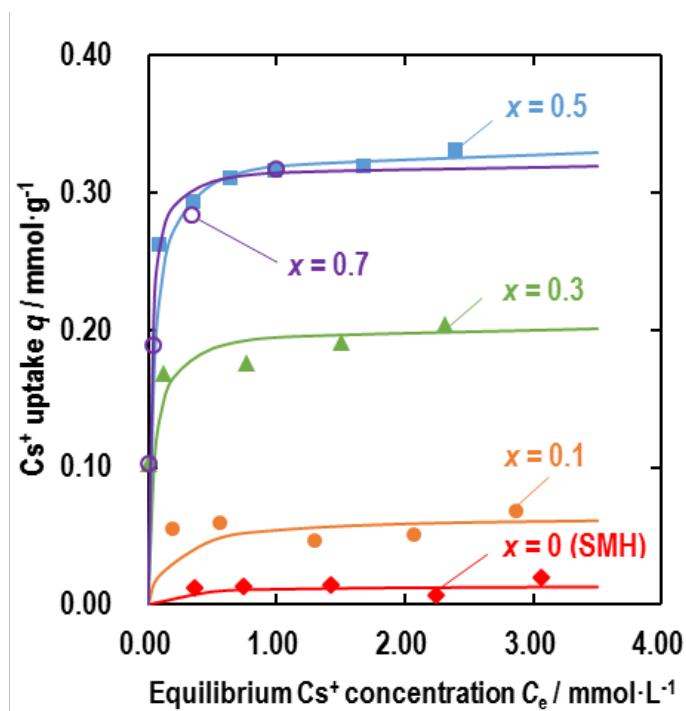


**Fig. 4.7**  $\text{Cs}^+$  adsorption isotherms of AMP-SMH- $x$  (298 K):  $x = 0$  (red rhombus),  $x = 0.1$  (orange circle),  $x = 0.3$  (green triangle),  $x = 0.5$  (blue square), and  $x = 0.7$  (open purple circle). The solid lines represent fits to the Langmuir adsorption isotherm equation.

### 4.3.3 $\text{Cs}^+$ Separation Experiments Using the AMP-SMHs in Flow Systems

To evaluate the applicability of AMP-SMH to flow adsorption systems, adsorption experiments were conducted using the system shown schematically in Fig. 4.1. First, to investigate the effect of the AMP content in AMP-SMH on the shape of breakthrough curves, breakthrough experiments were conducted using AMP-SMH with various AMP contents ( $x = 0.1, 0.3, 0.5$ ) (Fig. 4.8). The obtained curves are sigmoidal and shifted to the right direction when the AMP content was increased. The LUB of each AMP-SMH is very short (5–6 mm, Table 4.2), and much shorter than those reported for AMP immobilized in silica gel particles (LUB = 16 mm)<sup>3</sup>. The  $\text{LUB} \cdot \text{L}^{-1}$  values, indicating length based

column utilization, are 0.22-0.27 which indicates that about 75 % AMP-SMH can be effectively used for Cs<sup>+</sup> separation even though they are extremely short. The  $q_f \cdot q_m^{-1}$  values, indicating capacity based column utilization, are close to 1 which show that almost all of the Cs<sup>+</sup> exchange sites in AMP-SMH can be utilized in flow systems. These results show that AMP-SMH is able to effectively separate Cs<sup>+</sup> in flow systems.

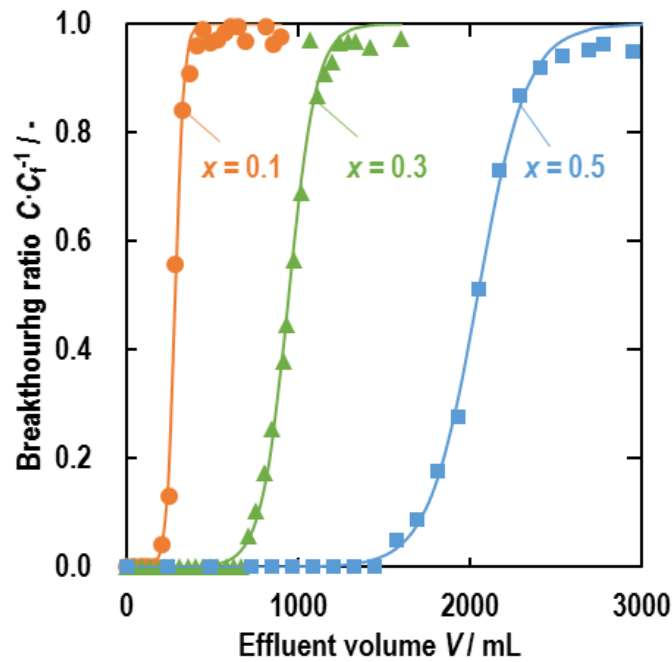


**Fig. 4.8** Breakthrough curves (Run 1-3) of AMH-SMHs for  $x = 0.1$  (solid orange circle),  $x = 0.3$  (solid green triangle), and  $x = 0.5$  (solid blue square). Conditions:  $u_s = 93 \text{ mm} \cdot \text{min}^{-1}$ ,  $C_f = 10 \text{ ppm}$ ,  $L = 23 \text{ mm}$ . Solid lines represent theoretical breakthrough curves calculated using Eq. (4.11).

Next, to investigate the effect of superficial velocity ( $u_s$ ) on the shape of breakthrough curves, breakthrough experiments were conducted at  $u_s$  from 32 to 112  $\text{mm} \cdot \text{min}^{-1}$  (Fig. 4.9). The shapes of the obtained curves were sigmoidal and independent on the variation of  $u_s$ . The  $u_s$  used in this work are extremely higher than that of the bench scale experiment using AMP loaded silica ( $4 \text{ mm} \cdot \text{min}^{-1}$ ).<sup>3</sup> As mentioned previously, the LUB value of the column used in the bench scale experiment is at least 16 mm. This comparison indicates that AMP-SMH can effectively separate Cs<sup>+</sup> in flow systems even at high  $u_s$ .

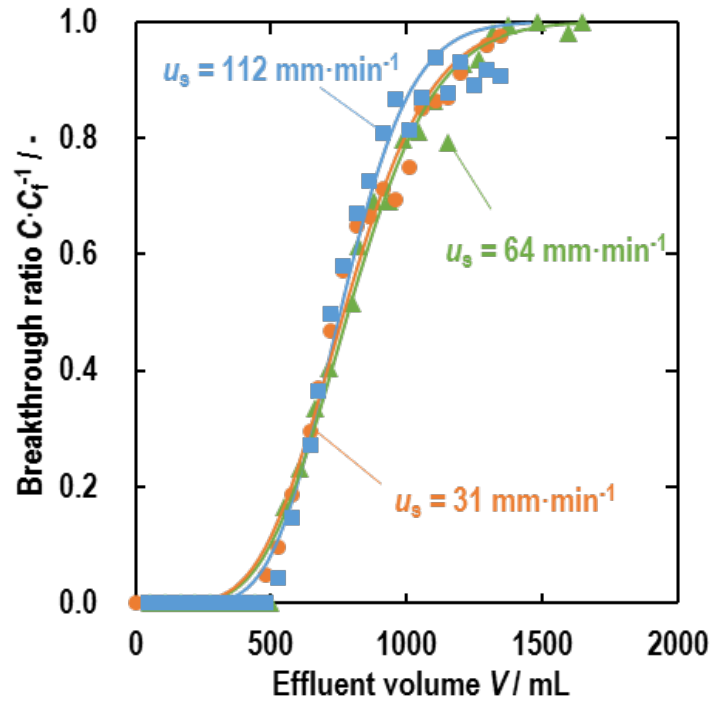


**Fig. 4.9** Breakthrough curves at various linear velocities (Run 4-6):  $u_s = 31 \text{ mm}\cdot\text{min}^{-1}$  (solid orange circle);  $u_s = 64 \text{ mm}\cdot\text{min}^{-1}$  (solid green triangle);  $u_s = 112 \text{ mm}\cdot\text{min}^{-1}$  (solid blue square),  $C_f = 10 \text{ ppm}$ ,  $x = 0.5$ ,  $L = 9 \text{ mm}$ . Solid lines represent theoretical breakthrough curves calculated using the Eq. (4.11).

To verify whether the adsorption zone has reached a constant pattern behavior,<sup>14</sup> breakthrough experiments were conducted using monolith length ( $L$ ) from 10 to 27 mm at a  $u_s$  of  $100 \text{ mm}\cdot\text{min}^{-1}$ . The obtained breakthrough curves shifted toward higher effluent volumes with increasing  $L$  without changing their shape, and the LUBs were constant (3 to 5 mm) (Fig. 4.10). It can be expected that AMP-SMH can quickly and effectively separate  $\text{Cs}^+$  from fluids, because the  $u_s$  and the  $L$  do not affect their LUB. These results show that high throughput system for  $\text{Cs}^+$  removal can be constructed using AMP-SMH.

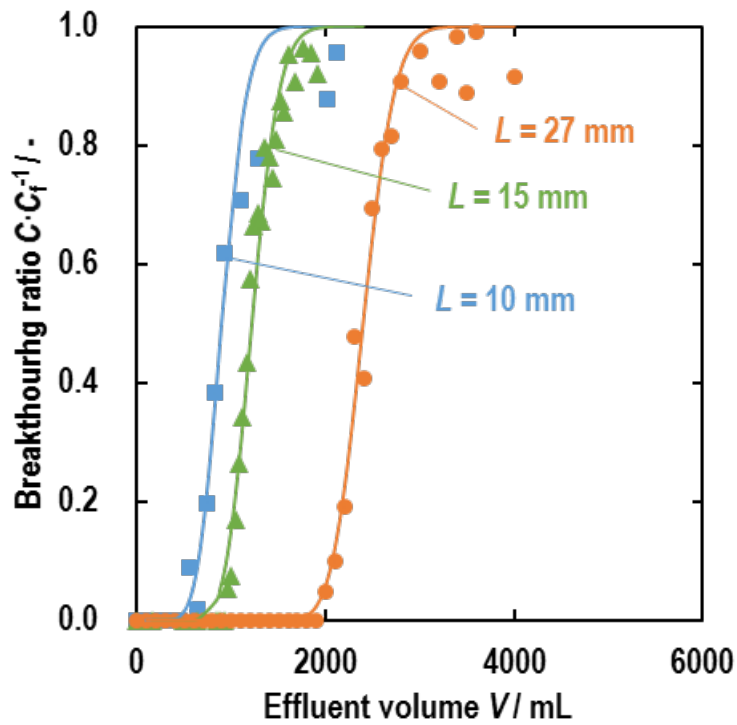


**Fig. 4.10** Breakthrough curves obtained using monoliths with various lengths (Run7-9):  $L = 27$  mm (solid orange circle);  $L = 15$  mm (solid green triangle);  $L = 10$  mm (solid blue square),  $u_s = 100$  mm·min<sup>-1</sup>,  $C_f = 10$  ppm,  $x = 0.5$ . Solid lines represent theoretical breakthrough curves calculated using the Eq. 4.11.

Finally, to compare the breakthrough curves of AMP-SMH with those of a typical column packed with particles used under the same conditions, breakthrough curves of a typical column were simulated. The physical parameters used for simulation are shown in Table 4.4. The simulated breakthrough curves of AMP-SMH-0.5 and a column packed with particles which cause the same total pressure drop are shown in Fig. 4.11. The breakthrough curve of AMP-SMH-0.5 is steeper than that of the column packed with particles. The LUB value of AMP-SMH-0.5 (11 mm) is less than half of that of the column packed with particles (27 mm) even though the total bed length of the packed column is only one quarter of that of AMP-SMH. This result indicates that 90 % of the AMP-SMH-0.5 can be used for Cs<sup>+</sup> separation until 5% breakthrough. On the other hand, only 10 % can be used in the packed column. This result indicates that AMP-SMH shows a notably higher performance for Cs<sup>+</sup> separation in flow

systems when compared with a column packed with particles used under the same conditions.

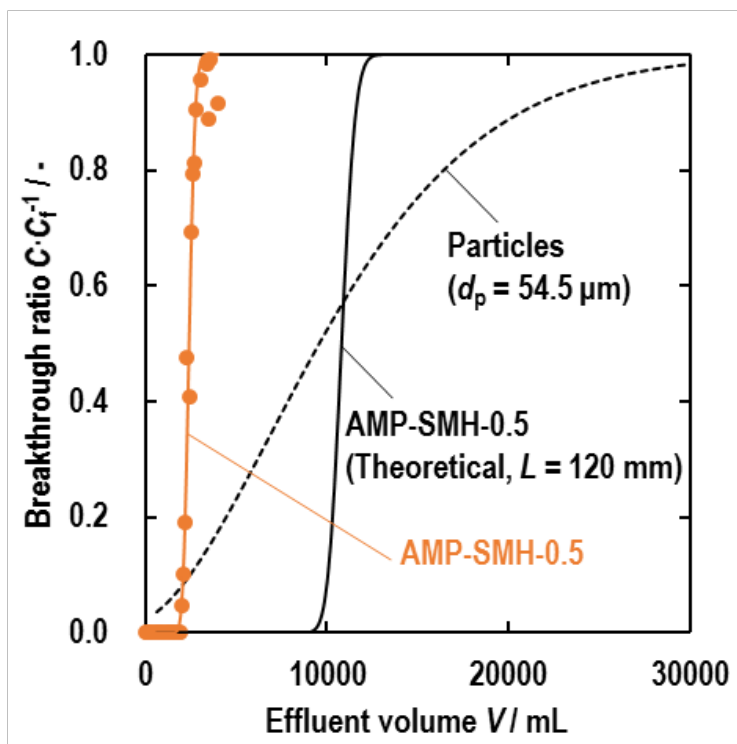


**Fig. 4.11** Simulated breakthrough curves of AMP-SMH-0.5 (black solid line) and a column packed with particles (black dashed line) calculated using the Eq. (4.1). (The parameters used for the simulation are shown in Table S2) Orange circles and the orange solid line represent the measured and the theoretical breakthrough curves of AMP-SMH-0.5, respectively (Run 9).

#### 4.4 Conclusion

AMP immobilized silica with a microhoneycomb structure (AMP-SMH) was successfully synthesized by using the ice templating method. The pressure drop which occurs when fluids flow through it was lower than that of a typical column packed with particles with the same diffusion path length causes. Adsorption experiments conducted in batch and flow systems indicate that contact efficiency of AMP-SMH-0.5 was higher than AMP-SMH with lower contents of AMP. From breakthrough experiments of  $\text{Cs}^+$  under various conditions using AMP-SMH, it was found that the LUB of AMP-SMH was very short (few mm) which indicates that effective  $\text{Cs}^+$  separation can be

achieved. Simulation data indicated that AMP-SMH can separate Cs<sup>+</sup> in a flow system more efficiently than a column packed with particles which causes a similar hydraulic resistance. These results indicate that AMP-SMH has a high potential to be used for quick and effective separation of Cs<sup>+</sup> existing in a diluted state in solutions, for example, contaminated water released from nuclear power plant in Japan.

## 4.5 Reference

1. Lehto, J.; Pettersson, M.; Hinkula, J.; Räsänen, M.; Elomaa, M., Gases Evolved in the Thermal Decomposition of Potassium Cobalt Hexacyanoferrate(II). *Thermochim. Acta* **1995**, *265*, 25-30.
2. Mimura, H.; Saito, M.; Akiba, K.; Onodera, Y., Selective Uptake of Cesium by Ammonium Molybdophosphate (AMP)-Calcium Alginate Composites. *J. Nucl. Sci. Technol.* **2001**, *38* (10), 872-878.
3. Endo, Y.; Wu, Y.; Mimura, H.; Niibori, Y.; Ozawa, M., Selective Uptake of Cesium Ions on AMP-loaded Silica Gels. *J. Ion Exch.* **2007**, *18*, 444-449.
4. Doležal, J.; Stejskal, J.; Tympl, M.; Kouřim, V., Improved Inorganic Ion-Exchangers. *J. Radioanal. Nucl. Chem.* **1974**, *21* (2), 381-387.
5. Tranter, T. J.; Herbst, R. S.; Todd, T. A.; Olson, A. L.; Eldredge, H. B., Evaluation of Ammonium Molybdophosphate-Polyacrylonitrile (AMP-PAN) as a Cesium Selective Sorbent for the Removal of <sup>137</sup>Cs from Acidic Nuclear Waste Solutions. *Adv. Environ. Res.* **2002**, *6* (2), 107-121.
6. Satyanarayana, J.; Murthy, G. S.; Sasidhar, P., Adsorption Studies of Cesium on a New Inorganic Exchanger Ammonium Molybdophosphate-Alumina (AMP-Al<sub>2</sub>O<sub>3</sub>). *J. Radioanal. Nucl. Chem.* **1999**, *242* (1), 11-16.
7. Rao, K. L. N.; Shukla, J. P.; Venkataramani, B., Electron Irradiation Studies on Ammonium Molybdophosphate. *J. Radioanal. Nucl. Chem.* **1995**, *189* (1), 107-114.
8. Smit, J. V. R., Ammonium Salts of the Heteropolyacids as Cation Exchangers. *Nature* **1958**, *181* (4622), 1530-1531.
9. Park, Y.; Lee, Y.-C.; Shin, W. S.; Choi, S.-J., Removal of Cobalt, Strontium and Cesium from Radioactive Laundry Wastewater by Ammonium Molybdophosphate-Polyacrylonitrile (AMP-PAN). *Chem. Eng. J.* **2010**, *162* (2), 685-695.
10. Todd, T. A.; Mann, N. R.; Tranter, T. J.; Šebesta, F.; John, J.; Motl, A., Cesium Sorption from Concentrated Acidic Tank Wastes Using Ammonium Molybdophosphate-Polyacrylonitrile Composite sorbents. *J. Radioanal. Nucl. Chem.* **2002**, *254* (1), 47-52.

11. Bird, R. B.; Stewart, W. E.; Lightfoot, E. N., *Transport Phenomena, 2nd ed.* 2nd ed. ed.; Wiley: New York, 2002.
12. Kozeny, J., Ueber kapillare leitung des wassers im boden. *Sitzungsber. Akad. Wiss. Wien* **1927**, *136*, 271-306.
13. Henley, E. J.; Seader, J. D.; Roper, D. K., *Separation Process Principles 3rd ed. International Student Version.* Wiley: New York, 2011.
14. Ruthven, D. M., *Principles of Adsorption and Adsorption Processes.* Wiley: New York, 1984.
15. Hawthorn, R. D. Afterburner Catalysts-Effects of Heat and Mass Transfer between Gas and Catalyst Surface *AIChE Symp. Ser.* **1974**, *70*, 428-438.
16. Patton, A.; Crittenden, B. D.; Perera, S. P., Use of the Linear Driving Force Approximation to Guide the Design of Monolithic Adsorbents. *Chem. Eng. Res. Des.* **2004**, *82* (8), 999-1009.
17. Friedman, A. M.; Kennedy, J. W., The Self-diffusion Coefficients of Potassium, Cesium, Iodide and Chloride Ions in Aqueous Solutions I. *J. Am. Chem. Soc.* **1955**, *77* (17), 4499-4501.
18. Williamson, J. E.; Bazaire, K. E.; Geankoplis, C. J., Liquid-Phase Mass Transfer at Low Reynolds Numbers. *Ind. Eng. Chem. Fundam.* **1963**, *2* (2), 126-129.
19. Sing, K. S. W., Reporting Physisorption Data for Gas/Solid Systems with Special Reference to the Determination of Surface Area and Porosity (Recommendations 1984). *Pure Appl. Chem.* **1985**, *57* (4), 603-619.
20. Sydorhuk, V.; Khalameida, S.; Skubiszewska-Zięba, J.; Leboda, R., Synthesis and Structure of AMP/Oxide Support. *J. Therm. Anal. Calorim.* **2011**, *103* (1), 257-265.
21. Bridgeman, A. J., Density Functional Study of the Vibrational Frequencies of  $\alpha$ -Keggin Heteropolyanions. *Chem. Phys.* **2003**, *287* (1-2), 55-69.
22. Popa, A.; Sasca, V.; Holclajtner-Antunović, I., The Influence of Surface Coverage on Textural, Structural and Catalytic Properties of Cesium Salts of 12-Molybdophosphoric Acid Supported on SBA-15 Mesoporous Silica. *Microporous Mesoporous Mater.* **2012**, *156*, 127-137.

# ***Chapter 5***

## ***Separation of Cesium Ion in Flow Systems Using Resorcinol-Formaldehyde Cryogels with a Microhoneycomb Structure***

### **5.1. Introduction**

In previous chapter, inorganic ion exchangers supported monolithic microhoneycombs were studied to remove  $\text{Cs}^+$  from its aqueous solution. Although these ion exchangers show high performance for  $\text{Cs}^+$  separation in the presence of other alkali metal cations, they easily decompose in high pH solutions.<sup>1, 2</sup> The decomposition problem can be avoided by neutralization of the high pH solution by a strong acid; however, such pre-treatment should be avoided as far as possible. The problem of  $\text{Cs}^+$  removal from high pH solutions may be encountered in the Fukushima Daiichi Nuclear Power Plant case. Huge amounts of burnable wastes containing radioactive cesium, such as agricultural wastes, were produced; these were incinerated in order to reduce their volume and enable their storage. Because the space available to store such nuclear waste is limited in Japan, the waste volume needs to be reduced further. One way to reduce the volume of the incineration ashes is the removal of  $\text{Cs}^+$  by adsorption from the solution obtained by simple washing of the ash. However, such ashes normally contain concentrated alkali metals and the obtained wash water shows high pH values (e.g., pH 10.5-12.9, as reported by the National Institute for Environmental Studies<sup>3</sup>). In such cases,  $\text{Cs}^+$  adsorbents that are stable in high-pH solutions are preferable.

In this chapter, resorcinol-formaldehyde (RF) gels having a microhoneycomb structure (RFMH), which are known to be ion exchangers that can be used in high pH solutions,<sup>4-8</sup> were applied to  $\text{Cs}^+$  separation. We discuss the preparation of RFMH and its  $\text{Cs}^+$  adsorption properties in high pH solutions in flow systems. The effect of preparation conditions of RFMHs are also evaluated to realize effective  $\text{Cs}^+$  separation.

## 5.2. Materials and Methods

### 5.2.1. Materials

Resorcinol, formaldehyde solution, sodium carbonate, 2-methyl-2-propanol (*tert*-butyl alcohol, TBA) and phenol cesium chloride (CsCl), nitric acid (HNO<sub>3</sub>, 1 mol·L<sup>-1</sup> aqueous solution) and cesium standard solution (CsCl, 1000 ppm) were purchased from Wako Pure Chemical Industries. All reagents were used as received.

### 5.2.2. Preparation of the RFMHs

The RFMHs were prepared according to a previous report.<sup>9</sup> Resorcinol (R) was dissolved in deionized-water (W), and sodium carbonate (C) was added to the mixture. After a transparent mixture was obtained, formaldehyde (F) was added to the mixture. The molar ratios of the four components (R:F:C:W) were set to 1:2:0.02:61 (*R/C* 50) and 1:2:0.005:61 (*R/C* 200). The obtained mixture was poured into a PP tube (125 mm × 13 mm i.d.) and maintained at 303 K until gelation. The resulting RF hydrogel was released from the glass tube and washed with deionized water for 1 h to remove the excess reactants and catalyst. Then, the hydrogel was reinserted into a polypropylene tube (125 mm × 13 mm i.d.) and unidirectionally dipped into a liquid nitrogen bath (77 K) at a constant rate (60 mm·h<sup>-1</sup>). After the tube was completely frozen, the frozen hydrogel was released from the tube, thawed at room temperature, and cut into portions of several centimeters. The obtained hydrogel was immersed in 1 mol·L<sup>-1</sup> hydrochloric acid (HCl) for 4 days to allow aging, and then washed with an excess amount of deionized water to completely remove HCl. After washing, the hydrogel was immersed in *tert*-butyl alcohol (TBA) for 2 days to replace the water in it with the alcohol. TBA was exchanged three times during this treatment. Then, the obtained gel was freeze-dried at 263 K for 2 days. The obtained monolith was named as RFMH-(*R/C*).

### 5.2.3. Characterization of the RFMHs

The morphology of the samples was observed using a scanning electron microscope (SEM). The porous properties of the samples were evaluated by nitrogen adsorption experiments. First, the

nitrogen adsorption isotherms of the samples were measured at 77 K. Next, the Brunauer-Emmett-Teller surface areas ( $S_{\text{BET}}$ ) of the samples were calculated from the obtained isotherms.

#### 5.2.4. Cs<sup>+</sup> Separation Experiments Using RFMHs in Batch Systems

The cesium adsorption capacity of the samples was evaluated by measuring their cesium adsorption isotherms. Experiments were conducted at 298 K using solutions containing cesium chloride with a specified pH. The pH was adjusted by adding sodium hydroxide solution. The solutions containing the samples were shaken for 7 days before determining the cesium uptake. The uptake ( $q$ ) was calculated using the following equation (Eq. (5.1)):

$$q = (C_0 - C_e) \frac{V}{m} \quad (5.1)$$

where  $C_0$  and  $C_e$  are the initial and equilibrium cesium concentrations in the solutions, respectively;  $V$  is the volume of the solution; and  $m$  is the weight of the sample.

#### 5.2.5. Cs<sup>+</sup> Separation Experiments Using RFMHs in Flow Systems

The performance of the samples in flow systems was then evaluated. The hydraulic resistance caused by the samples was evaluated by measuring the pressure drop across the hydrogel samples when water was passed through them. The diameter and length of the samples used in this experiment were 9.4 mm and 13 mm, respectively. Finally, the performance of the samples as cesium adsorbents was checked in a flow system. First, 1 mmol·L<sup>-1</sup> nitric acid containing cesium carbonate, with a Cs<sup>+</sup> concentration of 100 ppm ( $C_f$ ), was prepared. The prepared solution was passed through the samples at a flow rate of 1 mL·min<sup>-1</sup>, and the Cs<sup>+</sup> concentration at the outlet of the samples ( $C$ ) was monitored periodically by ion chromatography. The ratio of  $C$  to  $C_f$  ( $C \cdot C_f^{-1}$ ) was plotted against the effluent volume. The diameter and length of the samples used in this experiment were 10 mm and 20 mm, respectively. Figure 5.1 shows the schematic of the experimental apparatus used for the measurement of pressure drop and evaluation of adsorption performance in the flow systems.

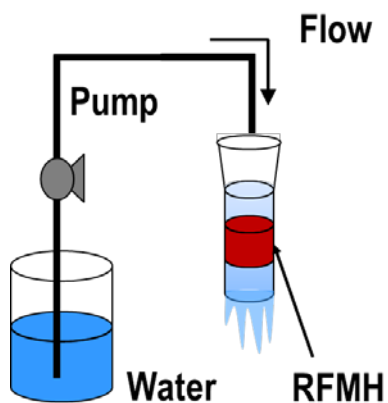


**Fig. 5.1** Schematic of the experimental apparatus for flow systems.

### 5.3. Results and Discussion

#### 5.3.1. Characterization of the RFMHs

Figure 5.2 shows the photograph and SEM image of the obtained RFMH (*R/C 200*). The results showed that the straight channel measured 80-100  $\mu\text{m}$  in diameter and  $\sim 10 \mu\text{m}$  in thickness, indicating that a lower hydraulic resistance and fast mass transfer can be committable, as seen in the other microhoneycomb monoliths.

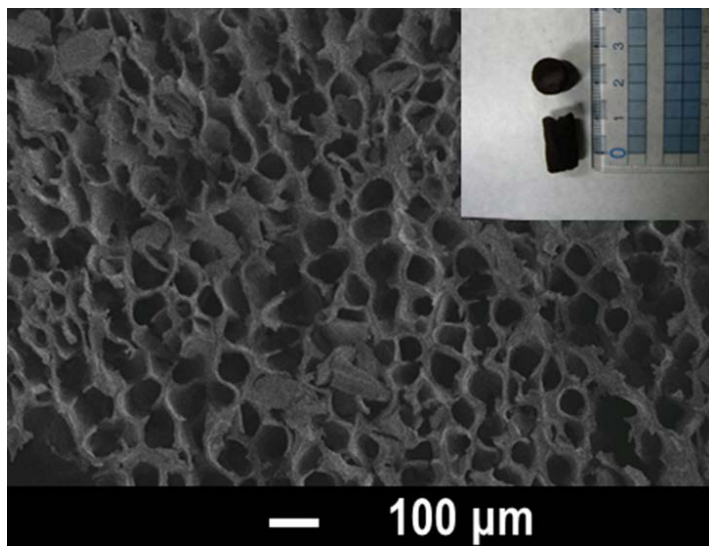


**Fig. 5.2** SEM images of RFMH (*R/C 200*) treated with  $\text{HNO}_3$ .

### 5.3.2. Cs<sup>+</sup> Separation Experiments Using RFMHs in Batch Systems

To evaluate the effect of  $R/C$  on the Cs<sup>+</sup> uptake, adsorption experiments were conducted using RFMH-50 and -200. The Cs<sup>+</sup> uptakes of RFMH-50 and -200 reached a constant value in less than 1 h; however, the uptake of RFMH-200 continuously decreased for 24 h (Figure 5.3). The color of the slurry containing RFMH-200 became partially orange, indicating that RF dissolved in the solution. As previously reported,<sup>8,9</sup> RF slowly decomposed in the basic solution because of oxidative decomposition of the polymer structure, and the Cs<sup>+</sup> selectivity was reduced. RF with high  $R/C$  composes with larger 1<sup>st</sup> particles when compared with one of the smaller  $R/C$ . The larger RF particles easily decomposed compared with the smaller ones because of the weaker polymer network (Scheme 5.1).

Next, the effect of pretreatment by HNO<sub>3</sub> was evaluated. The Cs<sup>+</sup> uptake of RFMH-50 that was not treated by HNO<sub>3</sub> was about half of that of the HNO<sub>3</sub> treated sample, and the uptake capacity decreased with increasing contact time (Figure 5.4). This result can also be explained by the strength of the polymer network. When treated with HNO<sub>3</sub>, polymerization occurs between the unreacted polymer chains, and the polymer network becomes stronger. Therefore, decomposition of the polymer network does not occur.

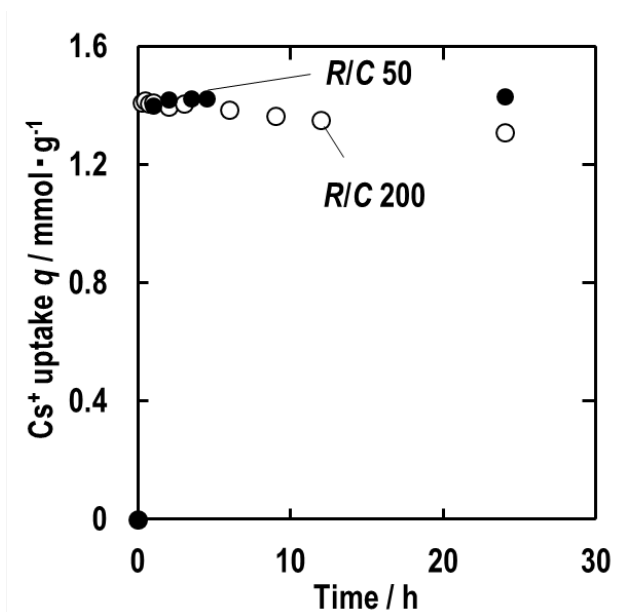


**Fig. 5.3** Cs<sup>+</sup> uptakes of RFMH at R/C 50 (black circles) and 200 (white circles) at 298 K, at an initial pH of 11.9.

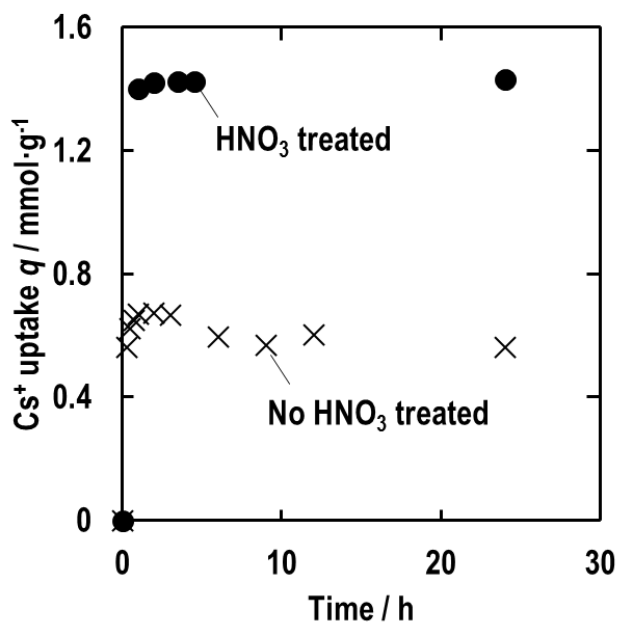
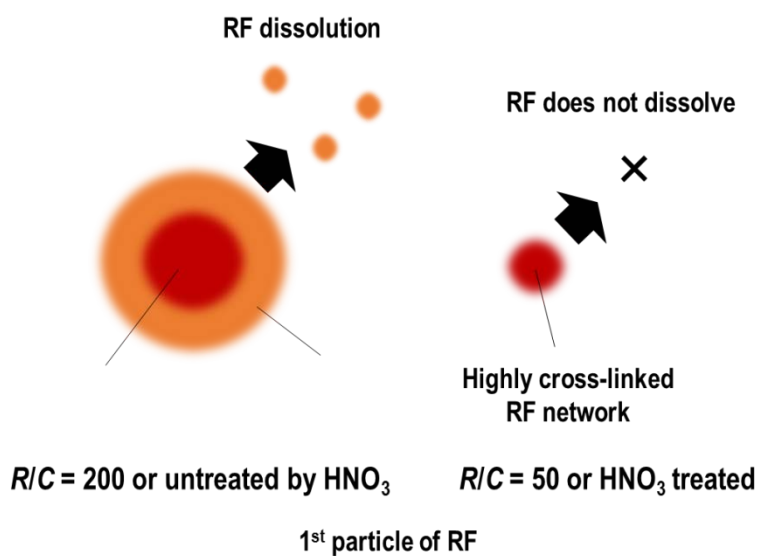


**Fig. 5.4** Cs<sup>+</sup> uptakes of HNO<sub>3</sub> treated RFMH at *R/C* 50 at 298 K at an initial pH of 11.9. HNO<sub>3</sub> treated samples are represented by black circles, and non-treated samples, by black crosses.



**Scheme 5.1** Schematic illustration of polymer network of RF 1<sup>st</sup> particles.

To evaluate the effect of pH on the Cs<sup>+</sup> adsorption capacity of RFMH-50, adsorption experiments were conducted at 298 K using Cs<sup>+</sup> aqueous solutions with pH values ranging from 6.1 to 12.8. The Cs<sup>+</sup> uptake curves at various pH values are shown in Figure 5.5. The Cs<sup>+</sup> uptake reached equilibrium within 1 h for each pH; on the other hand, the Cs<sup>+</sup> uptake amount are dramatically difference. The pKa

values of resorcinol, the monomer of RF, are 9.2 and 11.3; therefore, the proton in the hydroxy group of RF can act as ion exchangeable site when the pH is higher than these pKa values.<sup>1</sup> The pH vs. uptake plot shows that the Cs<sup>+</sup> uptake increases with increasing pH from 6.1 to 11.8, indicating that the first proton reacts with Cs<sup>+</sup> at pH 10.8 and the second proton further reacts with Cs<sup>+</sup> at pH 11.9. The Cs<sup>+</sup> uptake at pH 11.9 (= 1.4 mmol·g<sup>-1</sup>) was 2.3 times of that at pH 10.8 (= 0.6 mmol·g<sup>-1</sup>), which also supported the relationship between pKa and pH. On the other hand, the Cs<sup>+</sup> uptake dramatically decreased at pH 12.8 and the obtained slurry became orange. This result indicates that the RFMH dissolved in the solution of pH 12.8 and the Cs<sup>+</sup> selectively reduced due to this dissolution. Considering the effect of pH on Cs<sup>+</sup> uptake, the pH was adjusted to 10.8 for further experiments.

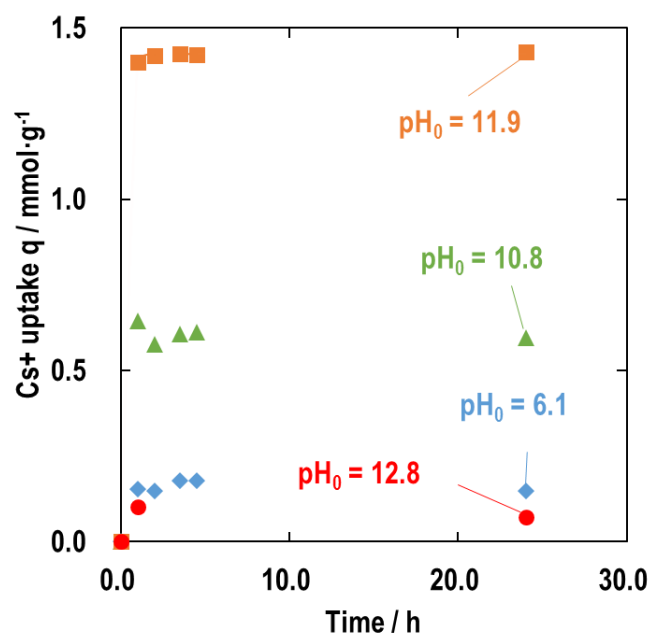


**Fig. 5.5** Cs<sup>+</sup> uptakes of RFMH at 298 K at initial pH values of 6.1 (blue diamond), 10.8 (green triangle), 11.9 (orange square), and 12.8 (red circle).

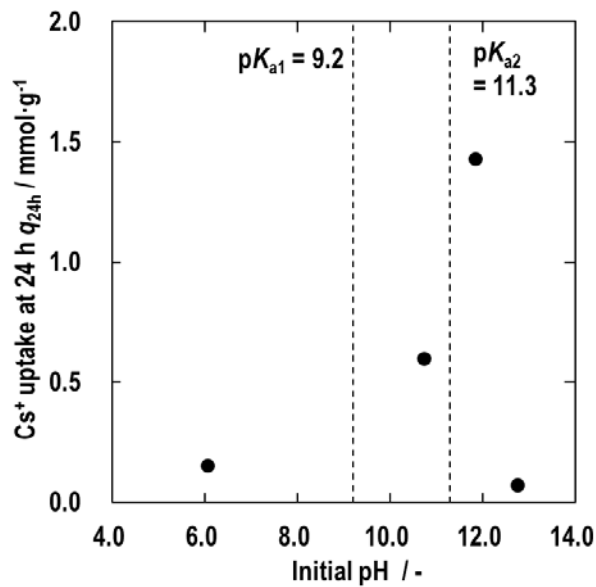


Fig. 5.6 Cs<sup>+</sup> adsorption capacity of RFMH at 24 h vs. the initial pH at 298 K.

To evaluate the Cs<sup>+</sup> adsorption equilibrium, adsorption isotherms at 298 K were prepared at a pH 11.9. The obtained isotherm was well represented by the Langmuir isotherm, which is often seen when the adsorption mechanism involves ion exchange. The maximum Cs<sup>+</sup> uptake calculated from the Langmuir model was 2.5 mmol·g<sup>-1</sup>, which was close to the reported values.

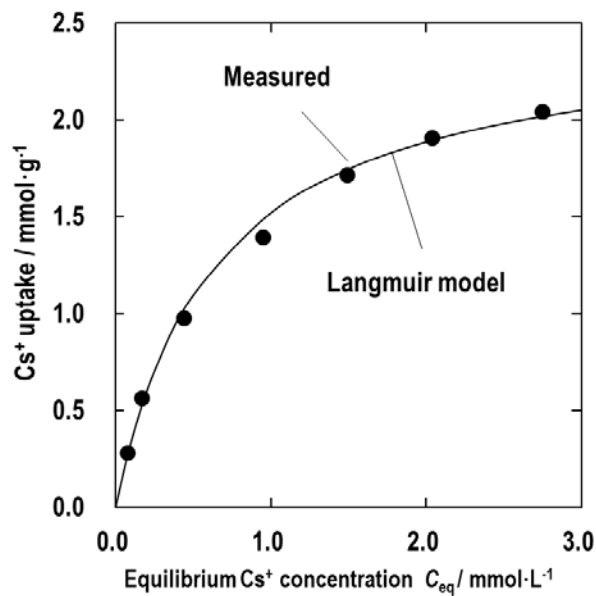
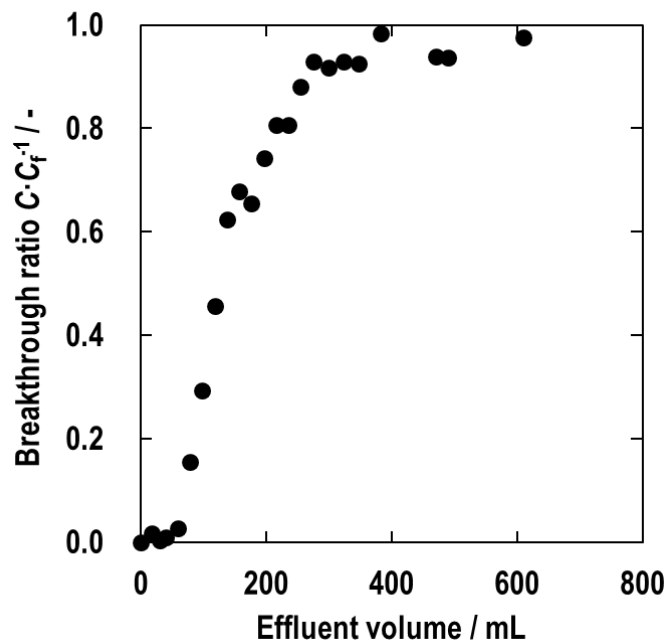


Fig. 5.7 Cs<sup>+</sup> adsorption isotherm at initial pH value 11.9 at 298 K.

### 5.3.3. Cs<sup>+</sup> Separation Experiments Using RFMHs in Flow Systems

To evaluate the applicability of RFMH for Cs<sup>+</sup> adsorption in flow systems, breakthrough experiments were conducted. The obtained Cs<sup>+</sup> breakthrough curve was sigmoidal and the adsorption capacity was 1.2 mmol·g<sup>-1</sup>. The capacity calculated from the ion exchange isotherm was 1.9 mmol·g<sup>-1</sup>, indicating that about 63 % of the capacity can be used in flow systems. The length of unused bed (LUB) was ~12 mm and length based column utilization (1-L/LUB) was 0.14. Because of the mass transfer resistance of the resin, the column length basis utilizations were comparatively lower than that of PBAs-SAMHs and AMP-SMH mentioned previous chapter. However, they are not stable and quickly decomposed in high-pH solutions. Therefore, RFMH is expected to show a high potential for use in Cs<sup>+</sup> separation from highly alkaline solutions.



**Fig. 5.8** Cs<sup>+</sup> breakthrough curve of RFMH. at initial pH at 298 K. Conditions: superficial velocity  $u_s = 14 \text{ mm} \cdot \text{min}^{-1}$ , feed concentration  $C_f = 300 \text{ ppm}$ ,  $L = 13 \text{ mm}$ .

## 5.4. Conclusion

In this work, the Cs<sup>+</sup> separation performance of monolithic resorcinol formaldehyde resin with a microhoneycomb structure (RFMH) was evaluated. The effects of  $R/C$  and  $\text{HNO}_3$  treatment of RFMH

were evaluated, and the obtained results suggested that RFMH with a highly cross-linked polymer network showed high Cs<sup>+</sup> adsorption capacity and stability in highly alkaline conditions. The batch adsorption experiments performed in solution with pH ranging from 6.1 to 12.8 showed that the Cs<sup>+</sup> uptake capacity dramatically increased with increasing pH from 6.1 to 11.9 but decreased sharply at pH ~12.8. This result indicated that ion exchangeable sites dissociated in the solutions with pH higher than pK<sub>a2</sub> (11.3); however, the RF polymer also dissolved in the highly alkaline solution. The Cs<sup>+</sup> breakthrough experiment results indicated that length basis column utilization of RFMH was lower than that of AMP-SMH because of the comparatively slower mass transfer. However, considering that AMP and SMH dissolve quickly in high-pH solutions, RFMH has a great potential for use in the separation of Cs<sup>+</sup> from highly alkaline solutions, such as those produced in the Fukushima case.

## 5.5. Reference

1. Zhu, Z.; Tain, R.; Rhodes, C., A Study of the Decomposition Behaviour of 12-Tungstophosphate Heteropolyacid in Solution. *Can. J. Chem.* **2003**, *81* (10), 1044-1050.
2. Takahashi, A.; Kitajima, A.; Parajuli, D.; Hakuta, Y.; Tanaka, H.; Ohkoshi, S.; Kawamoto, T., Radioactive Cesium Removal from Ash-Washing Solution with high pH and high K<sup>+</sup>-Concentration Using Potassium Zinc Hexacyanoferrate. *Chem. Eng. Res. Des.* **2016**, *109*, 513-518.
3. National Institute for Environmental Studies, Japan, Technical report. 2014.
4. Bray, L. A.; Elovich, R. J.; Carson, K. J. Cesium Recovery Using Savannah River Laboratory Resorcinol-Formaldehyde Ion Exchange Resin; Pacific Northwest Laboratory, Richland, WA, 1990.
5. Hubler, T. L.; Franz, J. A.; Shaw, W. J.; Bryan, S. A.; Hallen, R. T.; Brown, G. N.; Bray, L. A.; Linehan, J. C. Synthesis, Structural Characterization, and Performance Evaluation of Resorcinol-Formaldehyde (R-F) Ion-Exchange Resin; Pacific Northwest Laboratory, Richland, WA, 1995.
6. Kurath, D. E.; Bray, L. A.; Brooks, K. P.; Brown, G. N.; Bryan, S. A.; Carlson, C. D.; Carson, K. J.; DesChane, J. R.; Elovich, R. J.; Kim, A. Y. Experimental Data and Analysis to Support the Design of an Ion-Exchange Process for the Treatment of Hanford Tank Waste Supernatant Liquids; Pacific Northwest Laboratory, Richland, WA, 1994.
7. Samanta, S. K.; Theyyuni, T. K.; Misra, B. M., Column Behaviour of Resorcinol-Formaldehyde Polycondensate Resin for Radiocesium Removal from Simulated Radwaste Solution. *J. Nucl. Sci. Technol.* **1995**, *32* (5), 425-429.
8. Banerjee, D.; Rao, M. A.; Gabriel, J.; Samanta, S. K., Recovery of Purified Radiocesium from Acidic Solution Using Ammonium Molybdophosphate and Resorcinol Formaldehyde Polycondensate

resin. *Desalination* **2008**, 232 (1–3), 172-180.

9. Nishihara, H.; Mukai, S. R.; Tamon, H., Preparation of Resorcinol-Formaldehyde Carbon Cryogel Microhoneycombs. *Carbon* **2004**, 42 (4), 899-901.

10. Egorin, A. M.; Tutov, M. V.; Didenko, N. A.; Slobodyuk, A. B.; Marinin, D. V.; Avramenko, V. A., Effect of Parameters of Thermal Treatment of Resorcinol-Formaldehyde Resins on Their Chemical Stability and  $^{137}\text{Cs}$  Uptake Efficiency. *J. Radioanal. Nucl. Chem.* **2015**, 304 (1), 281-286.

11. Egorin, A. M.; Tutov, M. V.; Slobodyuk, A. B.; Avramenko, V. A., Stability of Resorcinol-Formaldehyde Resins in Alkaline Solutions. *Radiochemistry* **2014**, 56 (2), 183-188.



## *Part 3*

# *Application of Microhoneycombs for Carbon Dioxide Absorption by Supported Ionic Liquid Phases*



# ***Chapter 6***

## ***Absorption of Carbon Dioxide in Flow Systems Using Silica Microhoneycombs Loaded with an Ionic Liquid***

### **6.1. Introduction**

Carbon dioxide (CO<sub>2</sub>) is one of the most serious gases which contribute to greenhouse effect. CO<sub>2</sub> concentration in the atmosphere continuously increased from 315 to 385 ppmv in the past half century (A.D. 1958-2008, Hawaii).<sup>1</sup> The most critical CO<sub>2</sub> source is in energy-related fields where 67 % CO<sub>2</sub> is emitted from fossil-fuel combustion.<sup>2</sup> Therefore, CO<sub>2</sub> removal from combustion gas is important to inhibit CO<sub>2</sub> emission to the atmosphere. Various separation techniques have been studied to remove CO<sub>2</sub> from combustion gas (e.g. adsorption, absorption and the others).<sup>3-5</sup> Among them, CO<sub>2</sub> absorption using alkanolamine solutions has been most widely used in large-scale processes.<sup>6</sup> However, high energy consumption to regenerate the solutions, loss of alkanolamine during regeneration and corrosion of equipment by the solutions have led to active research to seek an alternative method.

CO<sub>2</sub> separation using ionic liquids (ILs) has been extensively studied because ILs have a high thermal stability, low volatility and low partial pressure.<sup>2,7</sup> In addition, the CO<sub>2</sub> separation performance of ILs can be improved by tuning their physical properties through molecular design. ILs designed for special tasks, which are called “task-specific ILs”, have recently attracted attention in various fields including catalysis, separation and analysis.<sup>8</sup> For example, ILs bearing amino groups in anion or/and cation parts have been reported.<sup>9,10</sup> These “amine-functionalized” ILs show high CO<sub>2</sub> absorption capacities at low CO<sub>2</sub> concentrations because CO<sub>2</sub> selectively reacts with the amino groups within them and forms carbonates/carbamates (Fig. 6.1).

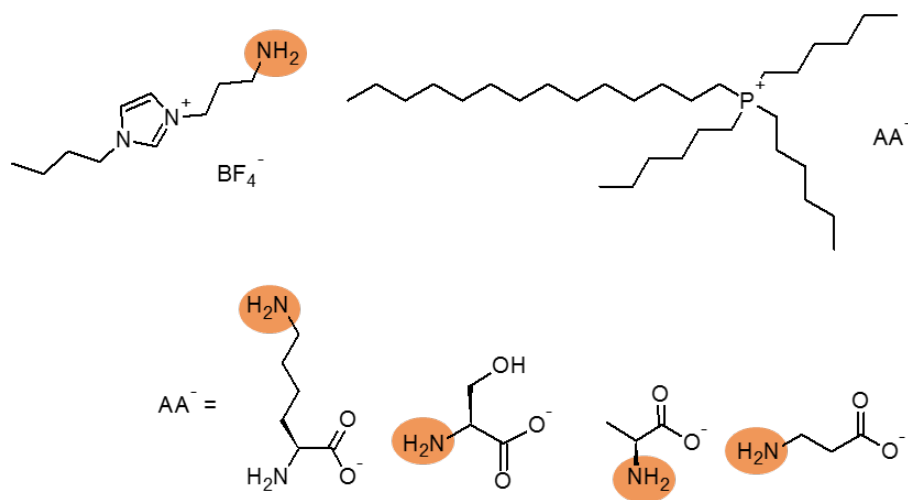
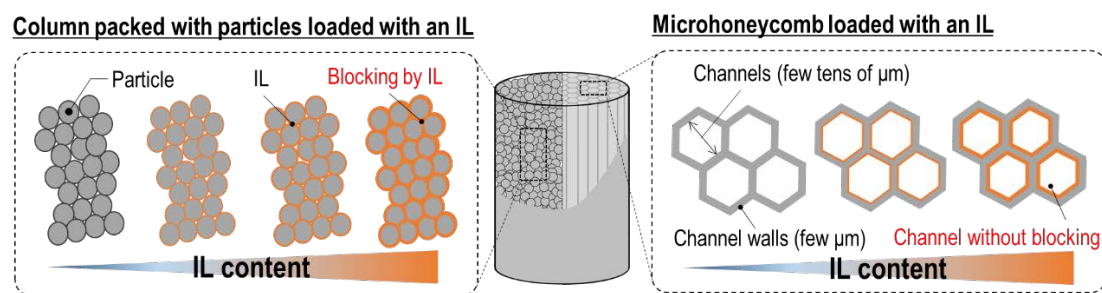


**Fig. 6.1** Example of task-specific ILs used for CO<sub>2</sub> absorption.<sup>10, 11</sup>  
Orange circles represent amino groups

One drawback of ILs to be used for CO<sub>2</sub> separation is their slow CO<sub>2</sub> absorption rate caused by their high viscosity. To improve CO<sub>2</sub> absorption rate, ILs supported on supporting materials, i.e. supported ionic liquid phases (SILPs), have been developed.<sup>11-13</sup> Normally, particles made from organic/inorganic materials have been used as supports for SILPs.<sup>11, 14</sup> In flow processes, SILPs are used as a column packed with their particles. However, clogging of void spaces between the packed particles by ILs occurs at high IL loadings. Such blocking causes a serious hydraulic resistance against a fluid flow (Scheme 6.1, left).

Microhoneycombs have aligned straight channels, a few tens of  $\mu\text{m}$  in diameter, which are formed by thin and porous channel walls, a few  $\mu\text{m}$  in thickness. As materials having this structure cause minimal hydraulic resistance when fluids flow through them, and they can be used as new monolithic adsorbents and catalysts for flow systems. Such unique structures can be easily synthesized using ice crystals as the template for their channels (ice-templating method).<sup>15</sup> Because microhoneycombs have straight macrochannels, it can be expected that void blocking by ILs hardly occurs when they are used as the support, even at high loadings.



**Scheme 6.1** Schematic illustration of ILs supported on a packed column (left) and a microhoneycomb (right)

## 6.2. Materials and Methods

### 6.2.1. Materials

Trihexyl(tetradecyl)phosphonium bromide ( $[P_{66614}][Br]$ ,  $\geq 95\%$ ) and silica gel (28-200 mesh, average pore diameter 22 Å) were purchased from Sigma-Aldrich. Sodium silicate solution (55 wt %, molar ratio ( $SiO_2/Na_2O$ ) = 2.1), 2-methyl-2-propanol (*tert*-butyl alcohol, TBA), (99.0 %), methanol (99.8 %) and ethanol (99.5 %) were purchased from Wako Pure Chemical Industries, Ltd, Japan. L-alanine (99.0 %) was purchased from Tokyo Chemical Industry Co., Ltd., Japan. All reagents were used as received.

### 6.2.2. Preparation of SMHs

Silica microhoneycombs (SMHs) were prepared according to a previous report.<sup>15</sup> A sodium silicate solution (silica glass) was diluted with a double deionized water to adjust its  $SiO_2$  concentration to 1.9 mol- $SiO_2 \cdot L^{-1}$ . Sodium ions in the solution were exchanged to protons by using a cation-ion exchange resin (2.0 eq to sodium ions, Amberlite® IR120B H AG, Organo Corporation, Japan). The obtained silica sol (pH ~ 2.5) was poured into a polypropylene (PP) tube (i.d.; 13 mm, length; 125 mm) and aged in an incubator (ICI-100, AS ONE Corporation, Japan) maintained at 303 K. After gelation, the obtained gel was aged in the same incubator. After the aging process, the PP tube including the silica gel was unidirectionally dipped into a liquid nitrogen ( $N_2$ ) bath (77 K) at a constant rate of 60 mm·h<sup>-1</sup> to grow aligned ice rods within the gel. The frozen gel was thawed and released from the tube. The

gel was soaked in TBA kept at 323 K for 2 days to exchange the water in it to TBA. The TBA was renewed 3 times during this soaking process. The sample was freeze-dried at 263 K for 2 days using a freeze dryer (FDU-2200, Tokyo Rikakikai Co., Ltd., Japan).

### 6.2.3. Preparation of Ionic Liquid ([P<sub>66614</sub>][Ala])

[P<sub>66614</sub>][Ala] was prepared according to Goodrich's procedure.<sup>10</sup> Briefly, 10 mmol (5.64 g) of [P<sub>66614</sub>][Br] was diluted with 30 mL of methanol, and an anion exchange resin (DOWEX™ SBR-P C OH, Wako Pure Chemical Industries, Ltd., Japan) was added to the solution to replace the Br anions (Br<sup>-</sup>) in [P<sub>66614</sub>][Br] with hydroxide ions (OH<sup>-</sup>). Then, 11 mmol (0.980 g) of L-alanine was added to the solution to replace OH<sup>-</sup> with alanate. Methanol in the solution was removed by evaporation at 323 K. Excess L-alanine was removed by recrystallization using cold acetonitrile at 273 K and the remaining alanine was separated by vacuum filtration. Acetonitrile was removed by evaporation at 313 K.

### 6.2.4. Preparation of Silica Microhoneycombs Loaded with [P<sub>66614</sub>][Ala] (IL-SMHs)

IL-SMHs were prepared by impregnating SMHs with an ethanol solution containing [P<sub>66614</sub>][Ala]. A 5 mL ethanol solution containing [P<sub>66614</sub>][Ala] at a specified amount was prepared and applied to the prepared SMH. The volume of the applied was adjusted to be the same as the total pore volume of the SMH. Then, the monolith was heated at 363 K for 5 min to evaporate the ethanol in it. The dried monolith was turned upside down, and was impregnated with the solution again. This impregnation/drying cycle was repeated until all of the solution was consumed, and then finally, the monolith was vacuum-dried at 363 K for half a day. The obtained sample was designated as IL-SMH-*x*, where *x* represents the [P<sub>66614</sub>][Ala] content in wt % ((g-[P<sub>66614</sub>][Ala])·(g-[P<sub>66614</sub>][Ala]-SMH-*x*)<sup>-1</sup>).

### 6.2.5. Preparation of Silica Gel Particles Loaded with [P<sub>66614</sub>][Ala] (IL-SPs)

Silica gel particles were stirred for 30 min in 10 mL of ethanol containing a specified amount of

[P<sub>66614</sub>][Ala]. The ethanol was removed by evacuation at 323 K, and then the particles were dried at 363 K in an oven for half a day. The obtained sample will be denoted as IL-SP-*x* hereafter, where *x* represents the [P<sub>66614</sub>][Ala] content in wt % ((g-[P<sub>66614</sub>][Ala])·(g-[P<sub>66614</sub>][Ala]-SP-*x*)<sup>-1</sup>).

### 6.2.6. Characterization

The morphology of the obtained samples was characterized using a scanning electron microscope (SEM, SU1510, Hitachi High-Technologies Corporation). FT-IR spectra were recorded on a Fourier transition infrared (FT-IR) spectrometer (FT/IR-6100, JASCO Corporation, Japan) operating in a transmission mode under vacuum. The [P<sub>66614</sub>][Ala] content was measured using a thermogravimetric (TG) analyzer (TGA-50, Shimadzu Corporation, Japan). Porous properties of the samples were characterized using a N<sub>2</sub> adsorption/desorption apparatus (77 K, BELSORP-mini, Microtrac BEL). Micro/mesopore volumes of SMH and SP were determined through Grand Canonical Monte Carlo method (GCMC) analysis.<sup>16</sup>

### 6.2.7. Evaluation of the Hydraulic Resistance of IL-SMHs and a Column Packed with IL-SPs

The pressure drop which occurs when helium (He) gas was passed through IL-SMHs was measured to evaluate the hydraulic resistance the samples cause. A monolithic sample (diameter, ~ 10 mm; length, ~ 20 mm) was fixed in a heat shrinkable tube and both ends of the tube were connected to stainless steel (SUS) tubes. He gas was fed to the monolith at a constant flow rate (0 to 100 mL·min<sup>-1</sup>) and the pressure drop which occurs was measured using a pressure sensor (PA-853, Copal Electronics, Japan). The measured pressure drop was analyzed using the Hagen-Poiseuille equation (6.1).

$$\frac{\Delta P}{L} = \frac{32\mu u_i}{d^2} \quad (6.1)$$

Here,  $\Delta P$ ,  $\mu$ ,  $u_i$ ,  $L$  and  $d$  represent the pressure drop in Pa, the viscosity of He gas, the interstitial velocity in, the monolith length and the hydrodynamic channel diameter, respectively. The interstitial

velocity was calculated from the superficial velocity ( $u_s$ ) and the cross-sectional void fraction of the honeycomb ( $u_i = u_s/\varepsilon$ ,  $\varepsilon \sim 0.85$ ).

The pressure drop a column packed with IL-SPs causes was also measured for comparison. IL-SPs were packed in a SUS column and measurements were conducted using the same method used for monoliths.

### 6.2.8. CO<sub>2</sub> Separation Experiments in a Batch System

The CO<sub>2</sub> uptake ability of the obtained samples was evaluated by TG analysis. A monolith (diameter,  $\sim 5$  mm; height,  $\sim 10$  mm) was set in a cage-type Pt cell (i.d. 8.5 mm, height, 9.5 mm). The cell was loaded in TG analysis system, and the sample in it was pretreated at 393 K under a N<sub>2</sub> flow (40 mL·min<sup>-1</sup>) for 1 h. The sample was cooled to 303 K and then N<sub>2</sub> including a specified concentration of CO<sub>2</sub> was passed over the sample to let it absorb CO<sub>2</sub>. The partial pressure of CO<sub>2</sub> was varied from 5 to 70 kPa to obtain sorption isotherms. Experiments using IL (10 mg) loaded in a pan-type Pt cell (i.d., 6.0 mm; height, 2.5 mm) were also conducted. The obtained isotherms were analyzed using the Langmuir model (6.2).

$$q = \frac{q_L K_L p}{1 + K_L p} \quad (6.2)$$

Here,  $q$ ,  $q_L$ ,  $K_L$  and  $p$ , respectively represent the CO<sub>2</sub> uptake, the maximum CO<sub>2</sub> capacity, the Langmuir constant, and the CO<sub>2</sub> partial pressure.

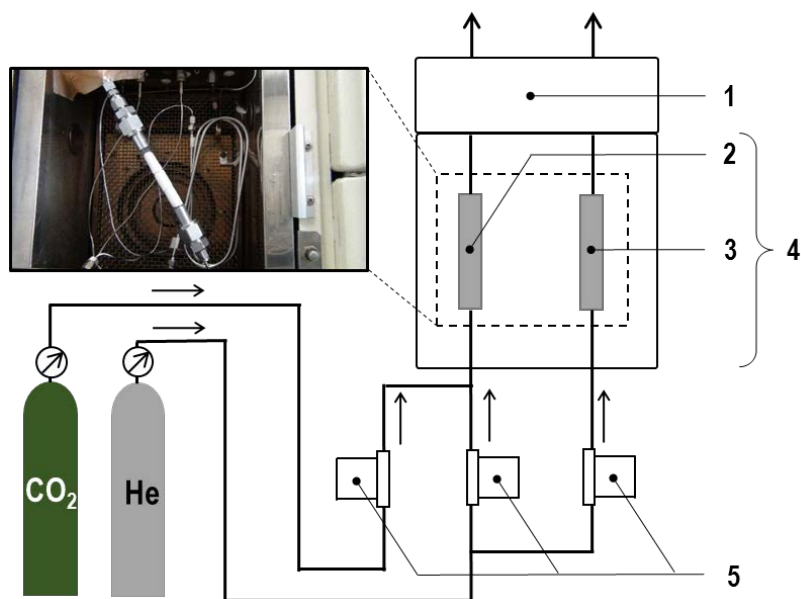


**Fig. 6.2** The experimental setup for CO<sub>2</sub> separation experiments using a flow system. (1) TCD detector; (2) a monolithic sample fixed in a heat shrinkable tube; (3) control; (4) GC oven; (5) mass flow controller.

### 6.2.9. CO<sub>2</sub> Separation Experiments in Flow Systems

CO<sub>2</sub> separation experiments were also conducted using a flow system. Three pieces of IL-SMH monoliths (average diameter; 11 mm, total length; 63 mm) fixed in series in a heat-shrinkable tube, were held at a constant temperature at 303 K in a gas chromatography oven (Fig. 6.2). The outlet of the tube was connected to a thermal conductivity detector (TCD). He gas containing 33 mol% CO<sub>2</sub> was passed through the sample at a total flow rate of 9.0 mL·min<sup>-1</sup>, and the CO<sub>2</sub> concentration in the effluent was monitored.

## 6.3. Results and Discussion

### 6.3.1. Synthesis and Characterization of IL-SMHs and IL-SPs

The SMHs prior to [P<sub>66614</sub>][Ala] impregnation were white in color (Fig. 6.3 (a)) and had aligned straight channels, 15-25 micrometer in diameter, which were formed walls, 1-2 micrometer in thickness (Fig. 6.3 (c), (d)). After impregnation, the color of the monolith changed to pale yellow,

indicating [P<sub>66614</sub>][Ala] was supported on it. As expected, [P<sub>66614</sub>][Ala] did not leak from the monolith even where the [P<sub>66614</sub>][Ala] content was increased to 50 wt %. On the other hand, [P<sub>66614</sub>][Ala] could not be supported without leaking on the silica gel particles at contents higher than 44 wt % (Fig. 6.3 (b)).

The FT-IR spectrum (not shown) of the IL-SMH-50 shows peaks corresponding to [P<sub>66614</sub>][Ala] ( $\nu(\text{C-H})$  at 720 cm<sup>-1</sup>,  $\nu(\text{P-C})$  at 1,040-1,500 cm<sup>-1</sup>,  $\nu_{\text{as}}(\text{CO}_2^-)$  at 1,580 cm<sup>-1</sup>,  $\nu(\text{C-H})$  at 2,855, 2,923 and 2,955 cm<sup>-1</sup>, and  $\nu(\text{N-H})$  at 3,300 cm<sup>-1</sup>),<sup>11, 17</sup> in addition to those characteristic of SiO<sub>2</sub> ( $\nu(\text{Si-O})$  at 795 cm<sup>-1</sup>, in-plane stretching vibration of Si-O at 950 cm<sup>-1</sup>,  $\nu_{\text{as}}(\text{Si-O-Si})$  at 1,080 and 1,140 cm<sup>-1</sup>,  $\delta(\text{H}_2\text{O})$  at 1,630 cm<sup>-1</sup> and  $\nu(\text{O-H})$  and  $\nu(\text{Si-OH})$  which hydrogen-bonded water at around 3,400 cm<sup>-1</sup>)<sup>18</sup>, indicating that [P<sub>66614</sub>][Ala] was supported intact.

The TGA data (not shown) of IL-SMH-33 and IL-SMH-50 show large weight losses occurring in the temperature range of 473 K to 1073 K which caused by the decomposition of [P<sub>66614</sub>][Ala]. From the weight losses, the [P<sub>66614</sub>][Ala] contents of IL-SMH-33 and IL-SMH-50 can be estimated 32 wt% and 44 wt%, respectively on a dry-sample basis, consistent with the amounts of [P<sub>66614</sub>][Ala] impregnated during synthesis.

The N<sub>2</sub> adsorption/desorption isotherms of SMHs and silica gel particles are of type-I,<sup>19</sup> indicating that they are microporous. As the approximate molecular sizes of P<sub>66614</sub> cation and alanine are 1.2 nm and 0.6 nm, respectively, according to the literature,<sup>20, 21</sup> [P<sub>66614</sub>][Ala] is assumed to be accommodated in pores with diameters >1.8 nm. SMHs and silica gel particles respectively have micro-mesopore (1.8-50 nm) volumes of 0.016 and 0.070 cm<sup>3</sup>·g<sup>-1</sup> as determined by GCMC analysis. As a [P<sub>66614</sub>][Ala] loading level of 50 wt % corresponds to 0.87 cm<sup>3</sup>·IL·(g-silica)<sup>-1</sup>, the excess volume of [P<sub>66614</sub>][Ala] should reside in the channels of SMH and the void spaces formed between silicagel particles, respectively.

### 6.3.2. Pressure Drop Measurements

To check whether the channels of SMHs are blocked by the impregnated [P<sub>66614</sub>][Ala], pressure drop measurements were conducted and the measured values were compared with the values

calculated by the Hagen-Poiseuille equation for a circular tube with the corresponding average diameter (Fig. 6.4 (a)). As we reported before, monolithic microhoneycombs show nearly the same pressure drop as a bundle of capillaries having the same diameter as the average channel size of them<sup>22</sup>. This was confirmed in the present study as the average diameter of channels of the SMH (20.3  $\mu\text{m}$  in Table 6.1) determined from the pressure drop measurements is consistent with those observed in the SEM images (Fig. 6.3 (c), (d)).

The pressure drop of IL-SMHs slightly increases with the increase in  $[\text{P}_{66614}][\text{Ala}]$  content, which indicates that the hydrodynamic diameter of the channel decreases by incorporating  $[\text{P}_{66614}][\text{Ala}]$ . The increases in pressure drop correspond to decreases in the channel diameter by 0.40  $\mu\text{m}$  and 0.70  $\mu\text{m}$  for IL-SMH-33 and IIL-SMH-50, respectively. On the other hand, the thickness of  $[\text{P}_{66614}][\text{Ala}]$  supported on SMH can be estimated as 0.24  $\mu\text{m}$  and 0.52  $\mu\text{m}$  for IL-SMH-33 and IL-SMH-50, respectively, which was estimated by assuming  $[\text{P}_{66614}][\text{Ala}]$  was uniformly coated on the channel walls and using  $0.9 \text{ cm}^3 \cdot \text{g}^{-1}$  as the density of  $[\text{P}_{66614}][\text{Ala}]$ .<sup>10</sup> This result essentially agrees with the decreases in the channel diameter determined by pressure drop measurements.

Although the pressure drop remains low for all IL-SMH samples, the pressure drop of a column packed with IL-SPs drastically increases as the  $[\text{P}_{66614}][\text{Ala}]$  content was increased to 44 wt % (Fig. 6.4 (b), IL-SP-44). This result indicates that  $[\text{P}_{66614}][\text{Ala}]$  block the voids formed between the particles in the column as schematically shown in the inset of Fig. 6.4. (b). This result indicates that SMHs are more suitable material to support ILs which are to be used in flow systems.

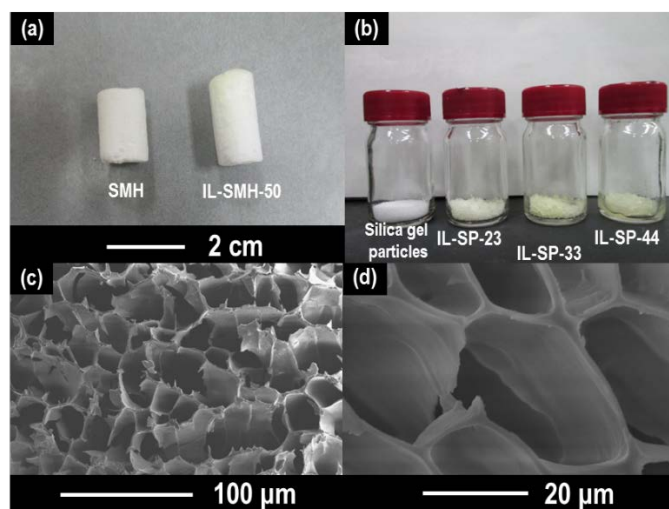


**Fig. 6.3** The obtained samples: (a) photographs of a SMH (left) and an IL-SMH-50 (right), (b) photographs of silica gel particles, IL-SP-23, IL-SP-33 and IL-SP-44 (left to right), (c) a cross-sectional SEM image of a SMH, (d) an enlarged SEM image of a SMH.

**Table 6.1** Calculated thickness of  $[P_{66614}][Ala]$  coated on the channels in SMH using two different methods.

	average size <sup>a</sup> / $\mu\text{m}$	channel	calculated thickness of $[P_{66614}][Ala]/\mu\text{m}$	
			method 1 <sup>b</sup>	method 2 <sup>c</sup>
SMH	20.3	-	-	-
IL-SMH-33	19.5		0.40	0.24
IL-SMH-50	18.9		0.70	0.52

<sup>a</sup> Calculated using the Hagen-Poiseuille equation (eq. (1)), <sup>b</sup> Estimated from difference of average channel size, <sup>c</sup> Estimated from the loading of  $[P_{66614}][Ala]$  and  $N_2$  adsorption data

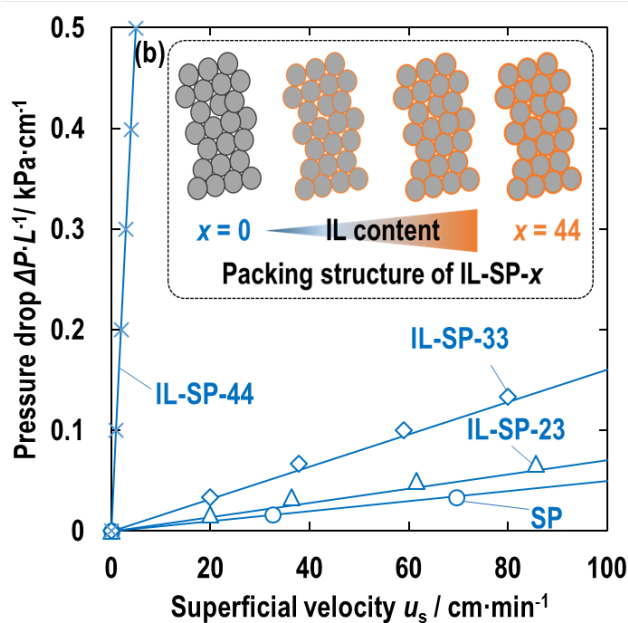
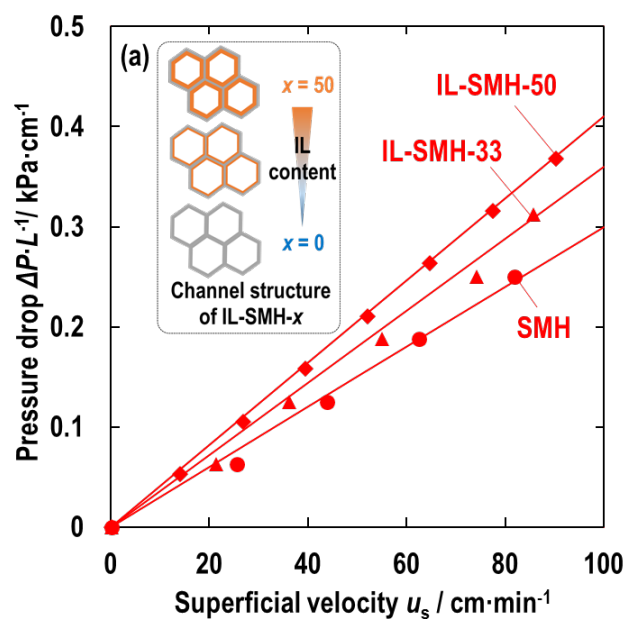


**Fig. 6.4** (a) Pressure drop data of a SMH (solid red circle), an IL-SMH-33 (solid red triangle) and an IL-SMH-50 (solid red diamond). Inset represents a schematic illustration of how IL is coated on channel walls of a SMH. (b) Pressure drop data of columns packed with silica gel particles (open blue circle), IL-SP-23 (open blue triangle), IL-SP-33 (open blue diamond) and IL-SP-44 (blue cross). Inset represents a schematic illustration of how the void spaces between silica gel particles are clogged at high IL loadings.

### 6.3.3. CO<sub>2</sub> Sorption Isotherms on SMH and IL-SMH

To evaluate the equilibrium CO<sub>2</sub> capacity of IL-SMH, sorption isotherms of SMH and IL-SMH were measured (Fig. 6.5). The obtained isotherm of IL-SMH-50 is well represented by the Langmuir model, indicating that CO<sub>2</sub> is chemisorbed to the amino groups in the materials. The CO<sub>2</sub> capacity of IL-SMH-50 at 15 kPa CO<sub>2</sub> was found to be about 0.26 mmol g<sup>-1</sup>, about 4 times higher than that of SMH. High CO<sub>2</sub> capacities at low partial pressures are favorable for the separation of CO<sub>2</sub> from post-combustion gas emitted from fossil-fuel power plants, which typically contains CO<sub>2</sub> at a partial pressure less than 15 kPa<sup>2,3</sup>).

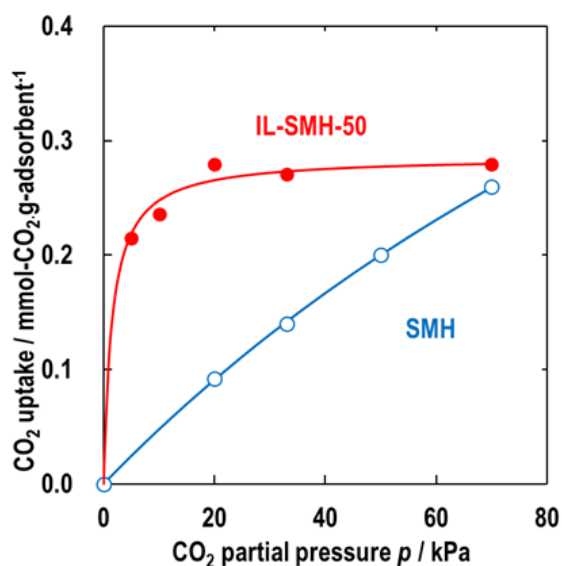


**Fig. 6.5** CO<sub>2</sub> sorption isotherms of IL-SMH-50 (solid red circle) and SMH (open blue circle) at 303 K. The solid lines are fitted using the Langmuir model. Diluent gas: N<sub>2</sub>.

### 6.3.4. CO<sub>2</sub> Separation Performance

To evaluate the CO<sub>2</sub> separation performance of IL-SMHs, first, the CO<sub>2</sub> absorption rate was measured using a TG analyzer. IL-SMH-50 and -33 were found to show about 40 times higher rates than neat [P<sub>66614</sub>][Ala] because of increases in effective surface area. IL-SMHs showed similar rates (0.26 mol-CO<sub>2</sub>·(mol-IL·min)<sup>-1</sup> and 0.24 mol-CO<sub>2</sub>·(mol-IL·min)<sup>-1</sup> for IL-SMH-50 and -33, respectively), suggesting that CO<sub>2</sub> diffusion through a thin [P<sub>66614</sub>][Ala] layer is fast.

To evaluate the reusability of IL-SMH samples, the spent IL-SMH-50 was heated at 393 K for 1 h under a N<sub>2</sub> flow and then used in CO<sub>2</sub> separation. The results show that the samples can be reused at least three times without losing its performance (Fig. 6.6, inset).

Finally, to verify the applicability of IL-SMH-50 for CO<sub>2</sub> separation in flow systems, a breakthrough experiment was conducted (Fig. 6.7). A typical sigmoidal-shaped breakthrough was obtained. This result indicates that IL-SMH can efficiently separate CO<sub>2</sub> in flow systems. In addition, the calculated length of unused bed (LUB), which represents the length of the zone in which sorption takes place, was 19 mm. The column utilization based on the length was 70 % which indicates that 70 % of the adsorbents can be used even though the column was rather short. These results clearly show that IL-SMHs have a high potential to be used for effective CO<sub>2</sub> separation in flow systems.

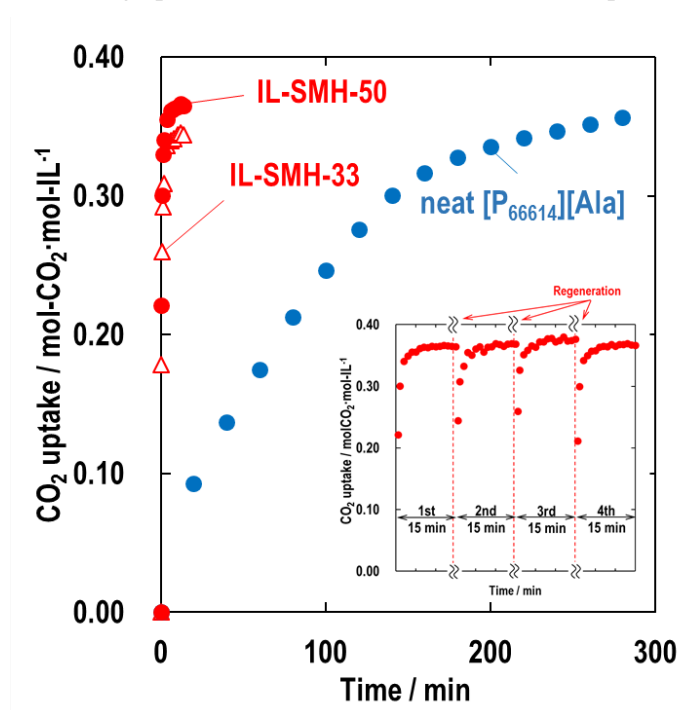


**Fig. 6.6** CO<sub>2</sub> uptake curves of IL-SMH-33 (open red triangle), IL-SMH-50 (solid red circle) and neat [P<sub>66614</sub>][Ala] (solid blue circle). Feed composition: 33 mol% CO<sub>2</sub> in N<sub>2</sub>. Temperature: 303 K. Atmospheric pressure. The inset shows CO<sub>2</sub> uptake curves of regenerated IL-SMH-50 samples. 1<sup>st</sup> cycle (solid red circle) 2<sup>nd</sup> cycle (solid red triangle), 3<sup>rd</sup> cycle (solid red diamond) and 4<sup>th</sup> cycle (red cross); Feed CO<sub>2</sub> pressure, 33 kPa; diluent gas, N<sub>2</sub>; temperature, 303 K; regeneration, heating at 393 K for 1 h under a N<sub>2</sub> flow.

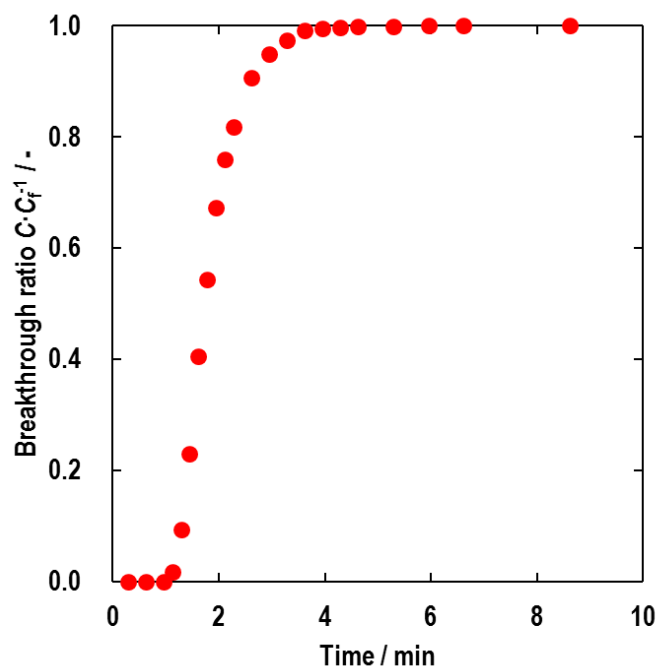


**Fig. 6.7** CO<sub>2</sub> breakthrough curve of IL-SMH-50. Average monolith diameter, 11 mm; total monolith length, 63 mm; mass, 1.2 g; CO<sub>2</sub> flow rate, 3 mL·min<sup>-1</sup>; He flow rate, 6 mL·min<sup>-1</sup>; total gas flow, 9 mL·min<sup>-1</sup>; temperature, 303 K.

## 6.4. Conclusion

SMHs loaded with [P<sub>66614</sub>][Ala] (IL-SMHs) were successfully synthesized by using a simple impregnation method. The pressure drop of the obtained IL-SMH supporting 50 wt % of [P<sub>66614</sub>][Ala] was much lower than that of a column packed with silica gel particles supporting 44 wt % of [P<sub>66614</sub>][Ala]. This result indicated that IL-SMHs can separate CO<sub>2</sub> without causing a severe pressure drop even at high IL loadings when compared with a column packed with silica gel particles loaded with [P<sub>66614</sub>][Ala]. The CO<sub>2</sub> uptake rate of IL-SMHs was around 40-times higher than that of neat [P<sub>66614</sub>][Ala] because of the high effective surface area of the supported [P<sub>66614</sub>][Ala]. CO<sub>2</sub> sorption isotherms of IL-SMHs were of a typical Langmuir-type, indicating that IL-SMHs are preferable to separate CO<sub>2</sub> from post-combustion gases emitted from typical fossil-fuel power plants. IL-SMH can be regenerated at least 3 times by heating without significant decrease in CO<sub>2</sub> uptake performances

were not significantly changed, indicating that IL-SMHs have a high reusability. IL-SMH can separate CO<sub>2</sub> in a flow system and the length of unused bed was only 19 mm, indicating that IL-SMHs have a high potential to be used for effective separation of CO<sub>2</sub> in flow systems. These results indicate that materials with a microhoneycomb structure are preferable to be used as supports of ILs for CO<sub>2</sub> separation when compared with the same material in the particle form.

## 6.5. Reference

1. Keeling, R. F.; Piper, S. C.; Bollenbacher, A. F.; Walker, S. J. Atmospheric CO<sub>2</sub> values (ppmv) derived from in situ air samples collected at Mauna Loa, Hawaii, USA.
2. Karadas, F.; Atilhan, M.; Aparicio, S., Review on the Use of Ionic Liquids (ILs) as Alternative Fluids for CO<sub>2</sub> Capture and Natural Gas Sweetening. *Energ. Fuel.* **2010**, *24* (11), 5817-5828.
3. Choi, S.; Drese, J. H.; Jones, C. W., Adsorbent Materials for Carbon Dioxide Capture from Large Anthropogenic Point Sources. *ChemSusChem* **2009**, *2* (9), 796-854.
4. Song, C., Global Challenges and Strategies for Control, Conversion and Utilization of CO<sub>2</sub> for Sustainable Development Involving Energy, Catalysis, Adsorption and Chemical Processing. *Catal. Today* **2006**, *115* (1-4), 2-32.
5. Yu, C.-H.; Huang, C.-H.; Tan, C.-S., A Review of CO<sub>2</sub> Capture by Absorption and Adsorption. *Aerosol Air Qual. Res.* **2012**, *12* (5), 745-769.
6. Idem, R.; Wilson, M.; Tontiwachwuthikul, P.; Chakma, A.; Veawab, A.; Aroonwilas, A.; Gelowitz, D., Pilot Plant Studies of the CO<sub>2</sub> Capture Performance of Aqueous MEA and Mixed MEA/MDEA Solvents at the University of Regina CO<sub>2</sub> Capture Technology Development Plant and the Boundary Dam CO<sub>2</sub> Capture Demonstration Plant. *Ind. Eng. Chem. Res.* **2006**, *45* (8), 2414-2420.
7. Blanchard, L. A.; Hancu, D.; Beckman, E. J.; Brennecke, J. F., Green Processing Using Ionic Liquids and CO<sub>2</sub>. *Nature* **1999**, *399* (6731), 28-29.
8. Giernoth, R., Task-Specific Ionic Liquids. *Angew. Chem. Int. Ed.* **2010**, *49* (16), 2834-2839.
9. Bates, D. E.; Mayton, D. R.; Ntai, I.; Davis, J. H., CO<sub>2</sub> Capture by a Task-Specific Ionic Liquid. *J. Am. Chem. Soc.* **2002**, *124* (6), 926-927.
10. Goodrich, B. F.; de la Fuente, J. C.; Gurkan, B. E.; Zadigian, D. J.; Price, E. A.; Huang, Y.; Brennecke, J. F., Experimental Measurements of Amine-Functionalized Anion-Tethered Ionic Liquids with Carbon Dioxide. *Ind. Eng. Chem. Res.* **2011**, *50* (1), 111-118.
11. Zhang, J.; Zhang, S.; Dong, K.; Zhang, Y.; Shen, Y.; Lv, X., Supported Absorption of CO<sub>2</sub> by Tetrabutylphosphonium Amino Acid Ionic Liquids. *Chem. Eur. J.* **2006**, *12* (15), 4021-4026.
12. Ruckart, K. N.; O'Brien, R. A.; Woodard, S. M.; West, K. N.; Glover, T. G., Porous Solids Impregnated with Task-Specific Ionic Liquids as Composite Sorbents. *J. Phys. Chem. C* **2015**, *119*

(35), 20681-20697.

13. Kolding, H.; Fehrmann, R.; Riisager, A., CO<sub>2</sub> Capture technologies: Current Status and New Directions Using Supported Ionic Liquid Phase (SILP) Absorbers. *Sci. China Chem.* **2012**, *55* (8), 1648-1656.
14. Zhu, J.; Xin, F.; Huang, J.; Dong, X.; Liu, H., Adsorption and Diffusivity of CO<sub>2</sub> in Phosphonium Ionic Liquid Modified Silica. *Chem. Eng. J.* **2014**, *246*, 79-87.
15. Mukai, S. R.; Nishihara, H.; Tamon, H., Formation of Monolithic Silica Gel Microhoneycombs (SMHs) Using Pseudosteady State Growth of Microstructural Ice Crystals. *Chem. Commun.* **2004**, (7), 874-875.
16. Kaneko, K.; Cracknell, R. F.; Nicholson, D., Nitrogen Adsorption in Slit Pores at Ambient Temperatures: Comparison of Simulation and Experiment. *Langmuir* **1994**, *10* (12), 4606-4609.
17. Cholico-Gonzalez, D.; Avila-Rodriguez, M.; Cote, G.; Chagnes, A., Chemical Properties of Trihexyl(tetradecyl)phosphonium Chloride and Bis(2,4,4-trimethylpentyl)phosphinic Acid Mixtures: Interaction Study by FT-IR and NMR Spectroscopies. *J. Mol. Liq.* **2013**, *187*, 165-170.
18. Al-Oweini, R.; El-Rassy, H., Synthesis and Characterization by FTIR Spectroscopy of Silica Aerogels Prepared Using Several Si(OR)<sub>4</sub> and R<sup>n</sup>Si(OR)<sub>3</sub> Precursors. *J. Mol. Struct.* **2009**, *919* (1-3), 140-145.
19. Sing, K. S. W., Reporting Physisorption Data for Gas/Solid Systems with Special Reference to the Determination of Surface Area and Porosity (Recommendations 1984). *Pure Appl. Chem.* **1985**, *57* (4), 603-619.
20. Esperança, J. M. S. S.; Guedes, H. J. R.; Blesic, M.; Rebelo, L. P. N., Densities and Derived Thermodynamic Properties of Ionic Liquids. 3. Phosphonium-Based Ionic Liquids over an Extended Pressure Range. *J. Chem. Eng. Data* **2006**, *51* (1), 237-242.
21. Lark, B. S.; Patyar, P.; Banipal, T. S.; Kishore, N., Densities, Partial Molar Volumes, and Heat Capacities of Glycine, l-Alanine, and l-Leucine in Aqueous Magnesium Chloride Solutions at Different Temperatures. *J. Chem. Eng. Data* **2004**, *49* (3), 553-565.
22. Murakami, K.; Satoh, Y.; Ogino, I.; Mukai, S. R., Synthesis of a Monolithic Carbon-Based Acid Catalyst with a Honeycomb Structure for Flow Reaction Systems. *Ind. Eng. Chem. Res.* **2013**, *52* (44), 15372-15376.

## ***Chapter 7***

### ***Conclusion***

Sorption processes using fixed bed systems, such as a column packed with spherical particles, have been widely used in industrial fields. However, particle-form sorbents have a disadvantage originating from their morphology. For example, large particles, causing low hydraulic resistance when fluids flow through a column packed with them, have low sorbent usability due to long diffusion path lengths. In contrast, small particles, having short diffusion path lengths, cause a high hydraulic resistance when they are used in a column packed with them. Therefore, a low hydraulic resistance and short diffusion path lengths are not compatible when particles are used as the sorbent. To overcome this trade-off relation, we suggest using a “microhoneycomb (MH) structure” as a sorbent morphology. A MH structure consists of aligned macrochannels measuring a few tenths of a micrometer ( $\mu\text{m}$ ) in diameter and formed by thin channel walls measuring a few  $\mu\text{m}$  in thickness. The straight channels minimize hydraulic resistance, and the thin channel walls minimize diffusion path lengths. Therefore, a low hydraulic resistance and short diffusion path lengths are compatible using a MH structure as the sorbent morphology. In this dissertation, various kinds of sorbents having a MH structure were developed, and their separation performance of diluted species was studied.

Part 1 (chapter 2) reports the phenol and dye adsorption in flow systems using carbon cryogels with a MH structure (CMH). The obtained monolithic CMHs had fairly straight channels of 25–45  $\mu\text{m}$  in diameter and a channel wall thickness ranging from 5 to 10  $\mu\text{m}$ . The pressure drop that occurred when water was passed through this CMH was 90–370 times lower than that of a column packed with particles having similar diffusion path lengths. This result indicates that the CMHs can process fluids without causing a severe hydraulic resistance when compared to columns packed with particles. Nitrogen adsorption/desorption experimental results show that the CMH has a hierarchical micro-meso porous structure, giving rise to BET surface areas of 513–1070  $\text{m}^2\cdot\text{g}^{-1}$ . The phenol and methylene blue adsorption isotherms of the CMH are typical Langmuir-type, which indicates monolayer adsorption. The monolayer uptake increases with an increase in the carbonization

temperature of the CMH, which shows that hydrophobic surfaces are preferable for the adsorption of phenol and methylene blue. The obtained phenol and methylene blue breakthrough curves show typical sigmoidal shapes, and the calculated dynamic capacities are equal to the values calculated from the isotherms. In addition, the length of unused bed (LUB), which represents the length of the zone in which adsorption takes place, is only a few millimeters (mm). These results indicate that the adsorbates can quickly gain access to the adsorption sites in the CMH channel walls even in flow systems. Although the same total pressure drop is shown and the column has the same material properties, the simulated breakthrough curves of a column packed with particles are a few times broader when compared with those of with a CMH measured under the same flow conditions. This result indicates that CMHs can effectively separate contaminants in flow systems when compared with typical columns packed with particles. Also, the results show that CMHs have a high potential to be used for effective separation of water contaminants such as phenol and methylene blue.

Part 2 (chapters 3, 4, and 5) reports on various cesium ion exchangers having a MH structure.

In chapter 3, development of Prussian blue analogues (PBAs), which are typical cesium ion exchangers, supported by silica-alumina microhoneycombs (PBAs-SAMHs) to efficiently remove  $\text{Cs}^+$  is discussed. PBAs-SAMHs were prepared by insolubilization of ferrocyanide by bivalent cations ( $\text{Fe}^{2+}$ ,  $\text{Ni}^{2+}$ ,  $\text{Cu}^{2+}$ , and  $\text{Zn}^{2+}$ ) in a silica-alumina solution following the ice-templating method. The obtained PBAs-SAMHs have a MH structure with about 50-times lower hydraulic resistance when compared with that of a column packed with typical particles having the same diffusion path lengths as the MH structure. Elemental analysis showed that there was a possibility of the formation of PBAs in the sample; however, X-ray diffractometry (XRD) analysis and transition electron microscopy (TEM) could not detect  $\text{Zn}^{2+}$ -insolubilized PBAs.  $\text{Cs}^+$  exchange in batch systems show that the capacity trend was  $\text{Cu}^{2+} > \text{Zn}^{2+} > \text{Ni}^{2+} > \text{Fe}^{2+}$ -insolubilized PBAs-SAMHs. On the other hand, a  $\text{Cs}^+$  breakthrough experiment indicated that the capacity trend was  $\text{Cu}^{2+} > \text{Zn}^{2+} \sim \text{Ni}^{2+} \sim \text{Fe}^{2+}$ . These results demonstrated that  $\text{Cu}^{2+}$ -insolubilized PBAs-SAMHs had the highest potential for use in  $\text{Cs}^+$  separation in flow systems.

Chapter 4 describes the preparation of 12-ammonium molybdophosphate (AMP), a typical heteropoly acid salt, which has a high stability for acidic conditions, supported silica microhoneycombs (SMHs) (AMP-SMHs) to efficiently remove  $\text{Cs}^+$ . Monolithic AMP-SMHs were prepared by adding AMP particles to silica solution followed by the ice-templating method. The adsorbents have a honeycomb-like structure with nearly straight microchannels running through them, and AMP particles are partially embedded intact within the channel walls as characterized by scanning electron microscopy, powder X-ray diffraction, and infrared spectroscopy. AMP-SMH causes a significantly lower pressure drop (about 35 times lower) than a typical column packed with spherical particles with similar diffusion path lengths for  $\text{Cs}^+$  when water was passed through it. Fast and efficient uptake of  $\text{Cs}^+$  from a ppm-level aqueous solution is also allowed, as demonstrated by breakthrough experiments at various inlet flow rates and monolith lengths. The maximum  $\text{Cs}^+$  uptake by AMP-SMH was about two  $\text{Cs}^+$  per AMP, indicating that  $\text{Cs}^+$  can gain access to almost the entire AMP embedded in the SMH. The LUB of the AMP-SMH was a few-times shorter than that reported for a column packed with granular-silica-supported AMP, showing the advantages of AMP-SMH. Comparison of breakthrough curves between the AMP-SMH and columns packed with particles by numerical simulation also indicates that AMP-SMH shows shorter LUB values when compared with the packed column used under the same conditions. These results demonstrate that the obtained adsorbents show a high performance in the continuous separation of  $\text{Cs}^+$  due to their unique MH structure.

In chapter 5, preparation and application of resorcinol formaldehyde monoliths having a microhoneycomb structure (RFMHs) for removing  $\text{Cs}^+$  in water having high pH are described. RFMHs having a lower  $R/C$  value and treated with  $\text{HNO}_3$  showed a high stability and  $\text{Cs}^+$  capacity. The  $\text{Cs}^+$  capacity was maximized when the  $\text{Cs}^+$  solution was at pH 11.9, indicating that RFMHs dissolved at a pH higher than 11.9. The  $\text{Cs}^+$  capacity of RFMHs in flow systems was calculated to be 68% from an ion exchange isotherm. RFMHs can remove  $\text{Cs}^+$  from solutions having a high pH, whereas PBAs and AMP dissolve in such solutions.

Part 3 (chapter 6) reports the preparation of an ionic liquid (IL) having an amino group-supported silica microhoneycomb (IL-SMH) and its application to CO<sub>2</sub> separation in flow systems.

Firstly, to recognize what amount of ILs can be supported by typical particles, a synthesized IL having an amino group ([P<sub>66614</sub>][Ala]) was supported on commercially available silica gel particles; a pressure drop occurred when He gas was flown through a column packed with the particles. The pressure drop dramatically increased when the supported amounts of IL exceeded 44 wt% due to the clogging of the supported IL. In contrast, the results of pressure drop while using SMH as the supporting material of IL suggested that clogging did not occur even when the supported amounts of IL was 50 wt%. To investigate the CO<sub>2</sub> absorption performance, the absorption rate was analyzed using TGA systems. The obtained CO<sub>2</sub> absorption rate of IL-SMH was about 40 times faster than that of neat IL, indicating that the IL was thinly supported on the SMH. To evaluate the reusability of IL-SMH, used samples were regenerated by heating at 393 K for 60 min. IL-SMH can be reused at least three times without any deterioration in their absorption performance. Finally, CO<sub>2</sub> absorption in flow systems were conducted, and the obtained breakthrough curves were of a typical sigmoidal shape, and the LUB value was 19 mm for a monolith of 63 mm. These results concluded that IL-SMH shows a high performance and has a high potential for application in CO<sub>2</sub> separation in flow systems.

In summary, this work showed that monolithic materials with a MH structure have a high potential to be effectively used for various separation, e.g. adsorption, ion-exchange and absorption, in flow systems, compared with typical spherical materials. These results indicate that the ice-templating method can be used with microhoneycomb monoliths for effective separation performance in flow systems. Therefore, it can be concluded that the MH structure is an ideal morphology for separation materials in flow systems. By applying this material to industrial fields, it can be expected that a more efficient separation process can be achieved.

## Acknowledgements

Firstly, I would like to appreciate Professor Shin R. Mukai in the Laboratory of Material Design and Engineering, Division of Applied Chemistry, Faculty of Engineering, Hokkaido University. He gave me many advice, suggestion and discussion even when he was very busy. He patiently listened to my suggestion, opinion and discussion and he also gave me accurate comments for them. Despite I transferred from another laboratory, he gave me many opportunity to attend international conference.

I also deeply appreciate Professor Takao Masuda in the Laboratory of Chemical System and Engineering, Division of Applied Chemistry, Faculty of Engineering, Hokkaido University, as a chief examiner. I deeply appreciate his constructive comments for my dissertation. I also appreciate Professor Atsushi Fukuoka in the Institution for Catalysis, Hokkaido University and Professor Isao Ogino in our laboratory as examiners. Their comments are also very helpful for my dissertation.

I also deeply appreciate Associate Professor Isao Ogino giving me many advice about what research should be done. He gave me positive advice and suggestion every time, and I really respect his positive thinking.

I also deeply appreciate Professor Shinichiroh Iwamura giving me advice for my research. He checked my abstract and manuscript many times and gave me many comments and advices even when he was busy.

I would also like to thank Ms. Akane Kunifuji, Technical Assistant, who was responsible for various general affairs of the laboratory.

I would like to appreciate laboratory members and alumni who contributed to microhoneycombs materials, Messrs. Dr. Takanobu Masuda, Dr. Yoshitaka Satoh, Yoshinao Kimura, Motoki Senoh, Taihei Takanohashi, Yuki Miyoshi, Takeshi Mori, Yuya Yokoyama, Daiki Andoh, Kazuki Sakai, Shunpei Takahashi, Kohei Kitano, Shuichiro Kudo, Kasama Urkasame, Yukei Suzuki, Takuya Aihara, Kazuya Takahashi and Hiroyuki Mega. Because of their cooperation, I really enjoyed working in this laboratory for 5 years. Especially, I would like to appreciate Messrs. Yoshinao Kimura, Kazuya Takahashi and Shuichiro Kudo for special contributions about my works (Y. Kimura for chapter 3, K. Takahashi and S. Kudo for chapter 6). This dissertation did not complete without their cooperation. I also would like to appreciate friendship as coworkers in our laboratory for Messrs. Ryoto Hirahashi, Yuki Miyoshi, Takeshi Mori and Yuya Yokoyama.

A part of this research project was supported by the JSPS KAKENHI, Grant Number 24360324 and 26630396. I appreciate their financial supports. We would like to thank Enago ([www.enago.jp](http://www.enago.jp)) and Editage ([www.editage.jp](http://www.editage.jp)) for the English language review.

Finally, I would like to deeply appreciate my father and mother about their kind help for studying in Hokkaido University. I could not continue my research without their understanding, I want to appreciate again them.



# Research Achievements

## Original Papers

1. Seiichiro Yoshida, Yoshinao Kimura, Isao Ogino, and Shin R. Mukai, "Synthesis of a Microhoneycomb-Type Silica-Supported Ammonium Molybdophosphate for Cesium Separation", *J. Chem. Eng. Jpn.*, 46(9), p. 616-619, 2013.
2. Shin R. Mukai, Yoshinao. Kimura, Seiichiro Yoshida, and Isao Ogino, "Development of a Novel Cesium Adsorbent which Causes Minimal Hydraulic Resistance through the Immobilization of Prussian Blue Analogues in a Monolithic Silica-Alumina Microhoneycomb", *Chem. Eng. Trans.*, 42, p. 181-186, 2014.
3. Seiichiro Yoshida, Shinichiroh Iwamura, Isao Ogino, and Shin R. Mukai, "Adsorption of phenol in flow systems by a monolithic carbon cryogel with a microhoneycomb structure", *Adsorption*, 22(8), p. 1051-1058, 2016.
4. Seiichiro Yoshida, Kazuya Takahashi, Shuichiro Kudo, Shinichiroh Iwamura, Isao Ogino and Shin R. Mukai, "CO<sub>2</sub> Separation in a Flow System by Silica Microhoneycombs Loaded with an Ionic Liquid Prepared by the Ice-Templating Method", *Ind. Eng. Chem. Res.*, Just Accepted.

## International Conference

5. Kazuhiro Murakami, Seiichiro Yoshida, Masatoshi Hashimoto, Isao Ogino and Shin R Mukai, Utilization of heteropoly acid supported by silica microhoneycomb in flowing system, 2012 CSE Summer School, 2012.7.15-16, Jozankei, Poster
6. Kazuhiro Murakami, Seiichiro Yoshida, Masatoshi Hashimoto, Isao Ogino and Shin R Mukai, Synthesis of Silica Microhoneycomb-Immobilized Heteropoly Acid Catalyst for Liquid-Phase Esterification Reaction, 10th Japan-Korea Symposium on Materials & Interface International Symposium on Frontiers in Chemical Engineering, 2012.11.7-10, Kyoto, Poster
7. Kazuhiro Murakami, Seiichiro Yoshida, Masatoshi Hashimoto, Isao Ogino and Shin R Mukai, Utilization of Heteropoly Acid Supported by Silica Microhoneycomb in a Flow System, The 6th

- International Conference on Multi-functional Materials and Application, 2012.11.22-24, Daejeon, Korea, Poster
8. Shin R. Mukai, Yoshinao Kimura, Seiichiro Yoshida, Isao Ogino, Development of a Novel Cesium Adsorbent Which Causes Minimal Hydraulic Resistance through the Immobilization of Prussian Blue Analogues in a Monolithic Silica-alumina Microhoneycomb, The 8th Conference on Sustainable Development of Energy, Water and Environment Systems, 2013.9.22-27, Dubrovnik, Croatia, Oral
  9. Seiichiro Yoshida, Yoshinao Kimura, Isao Ogino and Shin R. Mukai, Cesium Separation using Silica Microhoneycomb Supported Ammonium Molybdophosphate, The 1st International Symposium on Ambitious Leaders Program for Fostering Future Leaders to Open New Frontiers in Materials Science, 2014.3.7, Sapporo, Poster
  10. Seiichiro Yoshida, Yoshinao Kimura, Isao Ogino and Shin R. Mukai, Silica Microhoneycomb Supporting Heteropoly Salts for Continuous Cesium Separation, 3rd FCC International Symposium, 2014.6.13-14, Sapporo, Poster
  11. Seiichiro Yoshida, Yoshinao Kimura, Isao Ogino and Shin R. Mukai, Heteropoly acid salts immobilized into silica microhoneycomb for cesium separation in continuous systems, 2014 CSE Summer School, 2014.7.19-20, Jozean, Oral
  12. Seiichiro Yoshida, Yoshinao Kimura, Isao Ogino and Shin R. Mukai, Cesium Uptake in a Flow System Using Ammonium Molybdophosphate Immobilized in a Silica Microhoneycomb, 7th NITTH Joint Symposium, 2014.7.21-24, Sapporo, Poster
  13. Seiichiro Yoshida, Yoshinao Kimura, Isao Ogino and Shin R. Mukai, Continuous Cesium Separation Using a Silica Microhoneycomb Supporting Ammonium Molybdophosphate, 2014 AIChE Annual Meeting, 2014.11.16-21, Atlanta, USA, Poster
  14. Seiichiro Yoshida, Shinichiro Iwamura, Isao Ogino and Shin R. Mukai, Synthesis of monolithic carbon cryogels with microhoneycomb structure for continuous separation of phenol, 2015 CSE Summer School, 2015.8.22-23., Otaru, Poster

15. Seiichiro Yoshida, Shinichiroh Iwamura, Isao Ogino and Shin R. Mukai, Adsorption of phenol in a continuous flow system using carbon microhoneycombs, 7th Pacific Basin Conference on Adsorption Science and Technology, 2015.9.24-27., Xiamen, China, Poster
16. Seiichiro Yoshida, Shinichiroh Iwamura, Isao Ogino and Shin R. Mukai, Application of carbon cryogels with a microhoneycomb structure for continuous separation of phenol and methylene blue, 2016 CSE Summer School, 2016.7.16-17., Jozeikai, Poster
17. Seiichiro Yoshida, Shinichiroh Iwamura, Isao Ogino and Shin R. Mukai, Adsorption of Water Contaminants in Continuous Flow Systems Using Carbon Cryogels with a Microhoneycomb Structure, 2016 AIChE Annual Meeting, 2016.11.13-20, San Francisco, USA, Poster

## **Awards**

18. Academic award, The Society of Chemical Engineering, Japan, Hokkaido branch, 2013.1.31
19. Otsuka Hiroshi sensei memorial award, Graduate School of Chemical Science and Engineering, Hokkaido University, 2014.3.31
20. Academic award, The Society of Chemical Engineering, Japan, Hokkaido branch, 2015.1.30
21. Incentive award, The Society of Separation Process Engineers, Japan, 2015. 5.30
22. The Best Student Award, The Society of Chemical Engineering, Japan, 2016.3.15
23. A research encouragement award, The Japan Society on Adsorption, 2016.5.26